AUTHOR ACCEPTED MANUSCRIPT

Oolitic ironstones, continental iron flux and reverse weathering in the Proterozoic Eon: insights from the Tonian Katherine Group, Yukon

Lechte, M.[1]*, Halverson, G.[1], Wallace, M.[2], Gibson, T.[3], Hood, A.v.S.[2], Wang, C.L.[4,5], Bui, T.H.[1], Maloney, K.[1], Millikin, A.[3]

[1]*Department of Earth and Planetary Sciences/GEOTOP, McGill University, Montréal, Canada*
[2]*School of Earth Sciences, University of Melbourne, Melbourne, Australia*
[3]*Department of Geology and Geophysics, Yale University, New Haven, USA*
[4]*Key Laboratory of Mineral Resources, Institute of Geology and Geophysics, Chinese Academy of Sciences, Beijing, China*
[5]*College of Earth and Planetary Sciences, University of Chinese Academy of Sciences, Beijing, China*

*maxwell.lechte@mail.mcgill.ca

Highlights

- Ironstones have a distinct texture and mineralogy to iron formations
- The Tonian Katherine Group ironstone was deposited in low-energy coastal settings
- Diagenesis of weathering products led to redox cycling and phyllosilicate authigenesis
- Common in the Phanerozoic record, ironstones also span the Proterozoic Eon
- Ironstones can provide valuable constraints on biogeochemical cycles in deep time

Abstract

Oolitic ironstones are iron-rich and chert-poor sedimentary rocks containing concentrically coated grains composed of iron (oxyhydr)oxides and iron phyllosilicates that offer a unique window into iron cycling in ancient coastal environments. These enigmatic deposits are common in the Phanerozoic stratigraphic record yet lack clear modern analogues, and curiously are thought to be absent from Precambrian strata, suggesting a secular control on their deposition. Here we describe a previously unreported ironstone from the middle Tonian (ca. 850 Ma) Katherine Group in the Wernecke Inlier (Yukon, Canada), and show that similar deposits can be found—albeit rarely—throughout the Proterozoic. We investigate the origin of this unit and evaluate its palaeoenvironmental significance, and in light of an extensive literature review, present a holistic model for Precambrian ironstone deposition. The Katherine ironstone occurs in multiple horizons in the McClure and Abraham Plains formations and contains iron ooids and oncoids composed dominantly of authigenic hematite and berthierine, with detrital quartz grains. Textural relationships demonstrate that these coated grains formed on the seafloor with synsedimentary reworking, and the fine interlamination of these phases in grain coatings suggests redox and pH fluctuation during ironstone genesis. Facies associations indicate that the ironstones accumulated in a range of low-energy, shallow marine environments (tidal mudflats and coastal embayments). Geochemical analyses offer insights into genetic processes, and the radiogenic Nd isotope composition and negative Eu anomalies of the Katherine ironstone suggest a continental iron source. We present a model whereby abundant iron, cations, and silica—requisite for the authigenesis of iron phyllosilicates—were supplied from chemical weathering and preferentially enriched in coastal environments due to gradients in pH, Eh and salinity. This continental input would have led to intense iron cycling coupled to organic matter respiration, iron phyllosilicate authigenesis (i.e., reverse weathering). The enrichment of authigenic Fe(III) (oxyhydr)oxides and Fe(II) phyllosilicates took place on a broad coastal plain influenced by both autogenic and allogenic fluctuations in relative sea level, likely in a humid, tropical climate. The lenticular and episodic nature of ironstones in the Proterozoic stratigraphic record suggests that a unique combination of environmental conditions fostered ironstone accumulation. By reviewing the literature on oolitic ironstones, we re-evaluate the temporal distribution of these deposits compared to Archaean–Palaeoproterozoic iron formations, and show that the Great Oxidation Event may have been a prerequisite for ironstone deposition, which may implicate oxidative chemical weathering or suboxic, marine iron cycling. In general, we suggest that the Precambrian record of oolitic ironstones represents an important deep-time archive of iron and nutrient cycling in coastal settings.

Keywords

- Ironstone
- Neoproterozoic
- Sedimentology
- Paleoredox
- Iron cycle

1. Introduction

Sedimentary iron deposits are among the oldest rocks on Earth, and have long been used as a window into the nature of ancient surface environments (e.g., Leith, 1908; Gruner, 1922; Cloud, 1973; Moorbath et al., 1973). Iron is highly immobile under oxidising, circumneutral conditions, and therefore the transport and enrichment of sedimentary iron can be indicative of redox processes and pH variations (often mediated by biological activity), and in some cases hydrothermal activity (e.g., Krumbein and Garrels, 1952; James, 1954; Raiswell and Canfield, 2012; Tosca et al., 2019; Kappler et al., 2021). In addition, the precipitation of iron minerals often involves the scavenging of ambient organic matter, nutrients, trace elements and other dissolved species (e.g., Huerta-Diaz and Morse, 1992; Boyd and Ellwood, 2010; Lalonde et al., 2012; Zegeye et al., 2012; Tostevin and Ahmed, 2023). Therefore, studying the sedimentology, mineralogy and geochemistry of sedimentary iron deposits can be used to gain important insights into ancient biogeochemical cycles, water chemistry, and hydrothermal processes on local to global scales (e.g., Van Houten and Bhattacharyya, 1982; Beukes and Klein, 1992; Isley and Abbott, 1999; Li et al., 2015; Konhauser et al., 2017; Koschinsky and Hein, 2017; Lechte et al., 2019b; Smith et al., 2020; Matheson et al., 2022). This sedimentary iron record provides a unique complement to the study of carbonates, shales, and other sedimentary rocks. Here, we review the nature and significance of oolitic ironstones from the Precambrian to the holistic understanding of Earth's surface evolution, and compare these to other Precambrian iron deposits such as banded iron formations. We present new observations from an ironstone-bearing succession from the early Neoproterozoic Katherine Group (Yukon, Canada), and use these to inform a genetic model for ironstone deposition during this time. Within this framework, we discuss how Precambrian ironstones can be further used as constraints on Earth's surface processes in deep time.

The terminology for iron-rich sedimentary rocks has historically been variable, and confusion persists regarding how to interpret the palaeoenvironmental significance of these deposits. Before discussing the genetic implications of ironstones, we outline the definitions and key differences between oolitic ironstones and iron formations, and these distinctions are summarised in Table 1.

1.1 Ironstone terminology

Ironstones are a unique type of iron-rich sedimentary rock that are common in the Phanerozoic geological record, and have been used to make inferences about climate and global biogeochemical cycles during this time (e.g., Young, 1989; Petránek and Van Houten, 1997; Taylor and Macquaker, 2011; Abram and Holz, 2020; Matheson and Pufahl, 2021). Ironstones are characterised by the presence of concentrically laminated coated grains composed of iron oxides (goethite, hematite) and/or iron silicates (berthierine, chamosite). By analogy to carbonate textures, these are often referred to as iron ooids, and ironstones with an abundance of iron ooids are termed oolitic (or ooidal). As such, ironstones have been defined as "*non-cherty, sandy clayey siliciclastic or siliciclastic–carbonate sedimentary rock with more than 50% of ferruginous ooids and more than 15% of iron*" (Petránek and Van Houten, 1997), or "*sandy, clayey, and oolitic, shallow inland-sea*" iron deposits (Kimberley, 1978), and are interpreted to have been deposited in a range of coastal environments (e.g., Van Houten and Arthur, 1989; Petránek and Van Houten, 1997). The terms "Clinton-type", "Minette-type", and "Lorraine-type" are variably used to describe oolitic ironstones from different regions, however, there is significant overlap in the nature of the deposits that have been described using these terms (Kimberley, 1989) and further work is needed to elucidate the distinction between the different subtypes of ironstone. These deposits represent a significant historical and current resource of iron, phosphorus, and rare earth elements (e.g., Hatch, 1920; Baioumy et al., 2017; Rudmin et al., 2020). Near-exclusively described in Phanerozoic successions, the term 'ironstone' is often used to contrast with Precambrian 'iron formations' (e.g., James, 1966), which are considered to be indicative of vastly different environmental conditions during the Precambrian (e.g., Cloud, 1973; Holland, 1973; Fryer, 1977; Rasmussen et al., 2012; Konhauser et al., 2017).

1.2 Iron formation terminology

Iron formations have been defined as "*a chemical sediment, typically thin-bedded or laminated, containing 15% or more Fe of sedimentary origin, commonly but not necessarily containing layers of*

chert" (James, 1954). Iron formations are often termed either 'banded' (featuring thinly laminated to bedded layers of fine-grained iron (Fe) minerals; i.e., an iron lutite) or 'granular' (featuring sand-sized grains of Fe minerals; i.e., an iron arenite) (Beukes, 1980; Trendall, 2002). In addition to texture, these iron formations can be categorised based upon their depositional environment and tectonic setting, and iron formations are often distinguished as those that are intimately associated with volcanic rocks in tectonically active settings, or those interbedded with carbonates and clastic rocks in more stable continental basins.

Many iron formations are associated with submarine volcanic rocks and greywackes in volcanic arc, back-arc, spreading ridge or intracratonic rift settings; these are often found in greenstone belts and are typically lenticular deposits on the kilometre scale (Goodwin, 1973; Gross, 1980; Huston and Logan, 2004; Bekker et al., 2010). These iron formations can be associated with volcanogenic massive sulphide deposits which form due to hydrothermalism associated with volcanic activity (Peter, 2003; Tornos et al., 2015), and this type of iron formation is sometimes termed "exhalative" or referred to as an "exhalite" (Hutchinson et al., 1971). Others prefer to avoid using a genetic term (such as exhalative) to describe iron formation deposit types, with Kimberley (1978) referring to these as "*shallow-volcanic-platform*" or "*deep-water*" iron formations. These volcanic-associated iron formations are exclusively banded and/or laminated without evidence for wave influence, suggesting deposition in relatively deep water (Gross, 1980; Konhauser et al., 2017). By analogy to the iron formations of the Algoma Basin in Ontario (Canada; Goodwin, 1962), these were referred to as "Algoma-type" iron formations within Canada (Gross, 1965b), and this term continues to be used to describe deposits globally (e.g., Konhauser et al., 2017; Pirajno and Yu, 2021).

In terms of mass of sedimentary iron, the majority of iron formation is associated with carbonates and shales in continental shelf settings (Gross, 1980; Isley, 1995), termed "*metazoan-poor, extensive, chemical sediment- rich, shallow-sea iron formation*" by Kimberley (1978). Compared to exhalative iron formations, these continental shelf iron formations are much more laterally extensive (Isley, 1995; Bekker et al., 2010), can be exceptionally thick, and may or may not be granular in texture (James, 1954; Simonson and Goode, 1989; Beukes and Klein, 1990). Though these are often also interbedded with volcanic rocks (Trendall, 1968), the continental shelf iron formations are considered to lack the intimate association and genetic link with volcanism implied for exhalative iron formations (Gross, 1983). Some granular iron formations can have coated grains (i.e., iron ooids) and evidence for deposition above storm wave base (Dimroth and Wolf, 1976; Gross and Zajac, 1983; Ojakangas, 1983; Bekker et al., 2014), and therefore share some key similarities with Phanerozoic ironstones. However, the mineralogy and geochemistry of Precambrian granular iron formations is distinct from Phanerozoic oolitic ironstones (Kimberley, 1978; James, 1992; Simonson, 2003; Klein, 2005). In contrast to ironstones, iron formations are chert rich with a more complex Fe mineral assemblage that may comprise magnetite, hematite, siderite, ankerite, greenalite, stilpnomelane and minnesotaite, and typically contain much less phosphate than Phanerozoic ironstones (e.g., Geijer, 1962; Klein, 2005). These deposits are also texturally different, as granular iron formations have sand-sized grains of jasper and iron minerals (Simonson and Lanier, 1987) that are not usually found in ironstones. Where present, concentrically coated grains within iron formations often have fewer, coarser rims and a more radial texture (Dimroth and Chauvel, 1973; French, 1973; Akin et al., 2013; Smith et al., 2017; Dodd et al., 2018), in contrast to Phanerozoic iron ooids which typically have tens to hundreds of well-developed, tangential cortical laminae (Adeleye, 1973; Bhattacharyya, 1983; Van Houten and Purucker, 1984). Geochemically, Phanerozoic ironstones are less Si-rich (due to a lack of chert) and more Al-rich (due to a greater abundance of phyllosilicates) compared to Precambrian granular iron formations. These mineralogical, geochemical, and textural differences may imply different origins, although post-depositional processes can complicate the interpretation of primary mineralogy (e.g., Duncanson et al., 2024) and further work is needed.

Much of the early, detailed work on iron formations was focused on the iron formations in the Palaeoproterozoic sedimentary basins that surround the Lake Superior region of Canada and the United States of America, which characteristically feature oolitic units (Van Hise, 1901; Leith, 1908; Gruner, 1922; James, 1954). The term "Superior-type" iron formation has subsequently become widely used to describe all iron formations associated with carbonates and siliciclastic rocks (i.e., continental shelf iron formations), including the exceptionally thick and extensive iron formations of the Hamersley Basin (Australia) and Transvaal Basin (South Africa) (Gross, 1980). This is potentially confusing, given that the Hamersley and Transvaal banded iron formations, for instance, differ greatly in their textural and sedimentological features and areal extent compared to those of the Lake Superior region (Trendall, 1968). It is important to note that while, for example, the Hamersley and Transvaal basin iron formations have some intervals with granular iron formations (i.e., iron arenites) interbedded with banded iron formations (Simonson and Goode, 1989; Beukes and Klein, 1990), coated grains / iron

ooids have never been reported from these intervals. Therefore, we suggest that current use of the term “Superior-type” iron formation encompasses at least two major, distinct types of iron formation: iron ooid-bearing, granular iron formations (such as those of the Lake Superior region), and thick, laterally extensive banded iron formations (such as those of the Hamersley and Transvaal basins).

A third category of iron formation refers to those that are intimately associated with glacial deposits, sometimes named “Rapitan-type” iron formations (James, 1992) after the Neoproterozoic Rapitan Group in Northwest Territories (Canada). In the Rapitan Group, sedimentary iron deposits include cherty, banded iron formations and hematitic mudstones and siltstones, and these are interbedded with glacial diamictites and feature dropstones suggesting deposition during glaciation (Gross, 1965a; Yeo, 1981; Klein and Beukes, 1993). Similar iron formations can be found in Neoproterozoic glacial successions globally, and are interpreted to have been deposited in a range of glaciomarine environments (e.g., Young, 1976; Cox et al., 2013; Lechte et al., 2018; Lechte et al., 2019a).

1.3 Temporal distribution of ironstones and iron formations

Though ironstones are typically associated with the Phanerozoic and iron formations with the Precambrian (Kimberley, 1989), their temporal distribution is more widespread. Volcano-sedimentary iron formations date back to the Eoarchaean (Moorbath et al., 1973; O'Neil et al., 2018), and this type of iron formation is relatively rare after the Neoarchaean. However, isolated examples are reported from the Palaeoproterozoic (Slack et al., 2007; Slack et al., 2009; Lan et al., 2017; Zeng et al., 2023), Mesoproterozoic (Hu et al., 2023), Neoproterozoic (e.g., Volkert et al., 2010; Basta et al., 2011; Yellappa et al., 2016; El-Shazly et al., 2019; Yang et al., 2023a), and Phanerozoic (Grenne and Slack, 2003; Van Staal et al., 2003; Hollis et al., 2015; Li et al., 2018; Yang et al., 2021; Hu et al., 2022; Yang et al., 2023b), although the precise ages of many of these units are uncertain. The more extensive (continental shelf) iron formations first appear in the Palaeoarchaean–Mesoarchaean (Heubeck, 2019; Smith and Beukes, 2023) and were widely developed in the Neoarchaean and early Palaeoproterozoic, but are rare to absent after this time. Granular iron formations were deposited globally around 1880 Ma (Rasmussen et al., 2012), with only rare examples reported outside of this event from the early Palaeoproterozoic (Beukes, 1983; Beukes and Klein, 1990) and Mesoarchaean (Smith et al., 2017). Iron formations associated with glacial deposits are considered to be exclusively Neoproterozoic in age, and generally linked to the ca. 720–660 Ma ‘Sturtian’ ice age (Young, 2002; Macdonald et al., 2010; Cox et al., 2013; Lechte et al., 2019b), though iron formations have been observed to overlie diamictites from the Mesoarchaean (Smith et al., 2013) and Palaeoproterozoic (Le Heron et al., 2022).

Importantly, deposits that are compositionally and texturally similar to Phanerozoic ironstones (with a similar depositional environment) do occur in the Precambrian stratigraphic record (Fig. 1; e.g., Tegengren, 1921; Schweigart, 1965; Jackson et al., 1986; Dorland, 1999). This shows that ironstones are not exclusively Phanerozoic in age, just as iron formations are not exclusively Precambrian in age. The observation of Precambrian ironstones is important, as the Precambrian Earth was characterized by dramatically different surface conditions compared to the Phanerozoic Eon, including lower atmospheric and marine O_2 levels (e.g., Lyons et al., 2021), a lack of terrestrial vegetation (e.g., Wellman and Strother, 2015), and a distinct climate regime (Young, 2013; Mills et al., 2017). These Precambrian oolitic deposits, which have variably been referred to as “iron formations” or “ironstones”, can offer important insights into Earth’s surface evolution during this time (e.g., Eriksson and Cheney, 1992; Dorland, 1999; Konhauser et al., 2011; Köykkä and Lamminen, 2011; Partin et al., 2013; Swanner et al., 2014; Lin et al., 2019; Johnson et al., 2020a; Qiu et al., 2022; Tang et al., 2022; Wang et al., 2022). However, compared to the decades of extensive research into Phanerozoic ironstones (reviewed in Young, 1989; Petránek and Van Houten, 1997; Matheson and Pufahl, 2021), Precambrian ironstones remain understudied and enigmatic. Key aspects of their genesis are unclear, including their iron source, depositional environment, mechanism of iron mineral precipitation, and diagenetic history, which obfuscates the implications of these deposits for Earth’s surface evolution. Here, we present a detailed case study on an oolitic ironstone from the middle Tonian Katherine Group (Yukon, Canada), deposited in a succession bounded by units that feature important fossil evidence for increasing eukaryotic complexity (Fig. 2). Because the oolitic ironstones were previously thought to be absent from the Neoproterozoic (Petránek and Van Houten, 1997), this represents an important deposit for understanding the temporal distribution of ironstones. Building upon insights from this deposit, we present a genetic model for ironstones and consider the broader implications of the ironstone sedimentary record throughout Earth’s history.

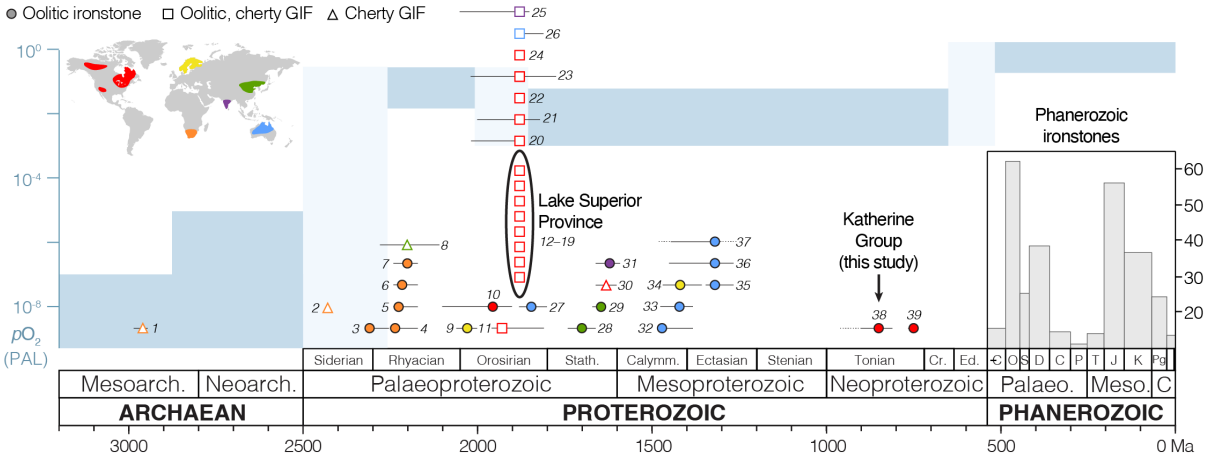

Fig. 1. Temporal and geographical distribution of Precambrian oolitic ironstones (filled circles) and cherty, coated grain-bearing granular iron formations (open squares), and granular iron formations (GIF) that lack iron-coated grains (triangles). The range of permissible age ranges is based upon the currently available geochronological constraints is indicated by the black horizontal lines, with the exception of the Lake Superior Province iron formations, which are assumed to be broadly contemporaneous with the Gunflint iron formation (dated to 1878.3 ± 1.3 Ma) (Fralick et al., 2002). The colour of the symbols indicates the present-day location of their host sedimentary basins (see inset). Numbers correspond to specific deposits. 1: Nconga Formation GIF (Mozaan Group, Witwatersrand-Mozaan basin, South Africa). 2: Griquatown iron formation GIF (Ghaap Group, Griqualand West basin, South Africa). 3–7: Pretoria Group ironstones (3: Timeball Hill; 4: Dwaal Heuvel; 5: Strubenkop; 6: Daspoort; 7: Silverton formations) of Transvaal basin (South Africa). 8: Yuanjiacun Formation GIF (Lüliang Group, Shanxi Province, North China craton). 9: Kolasjoki Sedimentary Formation ironstone (Kola Peninsula, Russia). 10: Pokegama Formation ironstone (Animikie Group, Mesabi Iron Range, Minnesota). 11: Watterson Formation GIF (Hurwitz Group; Hurwitz Basin, Nunavut, Canada). 12–19: extensive, correlative oolitic granular iron formations of the Lake Superior Province (Ontario, Canada and Minnesota, Michigan and Wisconsin, USA), including the Animikie Group (Gunflint and Biwabik); North Range Group (Trommald); Baraga Group (Ironwood); Michigamme Formation (Bijiki), Menominee Group (Negaunee); Fence River Formation; and Vulcan iron formation. 20: Kipalu Formation (Belcher Group; Belcher Islands, Nunavut, Canada). 21. Temiscamie Formation GIF (Mistassini Group; Lake Albanel Iron Range, Québec, Canada). 22: Sokoman Formation GIF (Ferriman Group; Labrador Trough, Québec, Canada). 23: Nastapoka Group GIF (Richmond Gulf graben; Nunavut, Canada). 24: Gibralter Formation GIF (Pethei Group; East Arm fold belt, Northwest Territories, Canada). 25: Chilpi Group GIF (Dongargarh Supergroup, Bastar Craton, India). 26: Frere Formation GIF (Tooloo Group; Earaheedy basin, Western Australia). 27: Chiall Formation ironstone (Miningarra Group; Earaheedy Basin, Western Australia). 28: Yunmengshan Formation ironstone (Ruyang Group; Henan Province, North China craton). 29: Chuanlinggou Formation ironstone (Changcheng Group; Yanshan basin, Hebei Province, North China craton). 30: Freedom Formation GIF (Lake Superior Province, Wisconsin, USA). 31: Nagari Quartzite ironstone (Nallamai Group, Dharwar Craton, India). 32–33: Roper Group ironstones, McArthur Basin, northern Australia (Wadjeli Sandstone Member, Mainoru Formation; Munyi Member, Corcoran Formation). 34: Brattefjell Formation (Rjukan Group, southern Norway). 35: Sherwin Formation (Roper Group, McArthur Basin, northern Australia). 36: Wondoan Hill Formation (Tijunna Group; Birrindudu Basin, northern Australia). 37: Train Range Member, Mullera Formation ironstone (South Nicholson Group; Queensland, Australia). 38: McClure and Abraham Plains formations, Katherine Group ironstone (Wernecke Inlier, Yukon, Canada). 39: Galeros and Carbon Butte formations, Chuar Group ironstone (Arizona, USA). Occurrences of Phanerozoic ironstones are shown as a histogram (grouped by geological period; data from Petránek and Van Houten, 1997). Indicated in blue is a schematic representation of the range in estimates for atmospheric pO_2 levels that are consistent with geological proxy constraints during this time, with the light blue boxes representing periods that experienced major stepwise changes in atmospheric pO_2 (adapted from Reinhard and Planavsky, 2022). For further discussion of the temporal distribution of ironstones see Section 7.5.

Table. 1. Comparison of the characteristic features of ironstones and iron formations. Data are summarised from the published literature (Beukes and Klein, 1990; Morey, 1992; Dorland, 1999; Klein, 2005; Schröder et al., 2011; Cox et al., 2013; Smith et al., 2013; Haugaard et al., 2016; Ossa et al., 2016; Baioumy et al., 2017; Konhauser et al., 2017; Smith et al., 2017; Warchola et al., 2018; Lechte et al., 2019b; Lin et al., 2019; Rudmin et al., 2019; Zhu et al., 2019; Sokol et al., 2020; Dunn et al., 2021; Lan et al., 2021; Martins et al., 2022; Qiu et al., 2022; Sindol et al., 2022; Tang et al., 2022; Afroz et al., 2023; Duncanson et al., 2023; Smith and Beukes, 2023).

Deposit type	Iron ooids	Textures / structures	Major minerals	Detrital minerals	Temporal distribution	Depositional environments	Host rocks	Fe	Si	Al	Mn
(Oolitic) ironstone	Always	Hardgrounds, intraclast breccias, cross bedding, desiccation cracks, possible microbial textures	Berthierine, chamosite, goethite, hematite, francolite	Abundant quartz grains, reworked fossils	Palaeo-proterozoic–modern	Coastal, estuarine, shallow marine, lacustrine, shoals, offshore	Mudstone, carbonates, sandstone	20–50 %, typically ~35 %	1–30 %, typically ~5 % (variable due to detrital quartz)	2–12 %, typically ~3 %	0.05–15 %, typically ~0.1 %
Granular iron formation	Sometimes	Granules, intraclasts, trough cross bedding, ripple marks, planar lamination, chert banding, iron stromatolites	Chert, magnetite, hematite, greenalite, stilpnomelane, chamosite, chlorite, siderite, ankerite, dolomite	Rare quartz, zircon, intraclasts of reworked chert	Palaeo-proterozoic with a possible Mesoarchaean example	Shallow marine, shoals, continental shelf, intracratonic basin	Volcanics, shale, carbonates	20–60 %, typically ~30 %	5–40 %, typically ~20 %	0.02–10 %, typically <1 %	0.01–5 %, typically ~0.05 %
Banded iron formation	Never	Chert banding, fine lamination, no evidence of wave agitation	Chert, magnetite, hematite, greenalite, stilpnomelane, minnesotaite, chlorite, siderite, ankerite, riebeckite	Rare / absent	Archaean–Palaeo-proterozoic, with minor younger examples	Offshore marine (below wave base), continental shelf, rift basins, volcanic arcs, back-arc basins	Volcanics, greywackes, shale, carbonates	20–60 %, typically ~30 %	5–40 %, typically ~20 %	0.05–6 %, typically <1 %	0.1–15 %, typically ~0.1 %
Glacial iron formations	Never	Planar lamination, grading, rare ripple marks, dropstones	Hematite, minor chert, magnetite, siderite	Quartz, zircon, feldspar, clays, dolomite	Neoproterozoic (Sturtian)	Glaciomarine, rift basins	Diamictite, shale, sandstone, carbonates	15–60 %, typically ~30 %	2–40 %, typically ~20 %	0.05–8 %, typically ~4 %	0.01–30 %, typically ~0.05

2. Geological setting of the Katherine Group ironstone

The ironstone-bearing Katherine Group is part of the Tonian Mackenzie Mountains Supergroup, which represents a thick and relatively continuous sedimentary succession interpreted to have been deposited in an intracratonic sag basin (Rainbird et al., 1996) or extensional basin (Turner and Long, 2008) during crustal attenuation and thermal subsidence in northwestern Laurentia. These units are well exposed in the Wernecke Mountains (Yukon Territory) and the Mackenzie Mountains (Northwest Territories) of northwestern Canada (Young et al., 1979; Long and Turner, 2012) and unconformably overlie the late Mesoproterozoic carbonate-dominated Pinguicula Group (Eisbacher, 1978; Medig et al., 2016). The Mackenzie Mountains Supergroup is unconformably overlain by the Cryogenian–Ediacaran strata of the Windermere Supergroup (Eisbacher, 1985).

In the Wernecke Inlier, the basal Mackenzie Mountains Supergroup is made up of the mixed carbonate–siliciclastic succession of the Hematite Creek Group (Turner, 2011b). The Hematite Creek Group comprises three conformable units, which record a shoaling-upward sequence and a transition from outer-shelf to slope marine settings (Dolores Creek Formation) through to peritidal environments (Black Canyon Creek Formation and overlying Tarn Lake Formation; Turner, 2011b; Maloney et al., 2021). The uppermost Hematite Creek Group has abundant sandstones and siltstones deposited in storm-influenced coastal settings with intermittent subaerial exposure, and similar facies in the overlying Katherine Group suggest that this contact is conformable and transitional (Hume and Link, 1945; Turner, 2011b; Long and Turner, 2012). The Katherine Group is in turn conformably overlain by basinal shales and carbonates of the Little Dal Group (Gabrielse et al., 1973; Aitken, 1981; Turner, 2011b). In the Mackenzie Mountains the lower Little Dal Group stromatolitic reefs are potentially indicative of increasing ecosystem complexity (Turner et al., 1993; Neuweiler et al., 2009), as may be supported by macrofossil assemblages (Hofmann and Altken, 1979; Hofmann, 1985) and putative fossil evidence for metazoans (Turner, 2021). In the study area in the Wernecke Inlier, the Mackenzie Mountains Supergroup is incised by a major erosional unconformity, and only the lowermost Little Dal Group (calcareous shales of the Stone Knife Formation) is preserved. The late Tonian Coates Lake Group is absent, and conglomerates interpreted to be a part of the Cryogenian Rapitan Group rest on the unconformity (Fig. 2; Macdonald et al., 2018).

Direct geochronological age constraints on the Mackenzie Mountains Supergroup are scarce. The Wernecke Supergroup, which underlies the Pinguicula Group, is intruded by gabbro of the Hart River sills (Abbott, 1997) which have been dated to ca. 1382 Ma (Verbaas et al., 2018). A detrital zircon U–Pb age of 1003 ± 4 Ma was obtained from strata that are likely equivalent to the Hematite Creek Group in the Hart River Inlier (Ogilvie Mountains, Yukon; Rainbird et al., 1997), and detrital zircon U–Pb geochronology of the Katherine Group preserves a late Mesoproterozoic peak, with a youngest age of 1083 ± 2 Ma (Rainbird et al., 1997). Muscovite Ar–Ar ages from the Hematite Creek Group are typically 1100–1000 Ma, with the youngest age obtained 1033 ± 9 Ma (Thorkelson, 2000). The only direct stratigraphic age on the lower Mackenzie Mountains Supergroup is a shale Re–Os age of 898 ± 68 Ma on the upper Dolores Creek Formation (Fig. 2; Maloney et al., 2021). A zircon U–Pb age of 775.10 ± 0.54 Ma from the Little Dal Basalt (which overlies the Little Dal Group in the Mackenzie Mountains) provides a minimum age constraint on the Little Dal Group (Milton et al., 2017). In the Mackenzie Mountains, the upper Little Dal Group features a prominent, prolonged negative shift in carbonate carbon isotope ($\delta^{13}C_{carb}$) values, interpreted to record the global, ca. 810–800 Ma "Bitter Springs" carbon isotope anomaly (Halverson, 2006; Macdonald et al., 2010; Swanson-Hysell et al., 2015; Zhang et al., 2023). Based on these constraints, and the conformable contacts above and below, we infer that the Katherine Group was probably deposited between ca. 900–850 Ma.

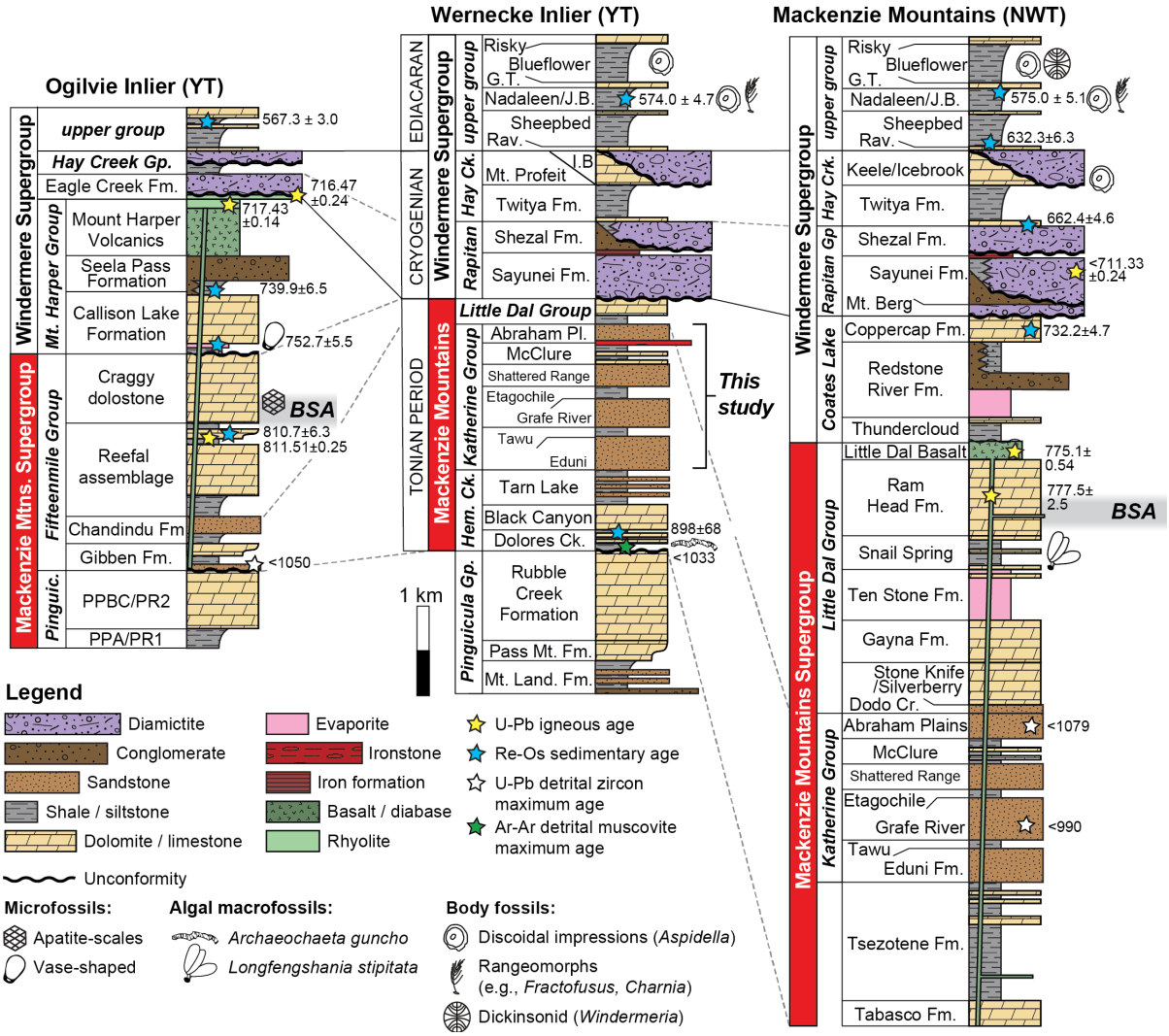

Fig. 2. Stratigraphy of the Mesoproterozoic–Neoproterozoic sedimentary basins of northern Laurentia, including the Coal Creek and Wernecke inliers of Yukon Territory (YT), and the Mackenzie Mountains of Northwest Territories (NWT). Highlighted are the available geochronological data (ages in Ma) and possible inter-basin correlations (after Rooney et al., 2020; Maloney et al., 2021), as well as the stratigraphic horizon of the ca. 810–800 Ma Bitter Springs carbonate carbon isotope anomaly ('BSA') (as documented in the Ogilvie and Mackenzie Mountains; Halverson, 2006; Macdonald et al., 2010; Halverson et al., 2022) highlighted in grey. Also shown is the distribution of fossils (Hofmann et al., 1983; Hofmann, 1985; Carbone et al., 2015; Cohen et al., 2017a; Cohen et al., 2017b; Rooney et al., 2020; Maloney et al., 2023), highlighting the importance of this time period for eukaryotic evolution and ecosystem complexity.

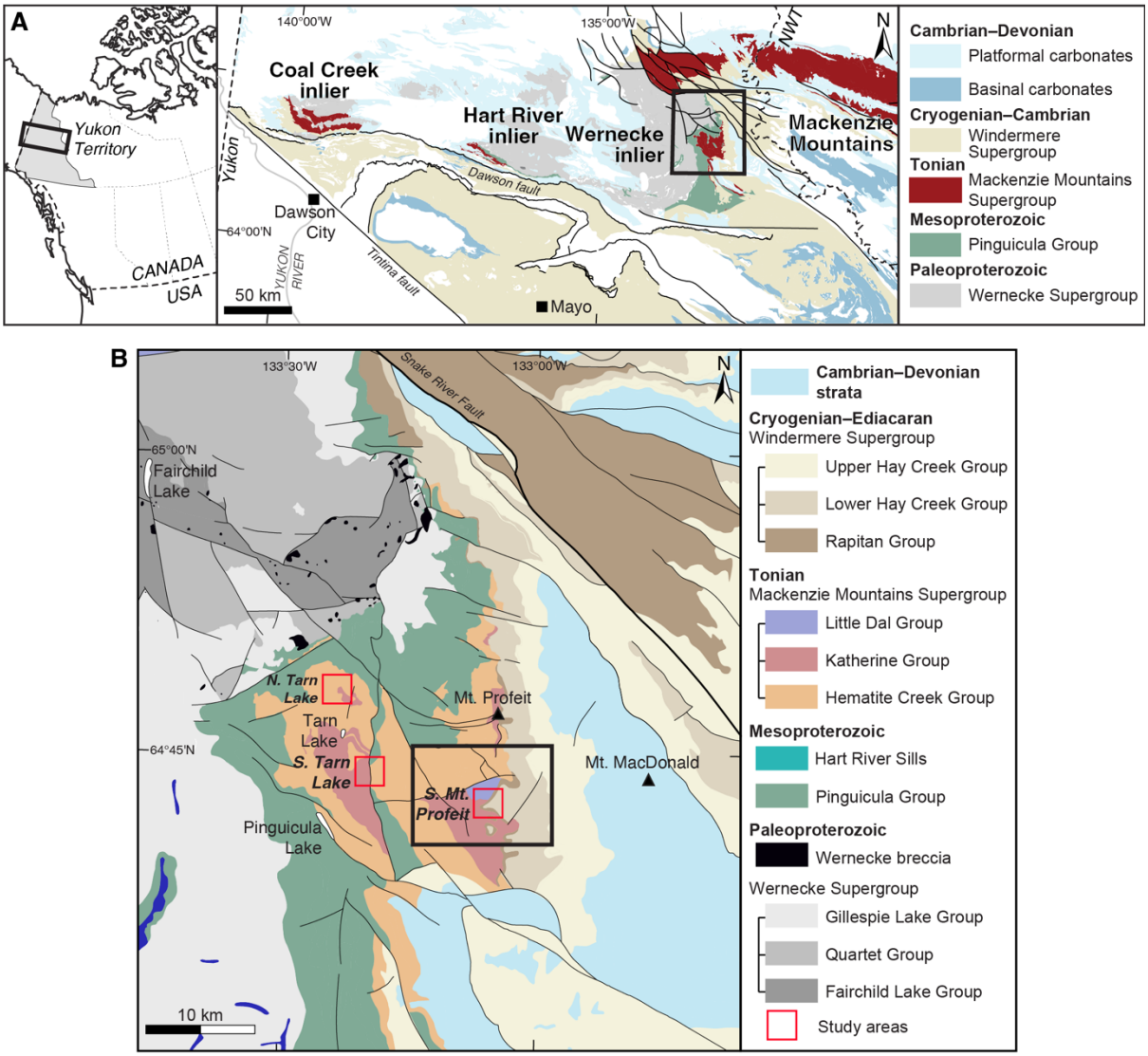

Fig. 3. A. Simplified geological map (after Colpron et al., 2016) of the Proterozoic–Palaeozoic strata of the Coal Creek, Hart River and Wernecke inliers, with the black rectangle highlighting the study area in the Wernecke Inlier. **B.** Geological map of the Bonnet Plume Range within the Wernecke Inlier (modified from the Bedrock Geology Dataset, Yukon Geological Survey, 2020; after Maloney et al., 2021), showing the location of the study areas of the Katherine Group stratigraphy (red squares; N. Tarn Lake, S. Tarn Lake, and S. Mt. Profeit), and the location of the map of the ironstone-bearing strata south of Mount Profeit (black rectangle; see Fig. 5).

2.1 Katherine Group

The Katherine Group is formally defined in the Mackenzie Mountains, where its thickness ranges from ~300–1300 m (Long and Turner, 2012). The type section for the Katherine Group is in the Glacier Lake area (Thundercloud Range; Mackenzie Mountains) near the Keele River (62°37'57"N, 126°34'15"W; Gabrielse et al., 1973; Long and Turner, 2012). In this area, the Katherine Group was originally subdivided into the informal units K1–K7 (Aitken et al., 1978b) and subsequently defined as the Eduni, Tawu, Grafe River, Etagochile, Shattered Range, McClure, and Abraham Plains formations (in stratigraphically ascending order; Long and Turner, 2012). The formations of the Katherine Group alternate between formations interpreted to have been deposited predominantly in fluviodeltaic settings (Eduni; Grafe River; Shattered Range; and Abraham Plains formations), and shallow-marine shelf settings (Tawu; Etagochile; and McClure formations; Aitken et al., 1978b; Long, 2011b; Long and Turner, 2012). Although the Katherine Group remains informally defined in the Wernecke Inlier, the overall stratigraphic framework appears to be similar to that of the Mackenzie Mountains (Turner, 2011b).

The Eduni, Grafe River and Abraham Plains formations are dominated by planar cross-laminated sandstones with a sheet-like geometry, interbedded with minor mudstones (Gabrielse et al., 1973; Aitken et al., 1978b; Long, 2011b). In addition to sheet-like units, sandstone beds are channelised

in places, with channels that are generally only a few metres deep and hundreds of metres wide (Long, 2011b; Long and Turner, 2012). These sandstones are interpreted to have been deposited by the lateral migration of ephemeral–perennial, sandy-braided rivers, with the fine-grained siliciclastics representing overbank deposits, abandoned channel fill, and tidal incursions (Long, 2011b; Long and Turner, 2012). The intervening Tawu, Etagochile and McClure formations typically have basal dark mudstones, increasingly interbedded with thin, planar-bedded sandstone up-section (occasionally featuring wavy and ripple cross lamination), with desiccation cracks and occasional carbonate-bearing intervals including stromatolite bioherms (Gabrielse et al., 1973; Aitken et al., 1978b; Long, 2011b). These units are interpreted to record marine transgression, leading to the deposition of shallow-shelf sediments, followed by a highstand shoaling to intertidal deposits (Long, 2011b; Long and Turner, 2012). In both fluvial- and marine-dominated units, local features such as current lineations, swash marks and reversing palaeocurrent indicators are interpreted as beach deposits (Long, 2011b). The distinctive stromatolite bioherms of the McClure Formation in particular can be traced extensively (Gabrielse et al., 1973; Aitken et al., 1978a), and this marker interval has been used to support a stratigraphic correlation between the Kathrine Group and the Rae Group in the Amundsen Basin to the north (Aitken et al., 1978a; Rainbird et al., 1996; Long et al., 2008).

The contact with the overlying Little Dal Group is sharp, and likely represents a transgressive event (Long, 2011b). In the study area, the basal Little Dal Group comprises siderite- and organic carbon-rich shales overlain by calcareous mudstones interpreted to represent deposition below storm-wave base (Turner, 2011b; Long and Turner, 2012). In the Mackenzie Mountains, the basal Little Dal features halite casts and ripple cross lamination and is considered to record a transition from nearshore environments that are influenced by fluvial processes to fully marine sedimentation (Aitken, 1981; Turner et al., 1997; Turner, 2011a). This study focuses on an ironstone-bearing interval in the Wernecke Inlier which is tentatively correlated with the McClure and Abraham Plains formations of the Katherine Group.

3. Materials and methods

A field study of the upper Katherine Group was conducted in the Bonnet Plume Range (Wernecke Mountains, First Nation of Nacho Nyak Dun Traditional Territory). Despite mapping by previous researchers of the Katherine Group throughout the Wernecke Mountains and Mackenzie Mountains (Gabrielse et al., 1973; Aitken et al., 1978b; Long, 2011b; Long and Turner, 2012), thus far ironstone has only been identified in the glacial valley and surrounding ridges south of Mount Profeit (64.71, -133.11°; Fig. 5). We focused on this locality and measured stratigraphic sections through the upper Katherine Group into the basal Little Dal Group. We collected eighty-five samples of the Katherine Group ironstones and host lithologies from surface outcrop, avoiding weathered or deformed outcrops.

3.1 Petrography and mineralogy

Samples were petrographically analysed using optical and scanning electron microscopy. Energy dispersive spectroscopy analyses were undertaken on coated samples on a JEOL JXA-8530F and a Philips FEI XL30 environmental scanning electron microscope equipped with an OXFORD INCA energy-dispersive X-ray spectrometer at the School of Geography, Earth and Atmospheric Sciences (University of Melbourne). An accelerating voltage of 15 kV and a probe current of 3.7nA for the acquisition were employed for element maps and point analyses. After representative petrographic analyses, cut hand samples were cleaned and drilled targeting authigenic phases (i.e., avoiding weathered surfaces and veins). Sample powders were subsequently analysed for their mineralogy using X-ray diffraction at the McGill Chemistry Characterization Facility, and Panalytical software was used to interpret diffraction patterns.

3.2 Whole rock major and trace elements

Following petrographic analysis, seventy-one samples were selected for whole-rock geochemical analyses. To avoid contamination, all weathered surfaces were removed and cut surfaces were cleaned with carborundum paper. These samples were then crushed to gravel size using a rock hammer, ensuring that all metal surfaces were covered to avoid direct contact, and subsequently pulverised to a fine powder (< 5 μm) using an agate ring mill.

For major element geochemistry, samples were analysed via fusion X-ray fluorescence (XRF) spectrometry according to standard procedures by Australian Laboratory Services (Brisbane, Australia).

For whole-rock trace element analysis, samples were analysed following methods outlined in (Wang et al., 2023). Sample powders were first ignited at 550°C to remove organic matter. Approximately 50 mg of sample powder was dissolved in Teflon beakers using concentrated HF and HNO_3 for 24 hours, dried down, and dissolved again using Aqua Regia. Final residues were dissolved in 5 ml 6 N HCl for stock solutions for geochemical analyses. A small aliquot (~10 µl) out of 5 ml 6 N HCl was then dried down and brought up to 4 ml with 5% HNO_3 containing an internal spike of 1 ppb indium. The resulting solutions were analysed in the Department of Earth and Planetary Sciences at Yale University using a ThermoFisher Scientific Element XR inductively coupled plasma-mass spectrometer (ICP-MS) to determine selected trace elements using a quartz spray chamber sample introduction system. Measurement precision (reported as 2σ uncertainty) was determined using duplicate analyses of samples and was generally less than ±5 % for major and trace elements. External accuracy was determined by analysing internationally certified reference materials from iron-rich United States Geological Survey (USGS) geostandards BHVO-2 (Hawaiian Basalt) and NOD-A-1 (Atlantic Ocean ferromanganese nodule) measured alongside samples, which were within 5 % of their reported values (Flanagan and Gottfried, 1980; Jochum et al., 2016).

3.3 Neodymium isotope analyses

Select sample aliquots prepared for bulk-rock trace element analyses were also chosen for Nd isotope analyses. Isotopic calculations were performed using the Nd and Sm contents measured in the ICP-MS trace element analyses described in the previous section. A three-stage chromatography process was used to isolate Nd and Sm, using AG1X8 200-400 mesh, Eichrom TRU SPS 50-100 µm, and Eichrom LN 50-100 µm anion exchange resins. The resulting Nd and Sm separates were taken up in 2% HNO_3 for isotopic analysis, conducted on a Nu Plasma II Multiple Collector ICP-MS at Geotop/Université du Québec à Montréal. Long-term averages for Nd isotope reference JNdi-1 yielded $^{143}Nd/^{144}Nd$ values of 0.512096 ± 0.000070 (2σ), which is within error of reported values (Tanaka et al., 2000).

Radiogenic ^{143}Nd is produced by the decay of ^{147}Sm, and because of the geochemical similarity between Nd and Sm, the $^{143}Nd/^{144}Nd$ ratio of a rock sample correlates with age. Here, the age of the rocks (t) is factored in by accounting for the decay of ^{147}Sm (using the decay constant, λ, from Goldstein et al., 1984) according to the following:

$$^{143}Nd/^{144}Nd = (^{143}Nd/^{144}Nd - {}^{147}Sm/^{144}Nd) \times (e^{\lambda t} - 1) \quad (1)$$

While the age of the Katherine ironstone is not well constrained, for the purposes of this study, an age of 850 Ma is assumed based upon the 898 ± 68 Ma Re–Os shale age from the underlying Hematite Creek Group (Fig. 2; Maloney et al., 2021). Following this, the Nd isotopic ratio is here expressed in epsilon notation normalised to the chondritic $^{143}Nd/^{144}Nd$ value (represented by the chondritic uniform reservoir, CHUR; Jacobsen and Wasserburg, 1980):

$$\varepsilon Nd(t) = [(^{143}Nd/^{144}Nd)_{sample}/(^{143}Nd/^{144}Nd)_{CHUR} - 1] \times 10^4 \quad (2)$$

3.4 Total organic carbon

To determine total organic carbon (TOC) concentrations, approximately 1.5 g of sample powder was leached twice in 2M HCl for twelve hours to remove carbonate minerals, rinsed with distilled water, and dried. Subsequently, TOC contents were determined using an Eltra CS-800 Carbon–Sulfur Analyzer following methods outlined in Kunzmann et al. (2015). Accuracy and reproducibility were monitored via duplicate analyses and certified reference materials, and measurement precision was better than ±8 %. Measured values for USGS shale standards SBC-1 (1.06 ± 0.08; n = 3) and SCo-1 (0.35 ± 0.03; n = 3) were within error of their reported values (Dennen et al., 2006; Galy et al., 2007; Fujisaki et al., 2022).

3.5 Iron speciation

Iron speciation analyses were conducted following the methods outlined in Poulton and Canfield (2005). This protocol involves the sequential extraction of Fe from several operationally defined pools, including Fe bound to carbonate (i.e., siderite, ankerite, dolomite; Fe_{carb}), ferric (oxyhydr)oxides (Fe_{ox}), and Fe associated with mixed-valence phases (such as magnetite; Fe_{mag}; Poulton and Canfield 2005). This sequential extraction was conducted on the same 150 mg of powdered rock for each sample. First, the extraction of Fe_{carb} was targeted by reacting samples with a solution of 1M sodium acetate buffered with

acetic acid to pH 4.5 on a shaking table for 48 hours at 50ºC. Second, Fe_{ox} was extracted using a 50 g/l sodium dithionite solution buffered with 0.35M acetic acid and 0.2 M sodium citrate to pH 4.8 on a shaking table at room temperature for 2 hours. Third, Fe_{mag} was extracted using a 0.2 M ammonium oxalate — 0.17 M oxalic acid solution buffered with ammonium hydroxide to pH 3.2 for 6 hours on a shaking table at room temperature. Leachates from these extractions were diluted with 2% HNO3 and analysed using a PerkinElmer AAnalyst 100 Flame Atomic Adsorption Spectrometer. Finally, in order to quantify Fe associated with pyrite (Fe_{py}), sulphide was liberated by $CrCl_2$ reduction (following the method outlined in Canfield et al., 1986), trapped as Ag_2S, and quantified gravimetrically (assuming FeS_2 stoichiometry). Independently analysed shale samples from Kunzmann et al. (2015) were included in all steps of the sequential extractions as external standards, and results were within 10% previously published values. Measurement precision, as determined from analyses of duplicate samples subjected to the same extraction processes, was generally better than ±15 % (2σ uncertainty). The operationally defined "highly reactive Fe" (Fe_{HR}) pool was calculated as the sum total of the Fe extracted by the different sequential leach techniques (i.e., $Fe_{HR} = Fe_{carb} + Fe_{ox} + Fe_{mag} + Fe_{py}$).

3.6 In-situ major and trace elements

For in-situ trace element analysis, samples of the Katherine ironstone (n = 21) were prepared as polished thick (~100 µm) sections, and an optical microscope was used to select 121 spots for in situ analysis. In situ major element analysis was conducted at the School of Geography, Earth and Atmospheric Sciences (University of Melbourne) using a Cameca SX50 Electron Microprobe, with an accelerating voltage of 15 kV, a beam current of 35 nA, spot size of 25 µm and a count time of 80 seconds. Limits of detection were generally better than 0.05 elemental wt% for all elements analysed. Reference materials MGOX, ALOX, WOL9 and HEM6 were used as calibration standards. The same spots analysed by microprobe were also analysed on a Helex 193 nm ArF excimer laser ablation system connected to an Agilent 7700× quadrupole ICP-MS at the School of Earth Sciences (University of Melbourne). Operating conditions included a source sample rate of 1.7 Hz, an ablation time of 60 seconds and a 72 µm spot size. National Institute of Standards reference material NIST612 (glass) and USGS international standards BCR-2 (Columbia River basalt) and BHVO-2 (Hawaiian basalt) were analysed regularly throughout the sequence. Data was reduced by Iolite Software (Paton et al., 2011) following the Trace Elements Scheme (Woodhead et al., 2007). The Fe values determined by electron microprobe analysis were used for internal standard calibration.

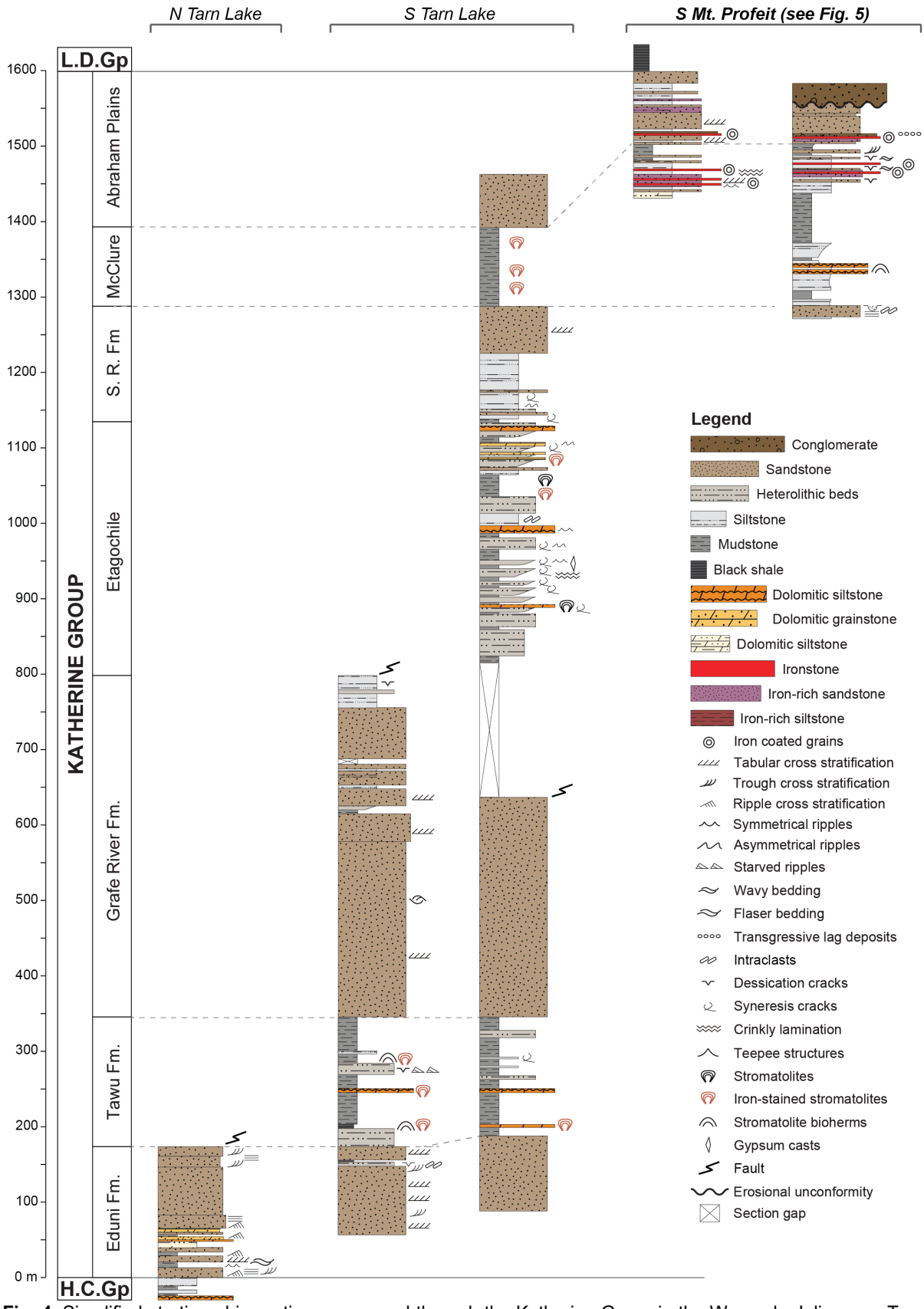

Fig. 4. Simplified stratigraphic sections measured through the Katherine Group in the Wernecke Inlier near Tarn Lake and Mount Profeit (see Fig. 3 for section locations). Note that the assignment of formation names is tentative, and further work is required to elucidate the thickness and facies relationships of the different units of the Katherine Group in the Wernecke Inlier. H.C.—Hematite Creek; Gp—Group, Fm.—Formation, S.R.—Shattered Range; L.D.—Little Dal.

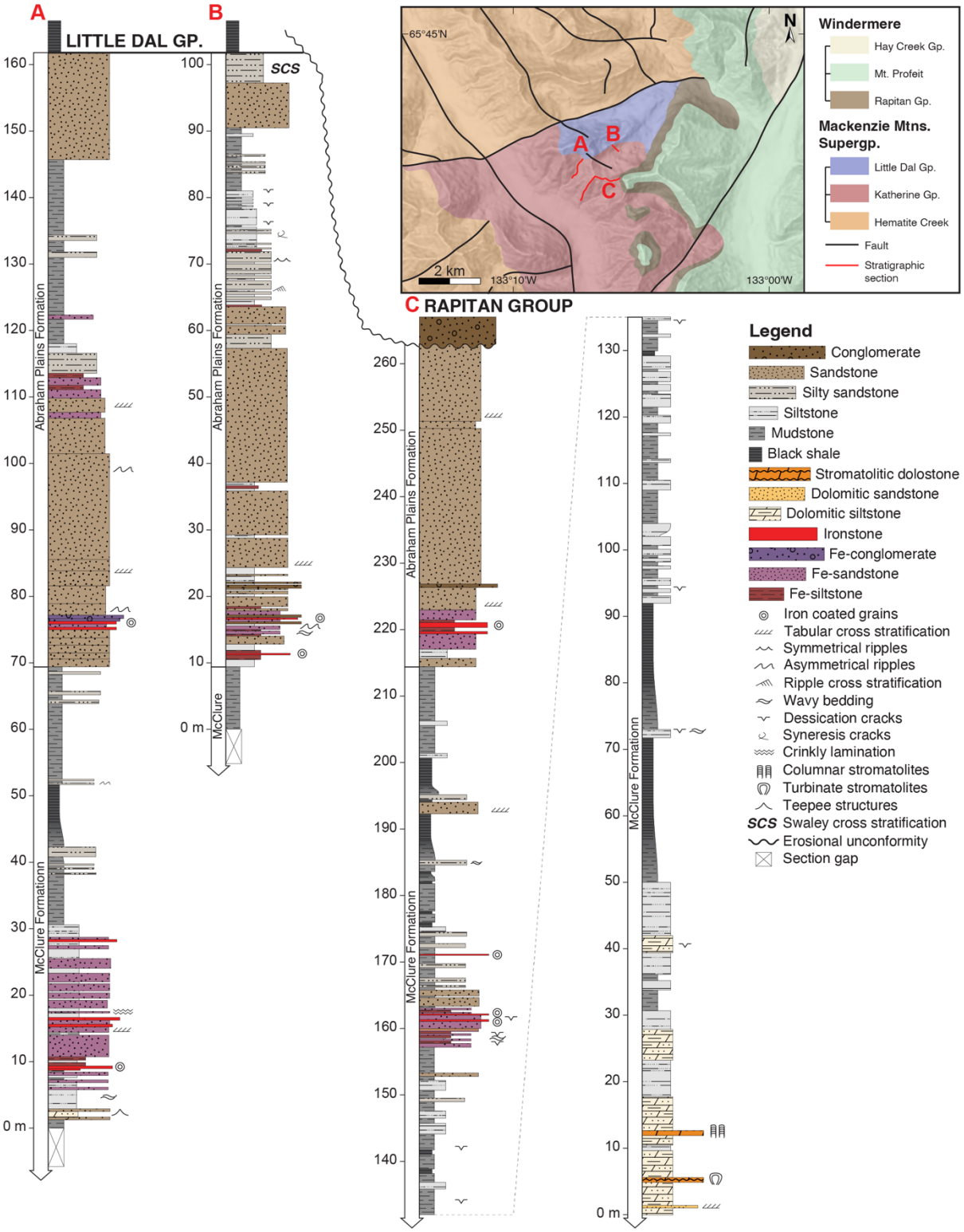

Fig. 5. Stratigraphic sections measured through the upper Katherine Group (McClure and Abraham Plains formations) to the conformable contact with the overlying Little Dal Group (sections A and B), or the unconformable contact with the Rapitan Group (section C).

4. Sedimentology and petrography

In the study area (Fig. 3), the Katherine Group contains ironstone horizons between ~150–30 m below the Little Dal Group (though locally this contact is obscured by an erosional unconformity; Figs. 3–4). For the purposes of this discussion, we adopt the nomenclature of Long and Turner (2012) as defined in the Mackenzie Mountains. The stratigraphic assignment at the formation level is based on the

stratigraphic closeness to the conformably overlying Little Dal Group, as well as features diagnostic of the McClure Formation (orange-weathering stromatolites). Here, we describe the sedimentology and petrography of this ironstone-bearing interval and interpret the depositional environment of these units.

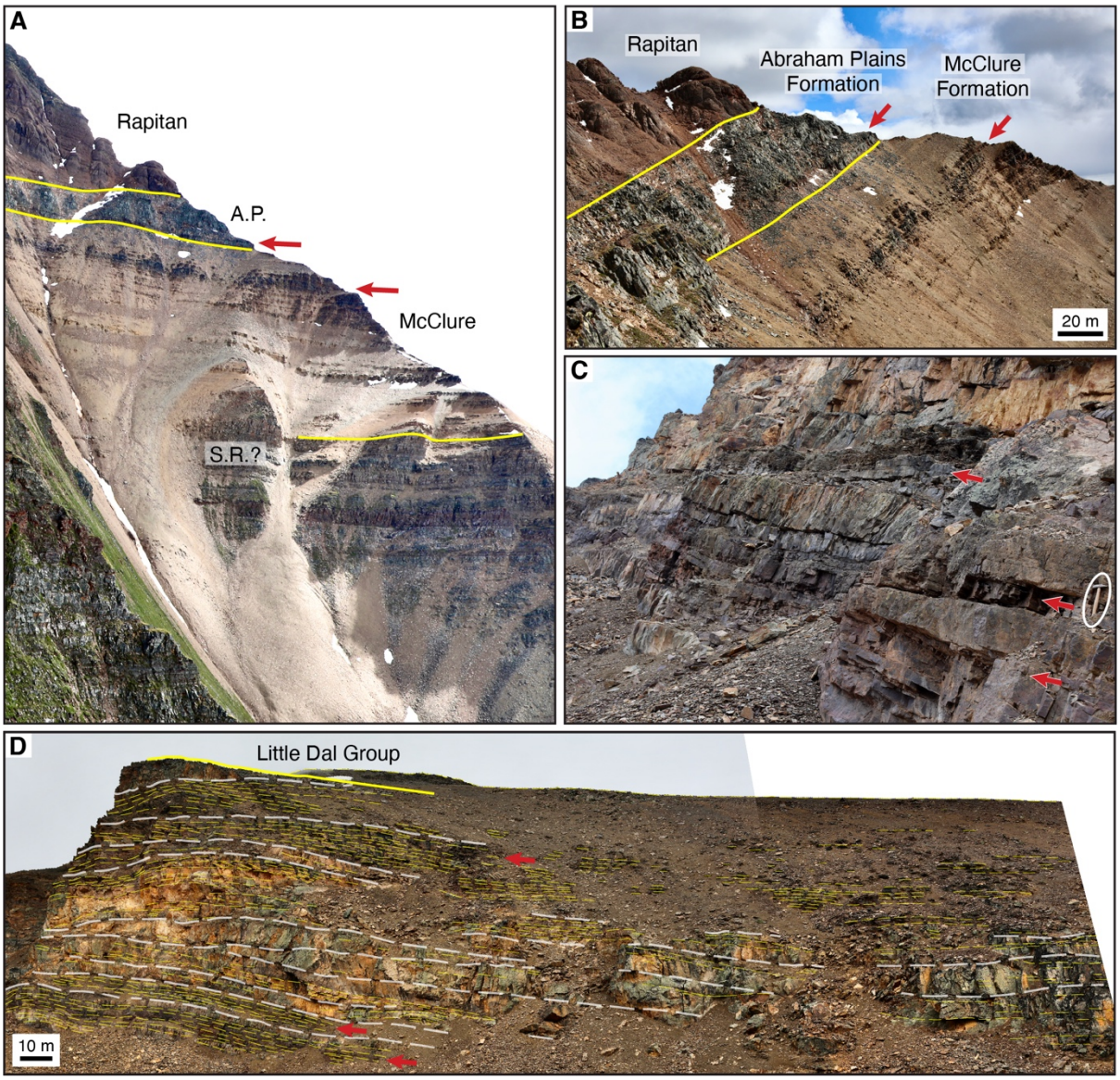

Fig. 6. Stratigraphic context of the ironstone horizons within the upper Katherine Group. Red arrows indicate ironstone horizons; yellow lines indicate formation boundaries. **A.** View facing east showing the upper Katherine Group in the southeast of the study area, where the upper Abraham Plains Formation is truncated by an erosional unconformity and overlain by conglomerates of the Cryogenian Rapitan Group. Note that the placement of the stratigraphic boundary between the McClure Formation and the underlying unit (equivalent to the Shattered Range Formation; S.R.) is approximate. **B.** A closer view of the upper Katherine stratigraphy shown in the ridge in A, with approximately 40 metres of stratigraphy missing compared to the northern part of the study area (section C in Figure 5). **C.** Ironstone horizons interbedded with quartz arenites of the basal Abraham Plains Formation; photo taken from the lower part of the stratigraphy depicted in D. **D.** View facing north of the upper Abraham Plains Formation in the northern part of the South Mount Profeit study area (section B in Figure 5), dominated by tabular cross-bedded quartz arenite and conformably overlain by recessive black shales of the Little Dal Group. Hammer in C is 33 cm long.

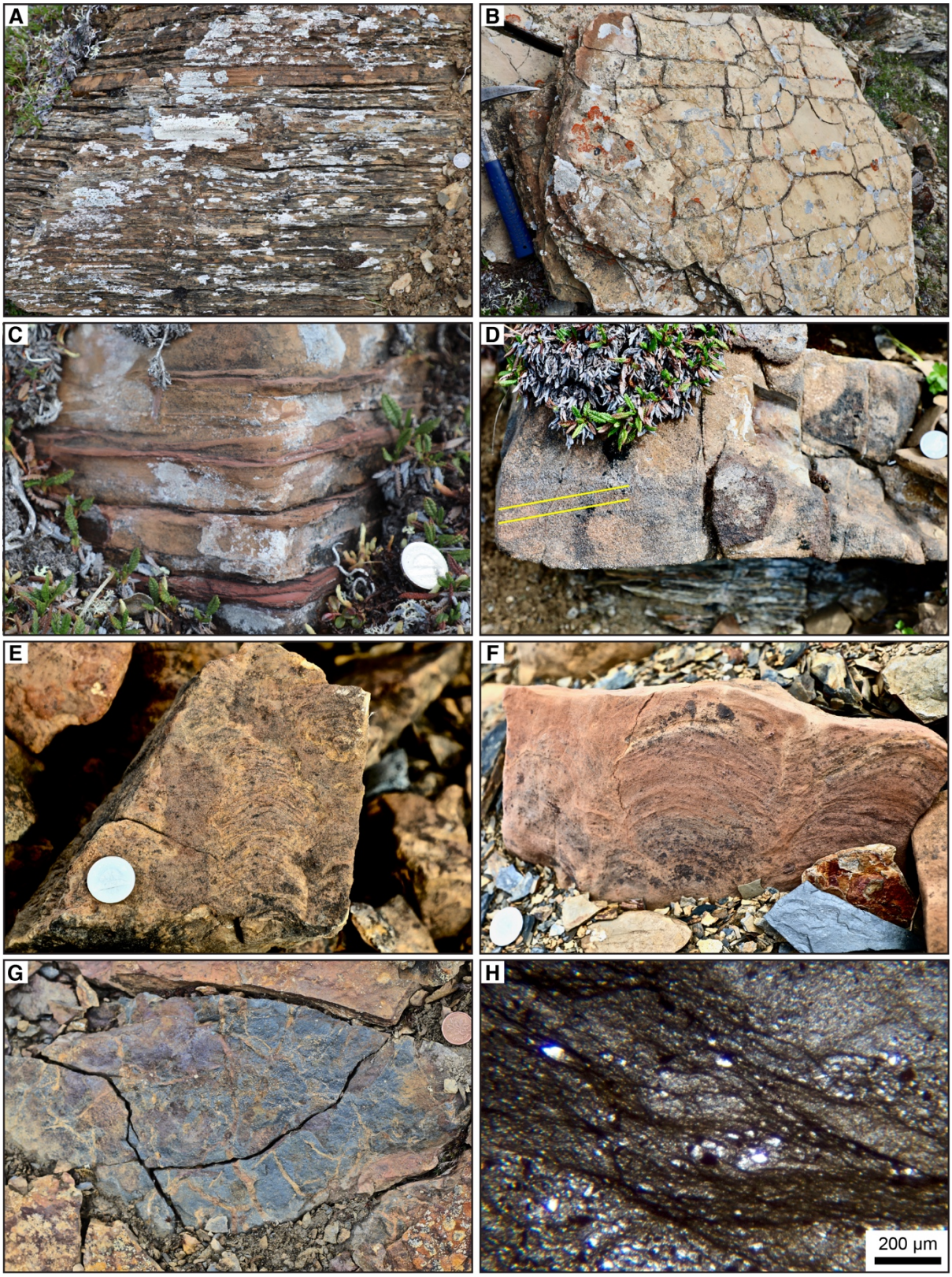

Fig. 7. Sedimentary features of the McClure Formation. **A.** Planar laminated dolomitic siltstone with mudstone interbeds, within the carbonate facies of the lower McClure Formation. **B.** Plan view of embryo tepee structures within dolomitic siltstone. **C.** Dolarenite with mud drapes. **D.** Dolomitic sandstone with tabular cross lamination (highlighted by yellow lines). **E.** Columnar stromatolites within dolobindstone beds. **F.** Turbinate stromatolites. **G.** Plan-view photo of a bedding plane of grey silty mudstone showing polygonal desiccation cracks. **G.** Transmitted light photomicrograph of mudstone with irregular, discontinuous carbonaceous laminae, and silt lenses. Coin in A, C–F is 21.2 mm, coin in G is 19 mm. Hammer in B is 33 cm long.

4.1 McClure Formation

Field and petrographic observations

In the study area, the McClure Formation comprises a carbonate-bearing facies (which predominates in the lower ~50 metres of the formation), a fine-grained siliciclastic facies (which predominates in the remainder of the formation; Figs. 4–5), and a ferruginous facies.

The carbonate-bearing facies comprises dolomitic siltstone, mudstone, dolomitic sandstone, and stromatolitic dolobindstone. In places, the dolomitic siltstones are wavy-laminated and contain rare tepee structures (Fig. 7A–B). Dolarenite and dolomitic sandstone beds are orange–buff-weathering, and can have mud drapes (Fig. 7C), erosive bases and tabular cross lamination (Fig. 7D). The dolobindstone units comprise bulbous and turbinate stromatolites which are typically <30 cm in height and <20 cm wide, with a synoptic relief of 1–3 cm (Fig. 7E–F). The columnar stromatolites are comparable to the branching, columnar stromatolites (*Inzeria*) reported by Long and Turner (2012) in the type section of the McClure Formation in the Mackenzie Mountains, as well as other middle Tonian stratigraphic successions globally (e.g., Glaessner et al., 1969). Mud drapes can also be observed overlying these stromatolite units, which are often laterally discontinuous (i.e., bioherms) in the study area despite typically forming continuous biostromes elsewhere in the McClure Formation (Long, 2011b). Individual laminae are crinkly with minor fine sand trapped within the carbonate matrix, and convexity often increases upwards. Minor parallel, columnar stromatolites with constringed variability are ~3 cm in width and <20 cm in height (Fig. 7E). Oncoids associated with the stromatolites in the type section of the McClure Formation (Turner and Long, 2012) were not observed in the study area.

The fine-grained siliciclastic facies are characterised by silty mudstone and siltstone with subordinate horizons of sandstone. The mudstones are dark grey and can be reworked, with intraclasts, convolute bedding, and crinkled, discontinuous laminae of carbonaceous material (Fig. 7H). Locally, these dark-grey mudstone horizons have polygonal mudcracks (Fig. 7G). Less commonly, mudstones and siltstones are red-weathering (hematitic). Siltstones and silty sandstones are typically planar laminated, with minor wavy bedding, and—similar to the dolomitic siltstones—can be organised into centimetre-scale packages of siltstone capped by thin mud drapes (i.e., heterolithic bedding). The XRD data indicates that the most common phyllosilicates of the McClure Formation mudstones and siltstones are kaolinite and illite with highly variable amounts of berthierine, hematite, calcite and apatite (Fig. 8). The McClure Formation mudstones contain 0.28–0.56 % TOC (average 0.39 wt%; n = 6).

Ferruginous facies (including oolitic ironstone and ferruginous sandstones and siltstones) are present in the upper McClure Formation and continue into the lower Abraham Plains Formation (Fig. 4); the sedimentology of the ferruginous facies is discussed in detail in Section 4.4. The uppermost ~30 metres of the McClure Formation marks the first appearance of thicker sandstone with wavy bedding, tabular and trough cross-lamination (Fig. 5). Given that this cross-bedded sandstone facies is abundant in the Abraham Plains Formation, this indicates a transitional contact (Long, 2011b).

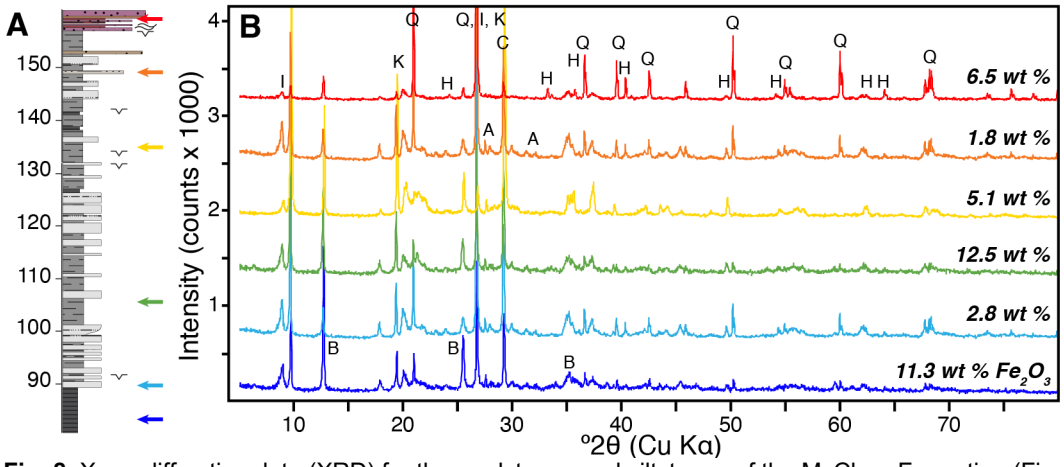

Fig. 8. X-ray diffraction data (XRD) for the mudstones and siltstones of the McClure Formation (Fig. 5 Section C). **A.** The coloured arrows show the stratigraphic level of the respective samples analysed, with the colour corresponding to the XRD spectrum shown in B. **B.** XRD spectra for bulk-rock sample powders, showing various amounts of authigenic and detrital mineral components (B = berthierine; K = kaolinite; I = illite; Q = quartz; H = hematite; C = calcite; A = apatite). Also shown are the bulk rock Fe contents (here shown as wt % Fe_2O_3 as

determined by X-ray fluorescence); the samples with greater Fe content appear to be relatively rich in Fe phyllosilicates such as berthierine, and lack peaks corresponding to Fe carbonates or sulphides.

Interpretation

Based upon the above observations from the study area, we suggest that much of the McClure Formation was deposited in a shallow, protected coastal setting (embayment) that was tidally influenced. This environment experienced temporally variable siliciclastic input, and was subject to episodic high energy conditions.

The lower, carbonate-dominated part of the McClure Formation has previously been interpreted to represent deposition in a shallow subtidal setting (Long, 2011b). Consistent with this interpretation, we suggest that the carbonate facies of the lower McClure Formation, was deposited in a shallow subtidal to peritidal (inner shelf) setting. The bulbous, turbinate and irregular columnar stromatolites with low synoptic relief are similar to those considered to be typical of Precambrian nearshore marine settings (Grotzinger, 1989), and likely accreted due to microbial growth and concomitant carbonate precipitation during periods of relative starvation of clastic detritus. The tepee structures are embryo tepees (sensu Assereto and Kendall, 1977), with limited development of the expansion process indicated by the lack of extensive disrupted fabrics and intraclasts. These are similar to the embryo tepees observed in Shark Bay (Western Australia; Davies, 1970), which is a stromatolitic, carbonate barrier-lagoon system (Dalrymple and Rivers, 2023). Tepee structures are considered to form in peritidal environments via the penecontemporaneous thermal expansion of carbonate crusts, possibly enhanced by synsedimentary carbonate precipitation and the associated displacive force of crystallisation (Assereto and Kendall, 1977; Kendall and Warren, 1987). The erosive base observed in some of the dolomitic sandstone beds (Fig. 7D) may indicate deposition in shallow tidal channels, and a tidal influence on deposition is supported by the observation of mud drapes (Tucker and Wright, 1990; O'Connell et al., 2022).

For the fine-grained siliciclastic facies, the mudstones were deposited due to low-energy suspension settling of clays, with the heterolithic bedding indicative of a tidal influence on deposition (Dalrymple and Choi, 2007). The polygonal cracks (which are common in this unit in other areas; Long and Turner, 2012) are interpreted to indicate desiccation during periodic subaerial exposure. The intraclasts of the mudstones were likely reworked by waves during episodic high energy conditions, with the silt and sand content indicating proximal detrital input. The minor tabular cross-bedded sandstones were deposited by the migration of subaqueous sand dunes due to tidal currents. The organic matter contents of the McClure Formation mudstones are comparable to other Tonian grey–black shales (median TOC = 0.25 wt%; Sperling and Stockey, 2018; Woltz et al., 2020), suggesting that organic matter loading was not especially high. However, carbonaceous laminae are common in the fine-grained siliciclastics of the McClure Formation, and often have a wavy-crinkly lamination (Fig. 7H) comparable to those in microbial mat deposits (e.g., Schieber, 1986). Microbial mats are a common feature of the intertidal–supratidal zone of modern siliciclastic tidal flats (Flemming, 2012). While tidal flat environments are often evaporitic, the lack of evidence for evaporites (including halite casts) in this facies likely points to a humid climate during deposition (Rankey and Berkeley, 2012; O'Connell et al., 2020), consistent with previous interpretations of the Katherine Group (Long, 2011a; Turner and Bekker, 2016).

The predominance of fine-grained lithologies with tidal features in both facies (i.e., dolomitic siltstones and mudstone)—and the rarity of well-developed cross bedding or wave ripples—demonstrates that the McClure Formation was deposited in a relatively quiescent, low-energy environment. Many modern mixed siliciclastic–carbonate tidal flats develop via settling during scour lags (Dalrymple and Choi, 2007) as a result of low levels of wave action, either in settings with low depositional slopes protected by barrier islands or spits, or in restricted embayments such as estuaries or back-barrier lagoons (Van Straaten, 1961; Dashtgard et al., 2021; Dalrymple and Rivers, 2023). Mudflats in tide-dominated embayments often overlie channelised facies, however, they can also develop over shoreface or delta front systems (Dashtgard et al., 2021). Muddy tidal flats can also accumulate in open-coast environments (such as those associated with the Changjiang and Amazon deltas), where the discharge of mud from the associated mega-deltas leads to the development of an extensive, fluidised mud layer which dampens wave energy (Anthony et al., 2010). These wave-influenced and tide-dominated muddy tidal flats have fewer tidal-channel deposits and more abundant storm-generated structures compared to back-barrier tidal flats, and these are often found associated with tide-dominated estuaries (Fan, 2012).

Regardless of the coastal geomorphology, the McClure Formation adds to the growing list of examples of muddy tidal flats prior to the evolution of land plants (O'Connell et al., 2022). Overall, the

McClure Formation represents a regression up-section from low-energy, shallow subtidal facies to humid, intertidal mudflat facies. This is consistent with observations from the Mackenzie Mountains, where repeated cycles of stromatolitic bioherms have been interpreted to record higher order variations in relative sea level change, ultimately resulting in shoaling to intertidal conditions near the top of the formation (Long, 2011b; Long and Turner, 2012).

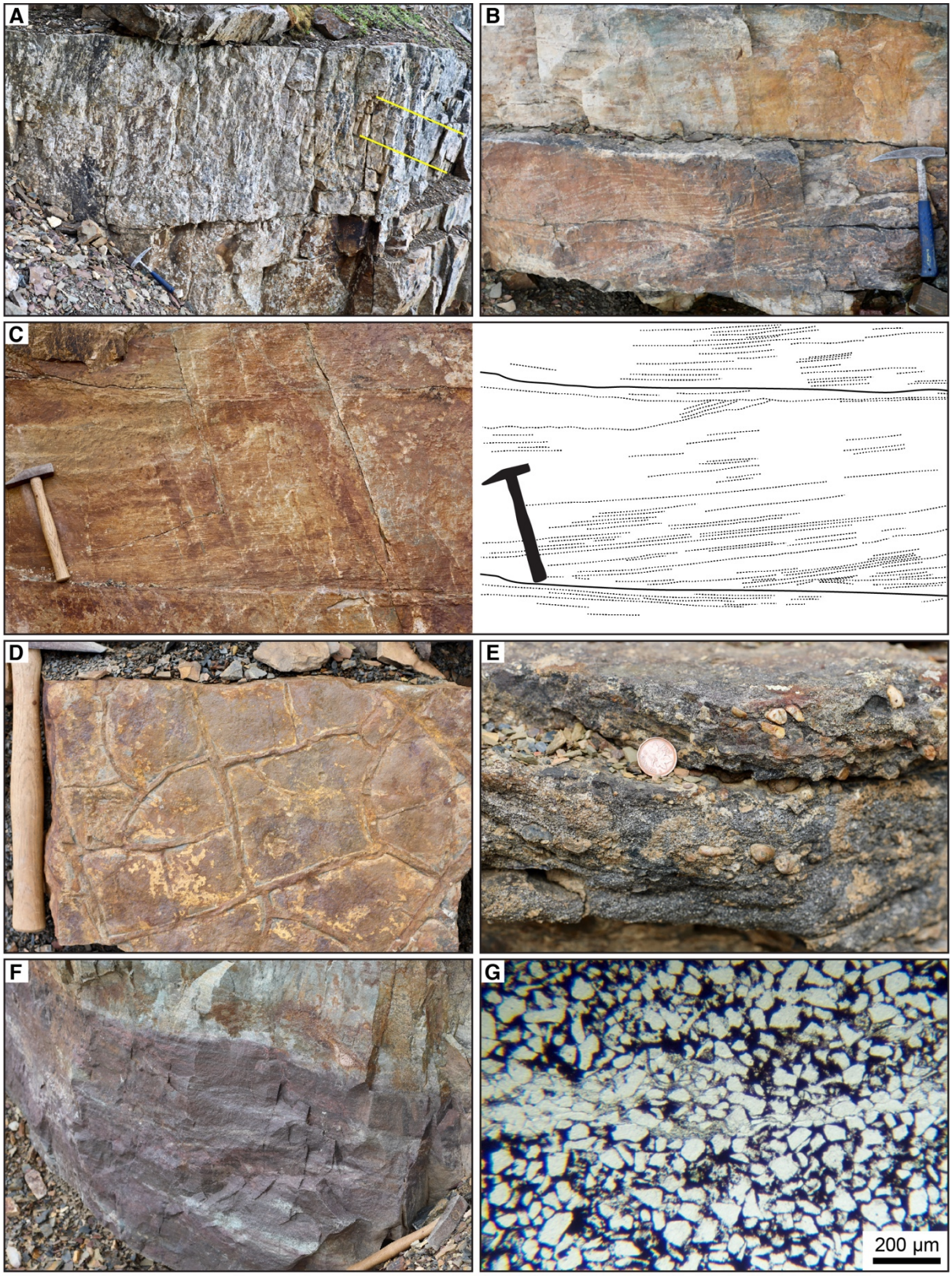

Fig. 9. Sedimentary features of the Abraham Plains Formation. **A.** Characteristic thick-bedded, tabular cross-laminated quartz arenites, with angular basal contacts (highlighted by yellow lines), with a predominant palaeocurrent direction trending towards the present-day east. **B.** Cross-laminated sandstones with palaeocurrent direction trending towards the present-day west. **C.** Cross lamination in sandstone featuring reactivation surfaces and tangential basal contacts. **D.** Plan view of the underside of a sandstone bed, showing positive relief structures highlighting polygonal cracks. **E.** Pebble clasts within the sandy–gravelly matrix of a conglomerate lens. **F.** Diffuse contact between lower hematite-cemented sandstone (purple) with upper non-ferruginous sandstone (grey–green). **G.** Transmitted light photomicrograph of ferruginous sandstone, showing angular quartz grains supported by hematite cement. Hammers in A–D and F are 33 cm long, coin in E is 19 mm wide.

4.2 Abraham Plains Formation

Field and petrographic observations

The Abraham Plains Formation is in transitional contact with the underlying McClure Formation, defined by the increasing abundance of sandstone relative to mudstone (Fig. 5). We interpret the base of the Abraham Plains Formation to be marked by the first appearance of the cross-stratified sandstone facies dominated by thick (>2 m) quartz arenite beds (Fig. 5), which is characteristic of the Abraham Plains Formation (Long and Turner, 2012). These cross-stratified sandstones are generally laterally extensive over hundreds of metres and lateral facies variations were rarely observed on the outcrop scale within the study area. In some cases, the tracing of first-order erosional surfaces can highlight the lenticular nature of these of sand bodies with a high aspect ratio (width:thickness) exceeding 40:1 (Fig. 6D). Continuous packages of quartz arenite beds can exceed 40 metres in thickness, punctuated by recessive intervals of the fine-grained siliclastic facies (mudstone and minor interbedded sandstone and siltstone). Rare, thin (<30 cm) lenses of conglomerate occur near the base of the Abraham Plains Formation, with a gravelly matrix supporting sandy–pebble-sized quartz and feldspar clasts (Fig. 9E). Sand casts of large-scale polygonal cracks can be observed on the base of sandstone bedding planes.

The quartz arenites are physically mature and well sorted, with rounded to angular grains of fine–medium quartz sand. Other minerals (e.g., alkali and plagioclase feldspars, rutile) contribute only a minor fraction of the detrital grains. Grading is not well developed. The sand grains are cemented by quartz, with hematite cement occurring in sandstones that are in close stratigraphic association with ironstones (Fig. 9F). The quartz arenite beds have a sheet-like geometry and are most commonly cross stratified, with less common tabular sets of parallel planar stratification. Cross stratification sets are typically ~0.6 m thick, with cosets ~1.5–3 m thick, and foresets have angular to slightly tangential basal contacts (Fig. 9A–B). Channelisation was not observed, with only rare instances of reactivation surfaces. These cross-stratified quartz arenite beds are bounded by planar first-order erosion surfaces, with superposition rarely developed, and are interpreted to represent simple subaqueous dunes (sensu Ashley, 1990). Ripples are undulatory to linguoid, with asymmetrical crests that generally trend towards the present-day east, although westward trending ripples were also observed.

In the study area, the upper half of the Abraham Plains Formation features a greater proportion of siltstone and mudstone relative to sandstone (Fig. 5), and comprises a similar fine-grained siliciclastic facies to that of the McClure Formation. This facies includes mudstones and siltstones with polygonal cracks infilled with sandstone (Fig. 9D), as well as curlicue cracks locally preserved in ripple troughs (Fig. 10B). Rarely, sandstone interbeds within siltstones feature symmetrical ripples. Current lineation, scour and groove casts are present, as well as rare gutter casts and tool marks (Fig. 10C–D).

The uppermost ~15 metres of the Abraham Plains Formation comprises a facies characterised by interbedded bedded sandstones and siltstones, locally featuring swaley cross stratification (Fig. 10E). These facies are in sharp contact with a ~20 metre thick interval of recessive, organic-rich shales of the Little Dal Group. Locally, this contact is erosive and truncates a few metres of the underlying beds at a low angle (Fig. 10E), whereas elsewhere this contact is conformable (Long, 2008; Turner, 2011b). The basal shales of the Little Dal Group contain large (<20 cm) siderite nodules and lack sedimentary structures other than fine, planar lamination. Overlying this black shale interval is a mixed package of interbedded mudstone (with limestone nodules), siltstone, sandstone and marl.

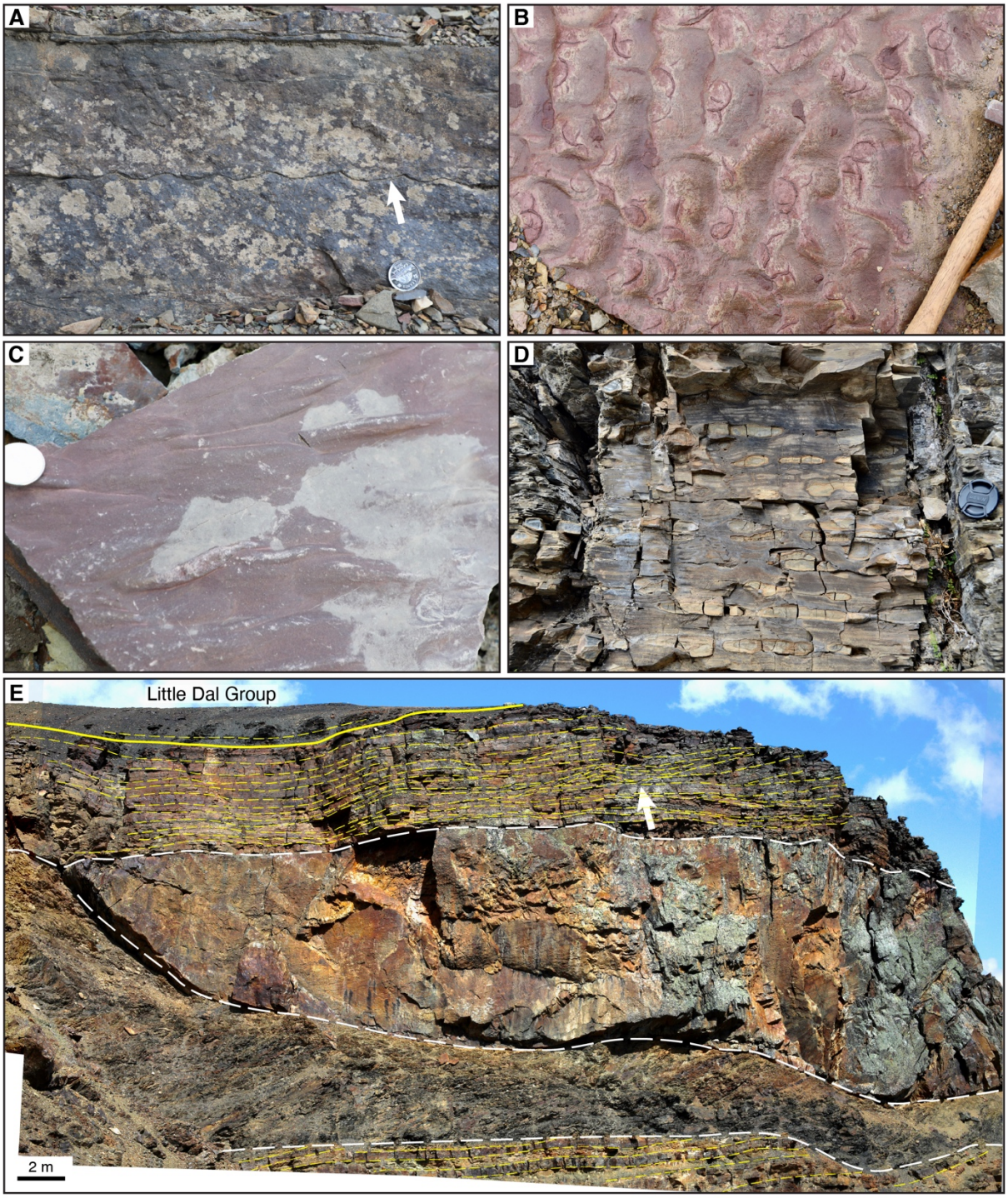

Fig. 10. Sedimentary structures of the Abraham Plains Formation. **A.** Current ripples preserved at the bedding plane interface between two sandstone beds (white arrow). **B.** Plan view of the base of a sandstone bed, featuring curlicue synaeresis cracks within the troughs of sinuous current ripples. **C.** Sole markings on the base of a hematite-stained sandstone bed. **D.** Finely laminated shales with carbonate nodules, lower Little Dal Group. **E.** Contact between the uppermost Abraham Plains and the Little Dal Group (demarcated by the yellow line), featuring significant erosional surfaces (white dashed lines) and swaley cross stratification (white arrow). This succession is interpreted to record ravinement and the deposition of estuary-mouth and shoreface sediments during transgression from coastal to basinal sedimentation. Coins in A, C are 21.2 mm wide, hammer in B is 33 cm, lens cap in D is 5.8 cm.

Interpretation

The facies described above were influenced by both fluvial sediment supply and marine processes, and it is likely that the relative importance of these two sedimentary environments varies between localities

of the Abraham Plains Formation. In other localities, the sandstones of the Abraham Plains Formation have been suggested to be the product of lateral migration of ephemeral–perennial, sandy-braided rivers, for which lateral accretion cosets are traceable over hundreds of metres (Long, 2011a). Channel elements have been documented in the Mackenzie Mountains, though crevasse and splay elements are not well developed (Long, 2011a). Despite the lenticular nature of some of the sand bodies in the study area, significant channelisation was not observed. However, prior to the evolution of land plants, Precambrian river systems are considered to have been predominantly braided and represented by stacked sandstone sequences with sheet-like geometry (Schumm, 1968; Cotter, 1977; Eriksson et al., 1998). Therefore, stacks of extensive tabular sandstones bounded by planar erosion surfaces in Proterozoic successions are often interpreted to represent deposition in a sandy braided river system (Long, 1977; Siedlecka and Edwards, 1980; Bose and Chakraborty, 1994; Gibson et al., 2021), and the Katherine Group sandstones have been linked to a widespread system of braided rivers envisaged to have drained mountains formed during the Grenvillian orogeny during the Tonian Period (Rainbird et al., 1997). Within this context, we suggest that the Abraham Plains Formation in the study area experienced a significant marine influence on deposition, as outlined below.

For the tabular cross-stratified sandstone facies, the geometry of the characteristic large bedforms implicates the migration of straight-crested, simple subaqueous dunes following the dominant current direction (Dalrymple et al., 1978; Reineck and Singh, 2012), likely characterised by a unidirectional equilibrium current with a steady, separated flow regime (Allen, 1980). This scenario results in relatively steep dune bedforms acutely overlying laterally extensive, first-order erosional surfaces; when flow is less steady, smaller convex-up, second-order erosional surfaces form (Allen, 1980), which are not observed. Dunes in fluvial environments form perpendicular to the flow direction as longitudinal bars and sheetflood deposits of ephemeral streams (Williams, 1971; Allen, 1980), or at high angles to the current direction as point bars in meandering or braided stream settings (Wright, 1959). Fluvial dunes often have complex interbedding of trough cross-stratified sandstones and conglomerates (Ielpi and Rainbird, 2016), as well as the truncation of underlying sets (Williams, 1971; Allen, 1980); these features were not observed in the study area.

Alternatively, dunes can form in the upper shoreface via wave, longshore and rip currents (Clifton, 2006). Shoreface dunes are often trough cross-laminated and feature gravel-lined scours due to surf processes and storms (Dashtgard et al., 2009). Gravel-bearing horizons were documented near the base of the Abraham Plains Formation (Fig. 9E), associated with local scours and incorporating granules and small quartz arenite pebbles. However, these features are not common in the study area. Dunes can also form as elongate sand bars perpendicular to dominant tidal currents in coastal embayments (Allen, 1980; Dalrymple and Rhodes, 1995; Barnard et al., 2006; Dalrymple et al., 2012). Tidal bars have a lateral accretion architecture, whereas compound tidal dunes have a forward-accretion architecture indicated by cross beds that form simple superimposed dunes with a dip direction that is the same as the inclined master bedding planes within the compound dunes (Olariu et al., 2012). Dunes in tide-dominated embayments feature tidal bundles, reactivation surfaces and can form compound dunes (Dalrymple et al., 2012). Given the stratigraphic association with the shallow marine facies of the McClure Formation, the observation of reactivation surfaces (albeit rare; Fig. 9B–C), and the lack of truncation of underlying sets, we suggest that the quartz arenites of the Abraham Plains Formation in the study area were largely deposited as tidal bars. The physical separation of sands from finer-grained material may have resulted from contemporaneous nearshore mud traps in lagoonal, tidal flat or lower coastal plain settings, which are suggested to have been efficient mud traps in Precambrian coastal environments (e.g., O'Connell et al. 2022), as also seen in the McClure Formation. However, it is likely that the sandstone facies of the Abraham Plains Formation were deposited in a range of coastal environments that varied spatially and temporally. While further study of these facies in the Wernecke Mountains is necessary to better constrain the relative influence of tide, wave and river processes on dune formation, we suggest that these facies can be interpreted to have been deposited as marine sands rather than in a continental, fluvial setting.

The fine-grained siliciclastic facies of the upper Abraham Plains Formation, as with the McClure Formation, is interpreted to have been deposited as tidal flats in a protected, coastal embayment. The polygonal cracks (Fig. 9D) are interpreted as desiccation cracks indicating periodic subaerial exposure, whereas the curlicue cracks within ripple troughs (similar to the pseudofossil 'Manchuriophycus'; Fig. 10B) are interpreted as synaeresis cracks formed due to the subaqueous shrinkage of cohesive sediment (McMahon et al., 2017), possibly enhanced by the presence of microbial mats (Gehling, 1999).

The swaley cross stratified sandstone facies observed in the uppermost Abraham Plains Formation indicates combined oscillatory and unidirectional flow conditions on the shallow shelf during storms (Swift et al., 1983; Dumas and Arnott, 2006), and suggests that the transgression that led to the

deposition of the basinal shales of the Little Dal Group was underway. The erosional surfaces in the uppermost Abraham Plains Formation are therefore interpreted as ravinement surfaces (dashed white lines in Fig. 10D). Tentatively, the lower surface is interpreted to represent a ravinement surface formed by tidal scour and infilled by estuary-mouth sands, with the upper surface representing a subsequent wave-ravinement surface due to shoreline retreat during transgression (Allen and Posamentier, 1993). The fine lamination and lack of wave-influenced sedimentary structures of the shales of the overlying Little Dal Group indicate deposition in deep water (i.e., below wave base). The comparatively high organic carbon content of these shales, and the associated siderite nodules, suggests a transition to a relatively deep setting characterised by dissimilatory iron reduction leading to the formation of authigenic, Fe-rich carbonates. The mixed siliciclastic–carbonate succession that overlies these black shales is correlated with the Basinal assemblage of the Little Dal Group in the Mackenzie Mountains and interpreted to represent suspension settling and carbonate mud sedimentation below wave base (Turner, 2011b).

4.3 Stratigraphic context of the Katherine ironstone

The ironstones of the Katherine Group are interbedded with the fine-grained siliciclastic facies of the McClure Formation as well as the tabular cross-stratified sandstone facies of the Abraham Plains Formation, suggesting that they were deposited in coastal environments ranging from intertidal mudflats to a tide-influenced estuary. Given that a comprehensive sequence stratigraphic analysis is beyond the scope of this study, it remains unclear whether this stratigraphic position is controlled by basin-scale relative sea-level fluctuations, which are hypothesised to have controlled the sedimentation of the Katherine Group more broadly (Long et al., 2008).

The Katherine Group overlies the Hematite Creek Group which records a gradual transition from basinal shales to peritidal carbonates and siliciclastics (Turner, 2011b), and therefore the Katherine Group was deposited following a long-term, first-order regression (Gibson et al., 2019). The broad facies alternation between fine-grained siliciclastic-dominated and sandstone-dominated successions (i.e., K1–K7) in the Katherine Group formations has is considered to be the product of a series of higher-order transgressive-regressive cycles (Long et al., 2008; Turner and Long, 2008). In particular, the subtidal carbonates of the lower McClure Formation in the Mackenzie Mountains have previously been interpreted to reflect a regional, third-order transgression based upon correlations with the Shaler Supergroup in the Amundsen Basin (Jefferson and Young, 1988; Rainbird et al., 1996).

In the study area, the McClure Formation records a clear regression from the subtidal, carbonate-bearing facies to the peritidal, fine-grained siliciclastic facies, as described above. The subsequent transition to the subaqueous sand dune-dominated setting of the Abraham Plains Formation may be the product of temporal, autogenic variability within laterally equivalent coastal depositional environments (possibly driven by the migration of dunes or the associated inland fluvial systems). Alternatively, this transition may have been driven by changes in climate (affecting sediment supply), or continued regression from a bayhead tidal mudflat to an upstream, tide-influenced estuary. Subsequently, the swaley cross-stratified facies and ravinement surfaces of the uppermost Abraham Plains Formation record transgression and shoreline retreat, followed by deposition of the basinal shales of the lowermost Little Dal Group which are interpreted as a flooding surface (Turner, 2011b).

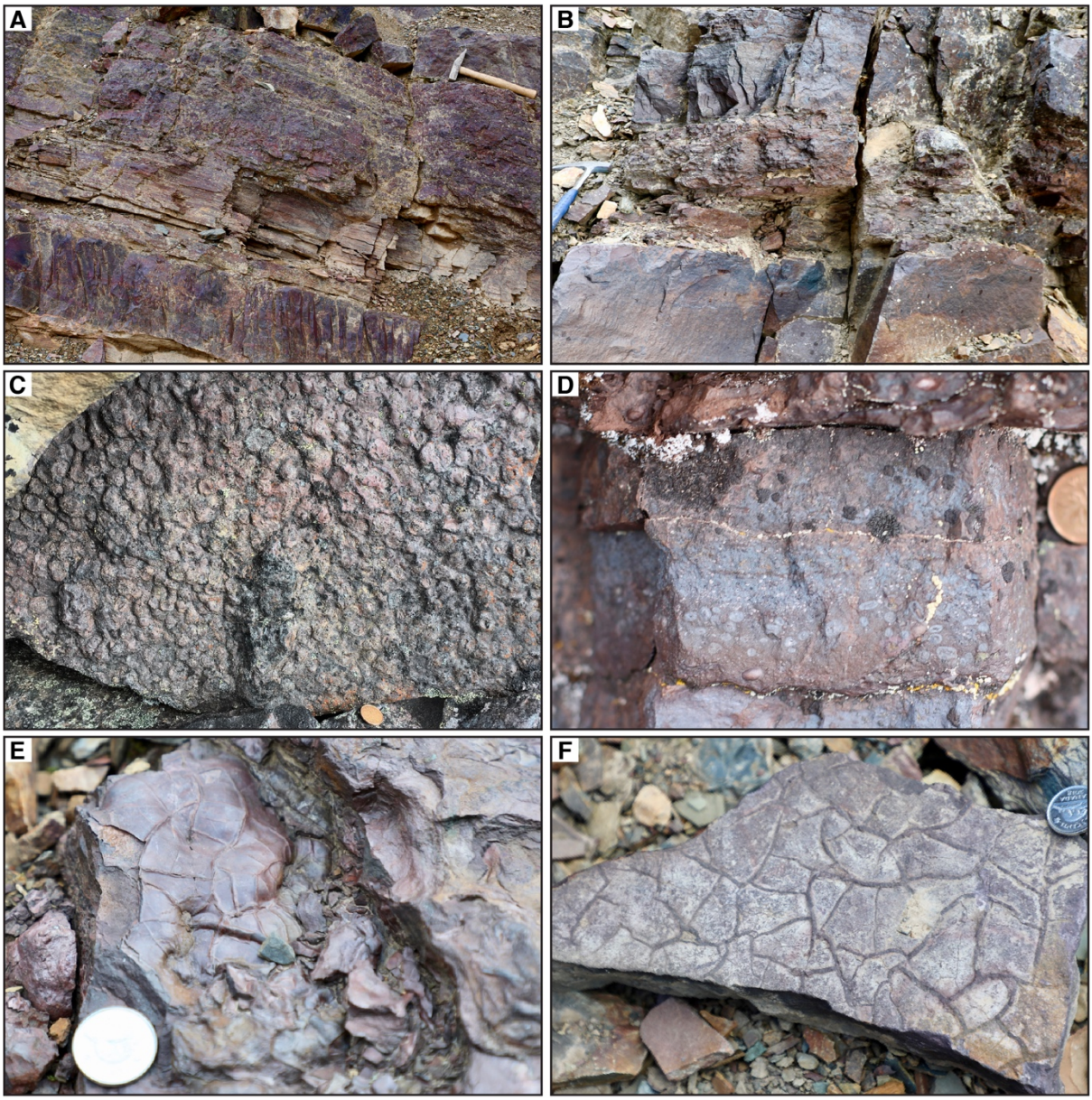

Fig. 11. Outcrop photos of the Katherine ironstone. **A.** Interbedded oncoid-bearing ironstone beds (oncolites; see text for discussion on terminology) and ferruginous mudstones. **B.** Oncolite bed hosted by ferruginous sandstones. **C.** A plan view of a bed of large (<5 cm), oblate hematite–berthierine oncoids, with the elongated plane of the oncoids crudely aligned with the bedding plane; see Fig. 13 for petrography. These oncolites are comparable to the reniform ironstone described from the late Palaeoproterozoic Chuanlinggou Formation (Li and Zhu, 2012; Zhu et al., 2022). **D.** Bed of small (<5 mm), subspherical to oblate hematite–berthierine ooids and pisoids. **E.** Cuspate structures on the surface of an ironstone bed; these are further detailed in Fig. 13. **F.** Casts of polygonal cracks preserved on the base of the bedding plane of a ferruginous sandstone horizon. Hammers in A–B are 33 cm longm coins are 19 mm wide in C–D and 21.2 mm wide in E–F.

4.4 Ironstone and ferruginous facies

Field and petrographic observations

The McClure–Abraham Plains formations contain several ferruginous lithologies: coated grain-bearing units dominantly composed of berthierine and hematite (referred to herein as ironstone), hematite-cemented sandstone (ferruginous sandstone) and ferruginous siltstone and mudstone. These ferruginous facies are interbedded with the fine-grained siliciclastic facies (i.e., tidal mudflat deposits) of the McClure Formation and the cross-stratified sandstone facies of the Abraham Plains Formation. Beds of the ferruginous facies can be traced on the outcrop scale for hundreds of metres (e.g., Fig. 6), however, similar facies have not been found in other areas which suggests that these deposits are laterally discontinuous. The contacts of the ironstone beds with the host lithologies are generally sharp.

The ferruginous sandstones are lithologically similar to the quartz arenites of the cross-stratified sandstone facies (with a greater abundance of hematite cement), and contacts can be gradational with these facies.

The ironstone coated grains exhibit a high degree of morphological variability. Historically, the coated grains of ironstones have been referred to using the conventional terminology applied to their carbonate analogues (e.g., Pettijohn, 1975; Peryt, 1983), and termed iron ooids (<2 mm in diameter), iron pisoids (>2 mm in diameter), iron oncoids (featuring irregular laminations that may represent a microbial influence on deposition) or spastoliths (deformed ooids) (Kimberley, 1983; Reolid et al., 2008; Dreesen et al., 2016). More recently, alternative terminology has been proposed to avoid possible genetic connotations implied by the carbonate terminology, and have been referred to as granules (<1 cm) and concretions (>1 cm) (Dodd et al., 2018) or iron coated grains (Matheson and Pufahl, 2021). However, we find that the use of the conventional carbonate terminology in a non-genetic sense is useful for describing the morphology of the coated grains of the upper Katherine Group.

Rare, sub-spherical iron ooids are present with a diameter of ~100 μm, often lacking any obvious nucleus, and associated with fenestrae (Fig. 13F). Larger, sub-spherical coated grains with rounded quartz grain nuclei reach ~1 cm (i.e., iron pisoids or "giant ooids" sensu Sumner and Grotzinger, 1993). The largest coated grains, which can reach ~4 cm in length, ~2 cm in width and ~1.5 cm in height, are characterised by irregular morphology—these are referred to herein as iron oncoids in a non-genetic sense. These iron oncoids are often nucleated around a fragment of a pre-existing iron coated grain (i.e., a composite oncoid; Fig. 13), and the iron coatings inherit the irregular morphology of the nucleus. Often, the nucleus is offset from the middle of the iron oncoids. The abundance of coated grains in the ironstone horizons is also variable, ranging from a few millimetre-scale iron ooids suspended within a ferruginous matrix (Fig. 11D), to beds composed almost entirely of large iron oncoids (iron oncolite; Fig. 11B–C). These iron oncolite beds vary from 1–50 cm in thickness, and the iron oncoids are typically oblate ellipsoids oriented with their shortest axis oriented perpendicular to bedding. Following the classification scheme of Dunham (1962) as applied to ironstones (sensu Young, 1989), the coated grain-bearing lithologies of the upper Katherine Group include oncoidal/pisoidal/ooidal wacke-ironstone and pack-ironstone, as well as oncoidal grain-ironstone. The ironstones beds have sharp lower and upper contacts and are typically in contact with siltstones or sandstones.

The ironstones are composed of a dominant authigenic component and minor (<5 %) detrital component. Petrographic and XRD analyses indicate that the Fe mineralogy is dominated by hematite (Fe_2O_3) and berthierine [$(Fe^{2+},Al)_3(Si,Al)_2O_5(OH)_4$] (Fig. 13), which is a trioctahedral member of the kaolinite–serpentine series (Bailey, 1988) that has a planar structure and a basal spacing of 0.7 nm along [001] (Brigatti et al., 2013). Electron microprobe and X-ray spectroscopy analyses indicate that two types of berthierine are present: a K–Fe-rich variety and a Mg–Fe-rich variety, with the K likely hosted by disordered, chlorite-like layers intercalated with the berthierine. The ironstone matrix is typically a mixture of hematite and K-berthierine, with coarse overprinting by Mg-berthierine locally present. Other phyllosilicates (e.g., mica, pyrophyllite and smectite) are also present. Hematite occurs as microcrystalline cortical laminae ~10–100 μm thick, interlaminated with ~50–500 μm thick laminae of K-rich berthierine, both of which appear to be primary phases. This K-berthierine often features pervasive, disseminated laths of microplaty hematite (10–80 μm in length) and is locally overprinted by patchy, radial aggregates of Mg–Fe-rich berthierine. Hematite and K-berthierine are also found as a mixed matrix in many ironstone horizons, and hematite also constitutes a common grain-rimming cement, whereas Mg-berthierine is found as a pore-filling cement. This coarsely crystalline Mg-berthierine can be seen overprinting finer (depositional) textures in both K-berthierine and hematite. In some samples, hematite can overprint the Fe phyllosilicates due to later oxidation, forming specular hematite. Other, minor authigenic phases include apatite (francolite), monazite, barite, siderite and pyrite. Disseminated microcrystalline phosphate is present within the cortices of large oncoids and pisoids (Fig. 15).

Detrital grains in the ironstone beds are predominantly quartz sand that is fine to very coarse (~0.1–1 mm). Quartz grains are most commonly coarse sand sized and rounded (i.e., more rounded than the associated quartz arenites of the Abraham Plains Formation; cf. Figs. 9G, 13G), with surface etching and are often matrix supported. Detrital clays are also present as fine–medium silt-sized grains of Fe-poor clays; these are mostly associated with iron ooid-bearing ironstones, and largely absent from iron oncolites. The reverse is generally true for quartz sand grains, which are more commonly found in iron oncolites, including within the laminae of iron oncoids and pisoids. Heavy minerals, such as zircon, rutile and ilmenite are minor components within the cortices of coated grains, yet near-absent in the host rock (Fig. 14C).

Some of the large iron oncoids contain radial shrinkage cracks that crosscut the oncoid centre (Fig. 13E); these cracks are typically <0.5 mm in diameter and can reach 8 mm in length. The cracks are filled with authigenic cement, predominantly an Fe-poor aluminosilicate with a chemical composition similar to kaolinite. This Fe-poor phyllosilicate has been partially overprinted by a Mg- and Fe-rich serpentine (Mg-berthierine), and the cracks are often rimmed at the edges by hematite cement (Fig. 13). Other micron-scale fractures are often observed near the outer edges of the iron oncoid cortices, associated with a deflection in the successive cortical laminae that give the cortices a cuspate appearance that are preserved on the oncoid surface (Fig. 13A).

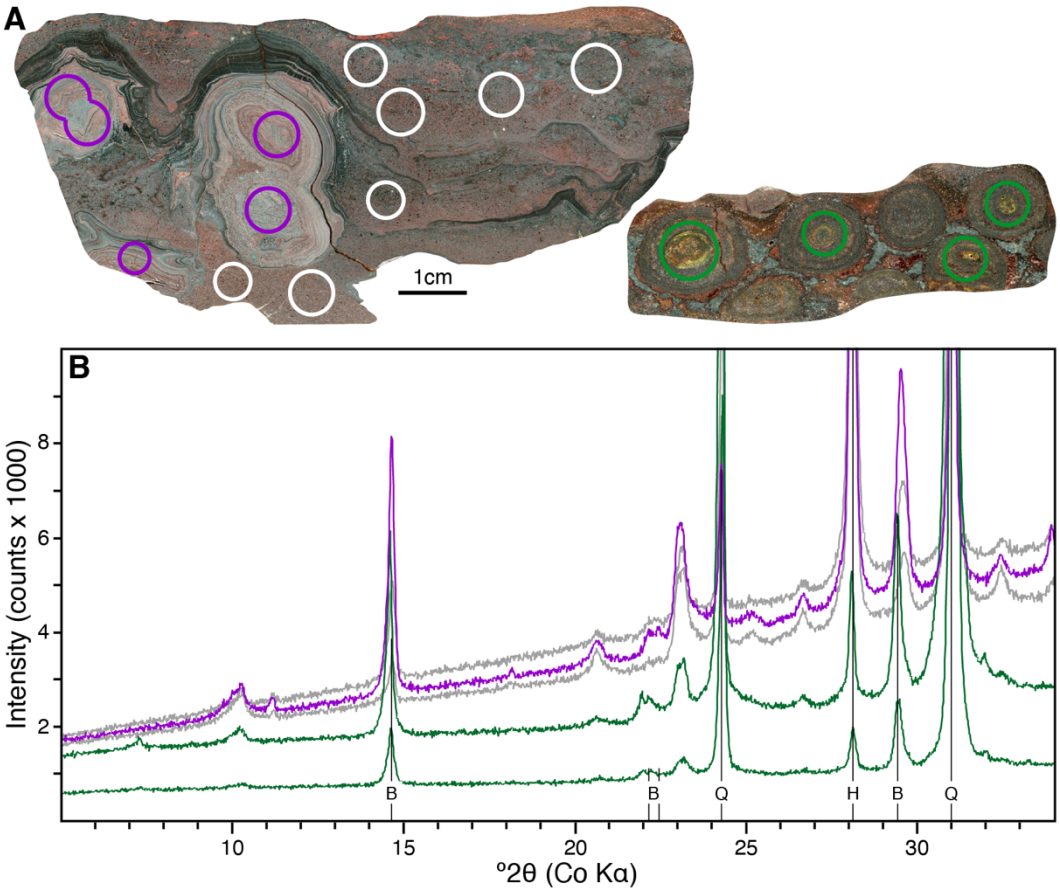

Fig. 12. X-ray diffraction data used to interpret the mineralogy of the Fe-rich phyllosilicate that forms a dominant component of the Katherine ironstone (purple = core of large iron oncoids; green = core of iron pisoids; white = ironstone host rock matrix). **A.** Location of targeted phases for sample powder drilling; the colour of each circle corresponds to an XRD spectrum. **B.** XRD spectra for the ironstone showing peaks characteristic of berthierine, including a prominent peak at 14.7º and a minor double peak at 22.1º and 22.3º (2θ angle). Note that for the oncoids, the XRD spectra are most similar to monoclinic berthierine, whereas the pisoids are suggestive of hexagonal berthierine. Also shown are the characteristic peaks for berthierine (B), quartz (Q) and hematite (H).

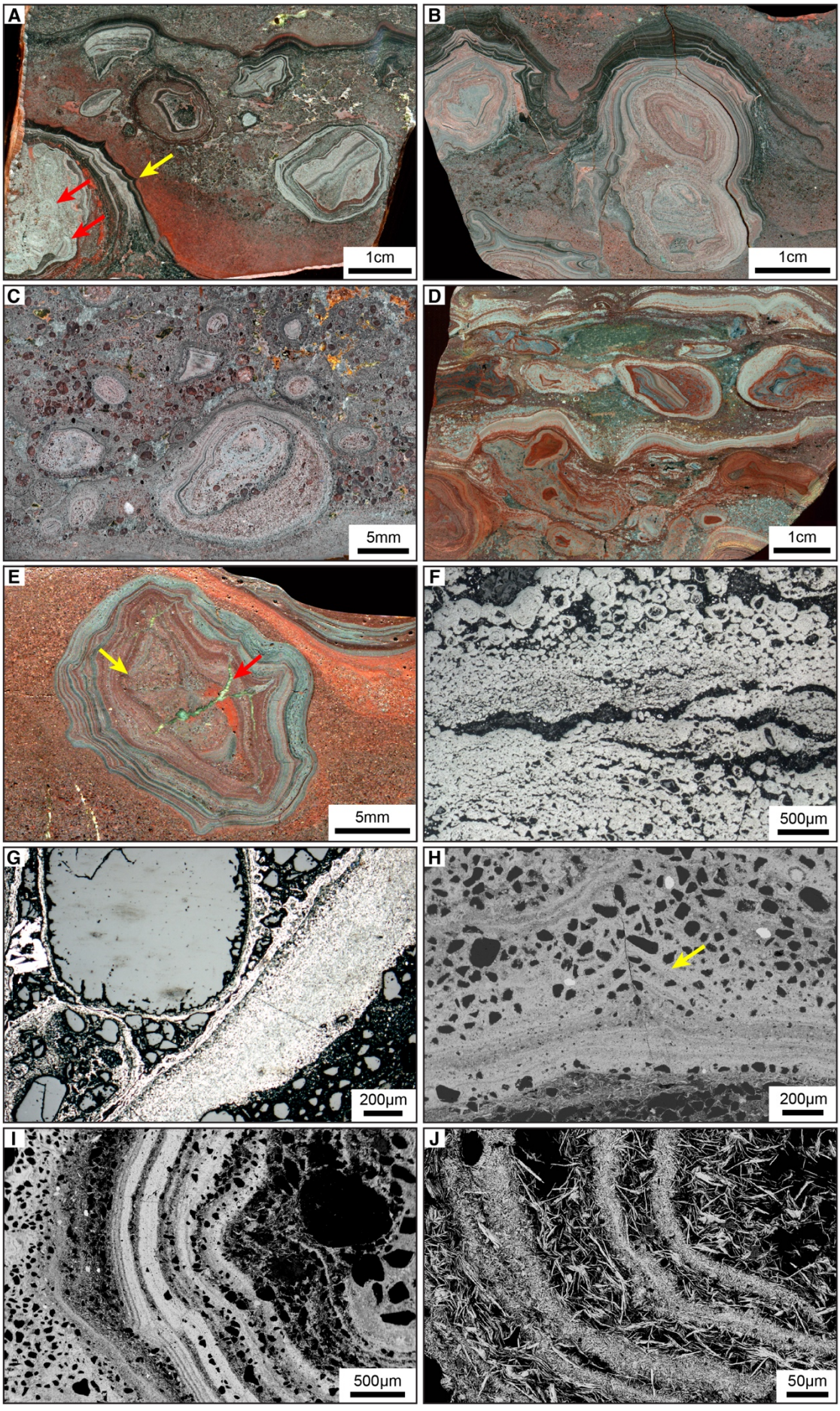

1

Fig. 13. Petrography of the oncolitic facies of the Katherine ironstone. **A.** Large oncoids with composite cores made up of oncoid fragments (red arrows), which have been oxidised to hematite. The outer surface of the oncoid is composed of interlaminated hematite and berthierine, with convex-outwards cuspate structures that have microfractures along their axial planes (yellow arrow) which may represent fluid-escape structures. Note the overprinting of precursor hematitic laminae by coarsely crystalline Mg-berthierine. The prominent layer of berthierine–hematite laminae near the top of the panel is interpreted to represent a hardground surface, with the small domal structures possibly of biological origin. **B.** Composite, mixed berthierine–hematite oncoids within a fenestral matrix. **C.** Large hematite–berthierine pisoids with irregular core shapes and large, rounded quartz grains entrained within the cortical laminae. **D.** Composite oncoids and hardground crusts within oncolitic ironstone, including mound textures reminiscent of biogenic mounds. **E.** Hematite–berthierine oncoid crosscut by radial, clay-cemented cracks (red arrow) through the composite core (yellow arrow). **F.** Reflected light photomicrograph showing reverse-grading in hematite ooids, featuring fenestrae. **G.** Reflected light photomicrograph showing diagenetic, grain-coating hematite cements surrounding matrix quartz grains that are texturally distinct from the oncoid cements. Quartz grain rims show heavy etching and dissolution. **H.** Backscattered electron image of a cusp on the surface of a hematite–berthierine oncoid showing deflection of detrital quartz grains (dark grey; yellow arrow), indicating that the cusp formation is postdepositional. **I.** Backscattered electron image of a cross section of an iron oncoid, showing the fine interlamination of hematite (light grey) and berthierine (darker grey); horizons of quartz grains (black) tracing the cortical laminae indicates that these laminae are sedimentary (i.e., syndepositional) features rather than intrasedimentary concretions. **J.** Backscattered electron image showing the fine-grained hematite layers interlaminated with layers of berthierine, crosscut by coarser microplaty hematite.

Interpretation

The paragenesis of ironstones is the subject of contention, as berthierine can form via the diagenesis of Fe oxyhydroxides and kaolinite (Bhattacharyya, 1983), and iron oxides (goethite / hematite) can result from the oxidation of iron silicates (berthierine / chamosite) (Gygi, 1981; Taylor and Curtis, 1995). This oxidation of ferrous phases to ferric (oxyhydr)oxides can be seen in ironstones recently exposed to oxidative weathering by mining excavation (Grgic et al., 2013). In Recent sediments, the formation of coated grains has been documented for both Fe (oxyhydr)oxides (Heikoop et al., 1996; Di Bella et al., 2019) and Fe phyllosilicates (Rohrlich et al., 1969; Kimberley, 1994). However, these thin, simple grain coatings grains are distinct from the micron-scale concentric laminations of the iron ooids of ironstones, and because the sedimentary facies associations of these proposed modern analogue sites do not clearly match those of ancient ironstones, the applicability of these sites as modern analogues is unclear. Because of this ambiguity, the primary mineralogy of Phanerozoic ironstones has been variably suggested to be Fe oxides (goethite / hematite) (Bhattacharyya, 1983; Maynard, 1986) or Fe silicates (berthierine / chamosite) (Taylor, 1949; Hallam, 1963; Knox, 1970). We suggest that the fine interlamination of hematite and berthierine in the Katherine iron coated grains (including reworked iron oncoid fragments; Fig. 13) indicates that both minerals represent primary / early diagenetic phases that formed prior to final burial and lithification. Accordingly, the ironstones likely experienced fluctuating redox conditions during deposition and early diagenesis. The occurrence of microcrystalline phosphates (francolite, monazite, rhabdophane) forming distinct concentric bands within cortical laminae (Fig. 15) also argues for a syndepositional origin for these phosphates.

The formation mechanisms of iron coated grains are also debated. Much of the contention stems from the difficulty of reconciling evidence for synsedimentary iron mineral precipitation in seemingly oxygenated shallow marine sites of ironstone deposition (many Phanerozoic ironstones contain fossils of aerobic animals; Odin, 1988; Burkhalter, 1995; Matheson and Pufahl, 2021), given the low solubility of iron under oxidising, circumneutral conditions (Baumgartner and Faivre, 2015). To address this apparent “ironstone paradox” (Hallimond, 1925), diagenetic growth of coated grains within the sediment pile (i.e., concretion) has been proposed (e.g., Pulfrey, 1933; Carozzi, 1961; Hemingway, 1974; Chauvel and Guerrak, 1989; Pufahl and Grimm, 2003; Dodd et al., 2018; Matheson and Pufahl, 2021). The precipitation of berthierine cement is considered to take place within the suboxic diagenetic zone (Taylor, 1998). Models for a concretionary origin of iron ooids often invoke repeated intrasedimentary precipitation, exposure and burial cycles in order to account for the interlamination of different mineral phases in the ooid cortices (Hallimond et al., 1951; Odin et al., 1988; Garcia-Frank et al., 2012). Alternatively, ironstone coated grains have been interpreted to form in the water column or seafloor (e.g., Hallimond, 1925; Adeleye, 1973; Van Houten and Purucker, 1984; Cotter and Link, 1993), and adsorption, accretion and primary precipitation mechanisms have been proposed (e.g., Bhattacharyya and Kakimoto, 1982; Gehring, 1985; Harder, 1989; Kearsley, 1989).

Several lines of evidence argue against an entirely intrasedimentary origin for the iron coated grains of the Katherine Group. The observation of iron crusts forming hardgrounds (Fig. 13A) suggests the precipitation of Fe minerals from seawater rather than diagenetic fluids. In the ironstone horizons, coated grains preserve fine detail in the tangential cortical laminae (Fig. 13). By contrast, concentric

laminations in concretions and weathered grains in soil profiles (such as bauxites and laterites; Nahon et al., 1980) have radial textures (Adeleye, 1973; Bhattacharyya and Kakimoto, 1982; Van Houten and Purucker, 1984), and lack ferrous phyllosilicates (van Houten, 1992). The quartz grains within the laminae of iron pisoids and oncoids suggests that these grains were coated on the seafloor during their formation. In places, quartz grains entrained within oncoid laminae are rotated parallel to the angle of surface cusps (Fig. 13H), indicating that the iron oncoids were forming prior to early diagenesis. Importantly, differences in quartz grain size between the coated grains and the host matrix (Figs. 12, 13) indicate that these coated grains cannot have formed as concretions. Similar evidence for extrasedimentary formation of coated grains is documented in Phanerozoic ironstones (Taylor, 1990), some of which have encrusting marine foraminifera within the cortical laminae (Burkhalter, 1995; Collin et al., 2005; Garcia-Frank et al., 2012; Vodrážková et al., 2022). It is likely that some components of the ironstones may have developed during further intrasedimentary precipitation (such as oncoid rim cements), and there is petrographic evidence for further mineral transformation (hematite overprinting berthierine and vice versa) during diagenesis (Fig. 13). However, these observations require that the ironstone coated grains were exposed to the water column for at least some part of their formation.

Complex, crinkled textures similar to those of the Katherine iron oncoids have been documented in Phanerozoic iron oncoids, and used to argue that their genesis was biologically mediated (Dahanayake and Krumbein, 1986). Textures considered to be diagnostic of Fe oxidising bacteria such as mineralised sheaths and stalks (Little et al., 2004; Emerson et al., 2010) were not observed in this study. However, the accretion of detrital quartz grains onto iron coated grain cortices indicates that the surface was adhesive, which could have been due to the presence of organic films. A greater abundance of zircon and other heavy minerals in the iron oncoids cortices compared to the host matrix—a characteristic that has also been documented in similar iron silicate-coated grains in the Mesoproterozoic (Johnson, 2021)—also shows that these surfaces were adhesive. Alternatively, the observation that detrital grains are more abundant in berthierine may suggest that these grains were concentrated by sticking to an Fe-Al-Si precursor gel. Regardless of any potential biological influence, the irregular morphology of the iron oncoids argues against formation by accretion and abrasion. While some of the iron coated grains are sometimes relatively spherical (e.g., Fig. 14A), most of the iron oncoids are oblate ellipsoids or other irregular shapes oriented with their long axis parallel to bedding. This geometry is likely related to minor synsedimentary compaction during deposition on the seafloor, indicating plastic deformation during early diagenesis and burial (as documented in Phanerozoic ironstones; e.g., James Jr and Van Houten, 1979).

Fragmented iron oncoids within composite coated grains provide evidence for synsedimentary brittle deformation (Fig. 13). Similar fragmented iron ooids in Phanerozoic ironstones are considered to be the product of physical reworking under high energy conditions (Taylor, 1949; Hallam, 1967). However, internal cracks are common within the iron oncoids (Fig. 13) (as is also the case for Phanerozoic ironstones; Van Houten and Purucker, 1984), and this promoted fragmentation during reworking. Cracks within the iron oncoids may suggest dewatering of a precursor Fe-Si gel or other hydrated phase, a process which has been suggested to explain cracks within iron coated grains in the Phanerozoic (Schoen, 1964) and in Precambrian granular iron formations (Quirke, 1961; Dimroth and Chauvel, 1973; Hall and Goode, 1978). Fenestrae are also abundant in the Katherine ironstone (Fig. 13A, F), and have also been documented in Precambrian granular iron formations (Simonson, 1987). By analogy to carbonate sedimentary systems (e.g., Logan, 1974), these fenestrae are interpreted to indicate wetting and drying during diagenesis. Importantly, the coated grains do not appear to have been significantly transported, as they are commonly matrix-supported, and the composite oncoids with fragmented nuclei require that the iron coated grains were physically reworked during formation at the site of deposition.

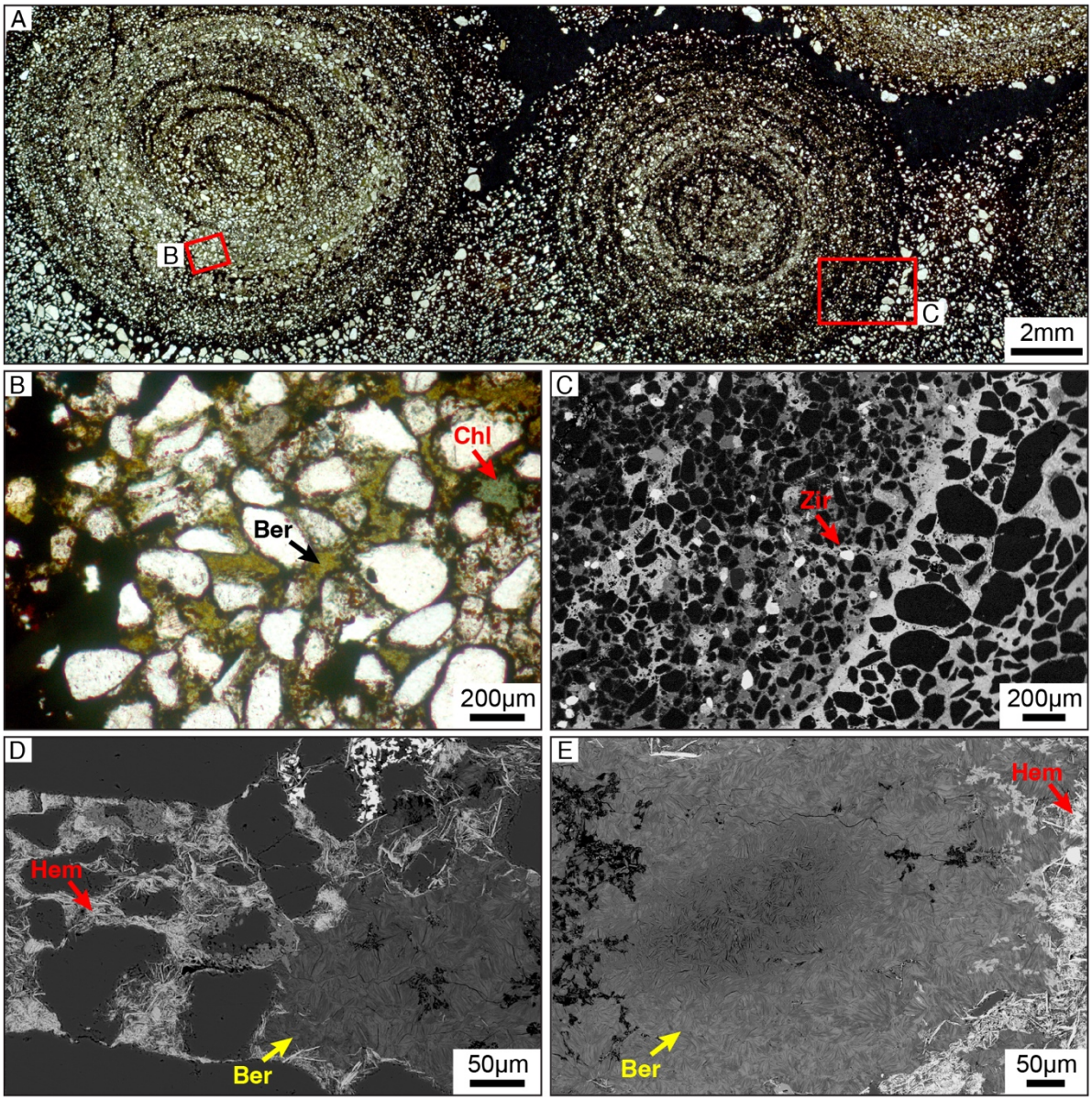

Fig. 14. Petrography of the ironstone ooids / pisoids. **A.** Transmitted light photomicrograph of subspherical berthierine pisoids (giant ooids?) within a sandy ironstone. **B.** Transmitted light photomicrograph of berthierine in the interstices of subrounded to subangular quartz grains, showing berthierine matrix (black arrow) and chlorite cement (red arrow). **C.** Backscattered electron image highlighting the grain size contrast between the sandy berthierine pisoid and the host hematitic sandstone, indicating that the pisoid was deposited as a clast (rather than forming as a concretion). Heavy minerals (such as zircon; red arrow) are preferentially incorporated into the pisoid rather than the host rock matrix. **D.** Backscattered electron image showing disseminated hematite throughout the berthierine matrix of the pisoid cortex (red arrow), overprinted by a coarser Fe-, Mg-rich phyllosilicate (yellow arrow). **E.** Backscattered electron image of a relatively pure zone of berthierine near the core of a berthierine-rich pisoid.

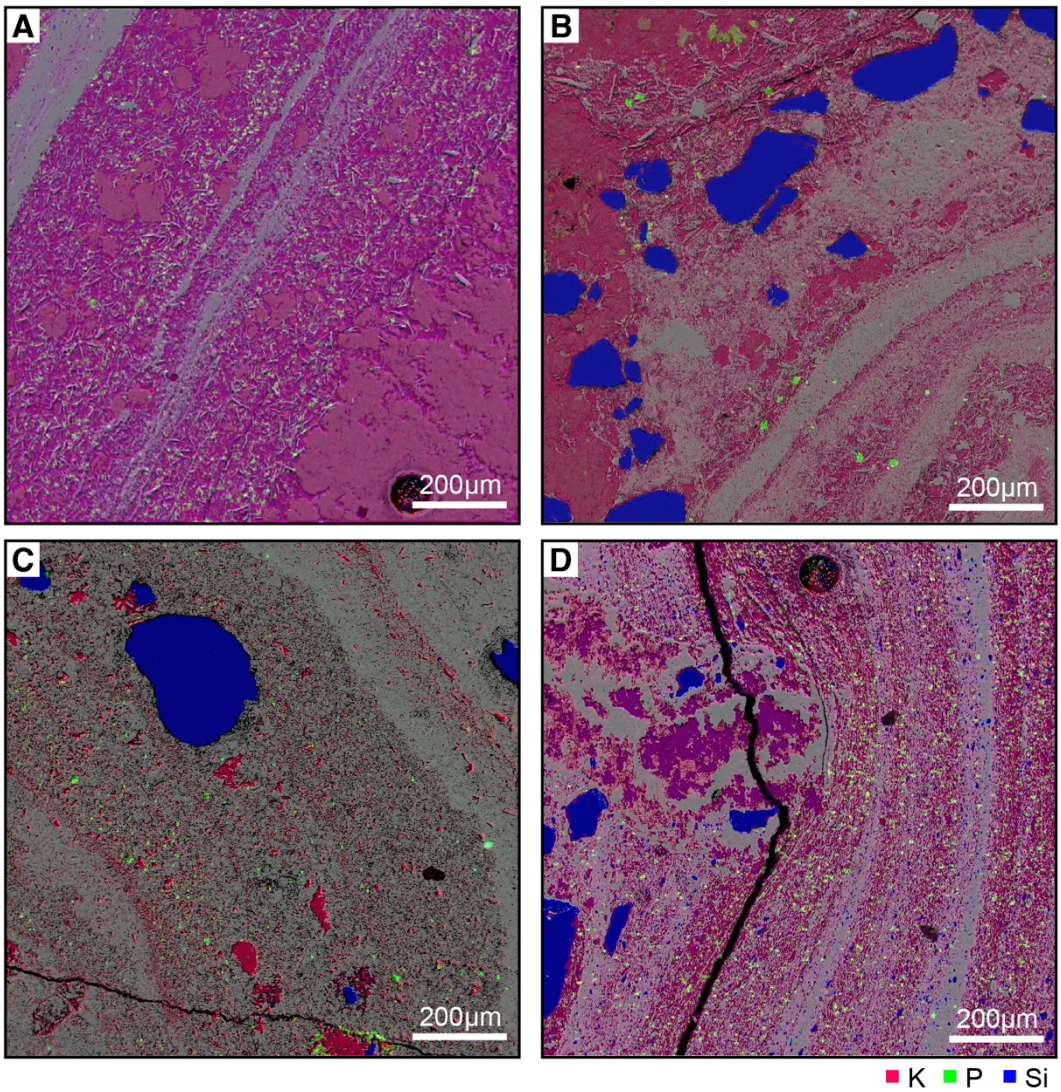

Fig. 15. Electron microprobe elemental map showing the distribution of microcrystalline phosphates (bright green) disseminated throughout the berthierine cortical laminae (pink) of these ironstone oncoids.

5. Ironstone geochemical data

5.1 Bulk rock major elements

In order to discuss relative geochemical enrichment, geochemical data were normalised to weathered young upper continental crust using values from Queensland mud (MuQ; Kamber et al., 2005). Compared to MuQ, the ironstones are depleted in all major elements due to the strong enrichment in Fe. In particular, Ca and Mn are strongly depleted. The ferruginous sandstones are enriched in Ba, whereas all other lithologies have similar Ba contents to MuQ. All lithologies are depleted in Na, Mg, P, Ca and Mn. Organic matter contents of the ironstones (mean TOC = 0.039 wt%; n = 6) are an order of magnitude lower than those in the mudstones of the McClure Formation (mean 0.37 wt%; n = 7) and basal Little Dal Group (mean 0.29 wt%; n = 4).

Interelemental Pearson correlation matrices (Lee Rodgers and Nicewander, 1988) calculated using the bulk rock (XRF) data for ironstone samples generally show positive correlation between Na, Mg, Al, K and Ti, whereas Fe does not show a strong positive correlation with any other major element (Table 2). For these ironstones, Si also correlates negatively with several major elements, particularly K and Fe, whereas P shows a strong positive correlation with Ca, and a less pronounced positive correlation with Na and Ti (Table 2).

The Chemical Index of Alteration (CIA) uses the relative proportions of various major elements in sedimentary rocks as a proxy for the degree of chemical weathering (Nesbitt and Young, 1982), and calculated as:

$$CIA = [Al_2O_3 / (Al_2O_3 + CaO' + Na_2O + K_2O)] \times 100 \quad (3)$$

where all oxides are in molar units, and CaO′ represents an approximation of the CaO present in silicate minerals, corrected for Ca in phosphates and carbonates according to the following formula:

$$CaO' = CaO - 10/3 \times P_2O_5 \quad (4)$$

This value is used unless CaO′ exceeds Na_2O, in which case the value for Na_2O is used in place of CaO′ (McLennan, 1993; Wang et al., 2020). This likely represents a minimum estimate for CIA given that Ca is more mobile than Na during weathering (McLennan, 1993), however, the CaO values are so low for nearly all samples that this correction does not significantly change the CIA values. The CIA values of the Katherine Group are high for all lithologies analysed, including mudstones (77–91; mean 86; n = 5), ferruginous mudstones (87–91; mean 89; n = 3), siltstones (77–98; mean 87; n = 12), and ferruginous siltstones (81–95; mean 86; n = 10). The CIA values are generally more elevated in the ironstone-bearing upper McClure Formation than in the lower part (see Fig. 18A). The McClure Formation shales have higher CIA values than those of the lowermost Little Dal Group (77–78; mean 77; n = 4).

	Na_2O	MgO	Al_2O_3	SiO_2	P_2O_5	K_2O	CaO	MnO	Fe_2O_3	BaO	TiO_2
Na_2O	1	**0.61**	**0.88**	-0.42	**0.57**	**0.74**	**0.55**	0.05	0.18	-0.00	**0.58**
MgO	**0.61**	1	**0.61**	-0.059	0.33	0.26	0.42	-0.00	-0.13	0.25	0.31
Al_2O_3	**0.88**	**0.61**	1	-0.40	**0.50**	**0.90**	0.45	0.18	0.11	0.12	**0.69**
SiO_2	-0.42	-0.06	-0.40	1	-0.31	**-0.52**	-0.21	-0.29	**-0.95**	-0.06	-0.45
P_2O_5	**0.57**	0.33	**0.50**	-0.31	1	0.41	**0.95**	0.24	0.14	0.48	**0.68**
K_2O	**0.74**	0.26	**0.90**	**-0.52**	0.42	1	0.34	0.20	0.29	0.14	**0.70**
CaO	**0.55**	0.42	0.45	-0.21	**0.95**	0.33	1	-0.01	0.05	0.42	**0.62**
MnO	0.05	-0.00	0.18	-0.30	0.24	0.21	-0.01	1	0.21	0.30	0.19
Fe_2O_3	0.18	-0.13	0.12	**-0.95**	0.14	0.28	0.05	0.21	1	0.00	0.24
BaO	0.00	0.25	0.12	-0.06	0.48	0.14	0.42	0.30	0.00	1	0.47
TiO_2	**0.57**	0.31	**0.69**	-0.45	**0.68**	**0.70**	**0.62**	0.19	0.24	0.47	1

Table 2. Interelemental Pearson correlation matrices (Lee Rodgers and Nicewander, 1988) for bulk rock major element geochemical data from the Katherine Group ironstones, calculated using X-ray fluorescence data. Bold numbers highlight significant correlation.

5.2 Iron speciation

The McClure Formation shales, mudstones and siltstones show significant variation in their iron speciation profiles (Fig. 18B). Enrichments in highly reactive iron (Fe_{HR}) begin to increase starting with the first appearance of ferruginous mudstones in the middle McClure Formation, before decreasing again leading up to the first ironstone horizon. These trends in Fe_{HR} do not show an obvious relationship to Fe/Al ratios (g/g). Values for iron sequentially extracted by sodium acetate (Fe_{carb}) and the chromium reduction method (Fe_{py}) are consistently low throughout the McClure Formation. Instead, iron extracted by sodium dithionite (Fe_{ox}) and ammonium oxalate (Fe_{mag}) drives much of the variation, and these leachates reach high iron contents in the ferruginous mudstones and siltstones (Fe_{ox} < 4.3 wt%; Fig. 18B).

5.3 Rare earth elements and Nd isotopes

Enrichments in Eu are often discussed in terms of Eu anomalies, i.e., the ratio of the UCC-normalised Eu value (Eu_n) to the expected value (Eu_n^*) assuming a constant ratio of concentrations between near-neighbour elements (Lawrence et al., 2006). Because Gd can also behave anomalously during estuarine mixing and seawater scavenging, Sm and Tb are used for Eu, i.e.:

$$Eu_n^* = (Sm_n^2 \times Tb_n)^{1/3} \quad (5)$$

The non-ferruginous shales and siltstones of the McClure Formation do not show any clear trend in terms of their Eu anomaly, and typically show negative Eu anomalies ($0.79 \leq Eu_n/Eu_n^* \leq 0.90$; mean 0.84; n = 7). The ferruginous siltstones (0.79–0.94; mean 0.85; n = 7) show similar Eu_n/Eu_n^* values to the non-ferruginous lithologies preceding the ironstone interval, whereas the oolitic ironstones have slightly higher Eu_n/Eu_n^* values (0.84–1.13; mean 0.95; n = 6). The Katherine $\varepsilon Nd(t)$ values show a wide range of negative values, ranging from -16.66 to -4.33 (mean -7.16; n = 6).

When normalised to MuQ (Kamber et al., 2005), the Katherine ironstones are generally depleted in light REEs (La–Nd), enriched in the middle REEs (i.e., Sm–Gd), with flat heavy REE (Ho–Lu) profiles. Total REE content shows a positive correlation with TiO_2 (a proxy for detrital input), however, there is no clear correlation between TiO_2 and Eu_n/Eu_n^* (Fig. S1).

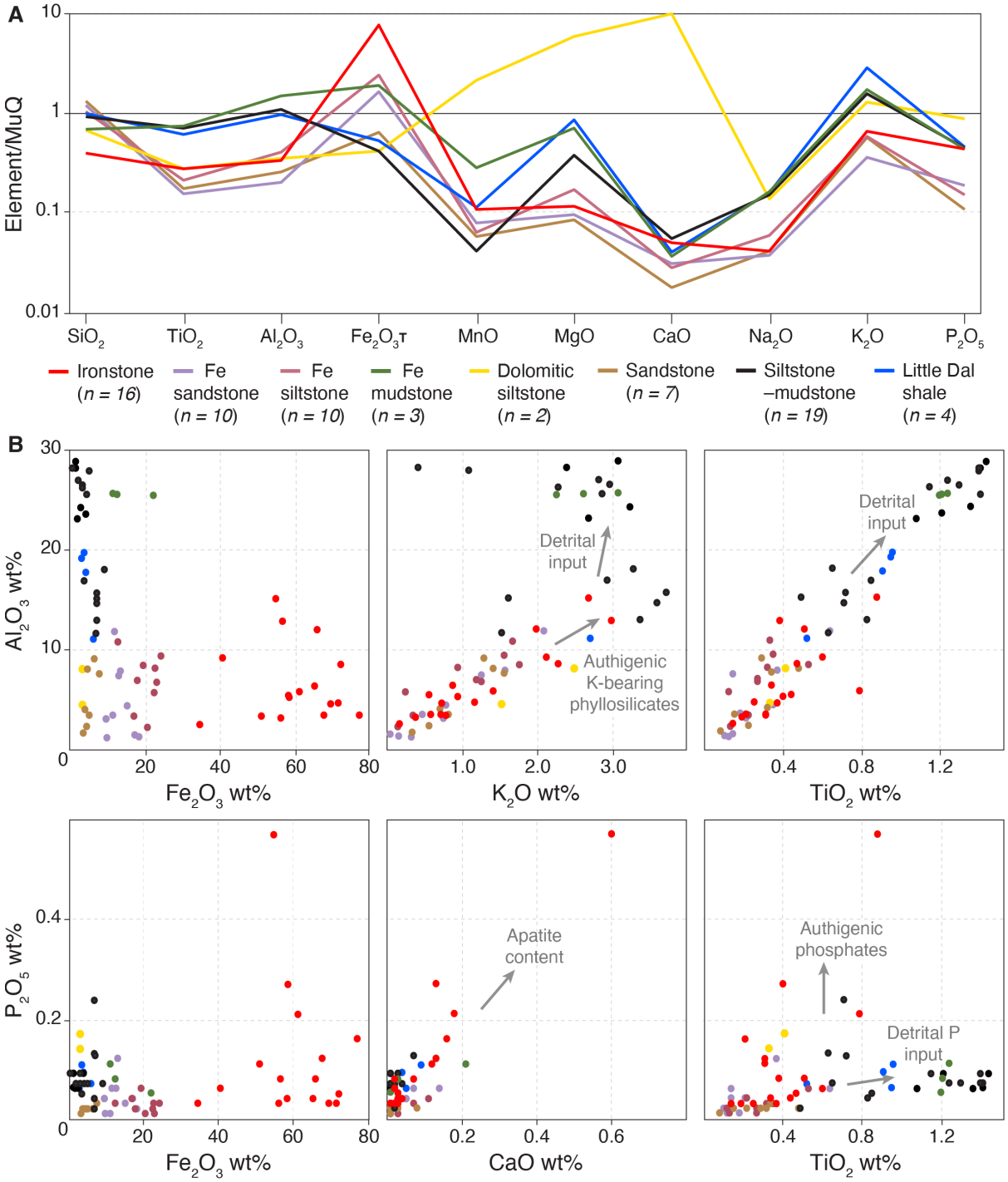

Fig. 16. X-ray fluorescence data showing the bulk-rock major element oxide composition of the Katherine ironstone, compared to the non-ferruginous host lithologies. **A.** Spider diagram showing the average major element contents of the different lithologies of the upper Katherine Group, normalised to Queensland mud (MuQ; Kamber et al., 2005). The Katherine Group lithologies are strongly depleted in Na_2O and CaO. **B.** Cross-plot diagram showing the relationship between various bulk-rock major element components for the upper Katherine Group. Elements that correlate positively with TiO_2 are interpreted to indicate detrital input (as indicated by the grey arrows), whereas other correlations can indicate the presence of authigenic phases such as K-bearing phyllosilicates (K_2O and Al_2O_3) and apatite (CaO and P_2O_5).

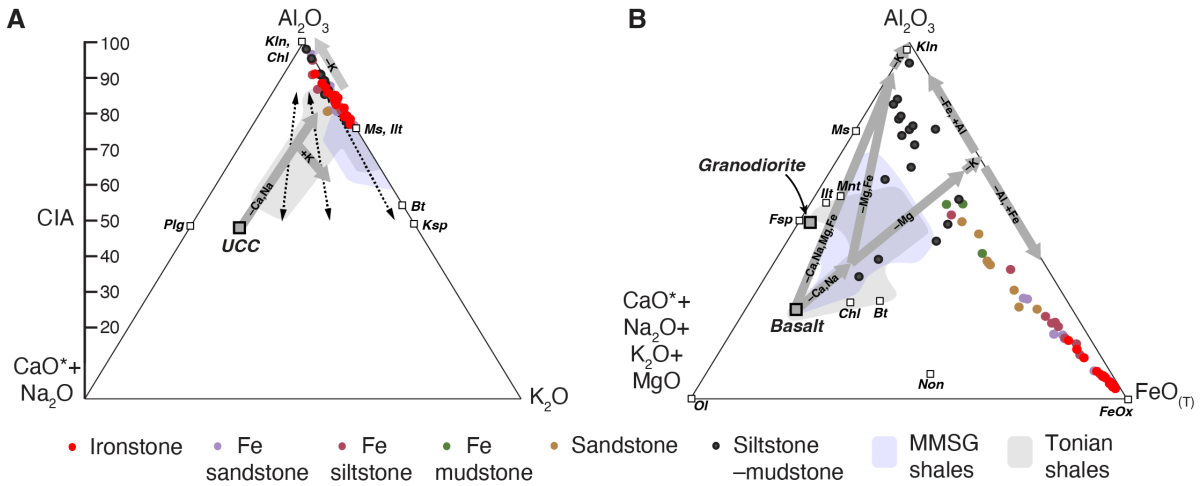

Fig. 17. A. Bulk rock major element geochemical data from the McClure and Abraham Plains Formations and basal Little Dal Group shales represented by an A–CN–K ternary plot using the molar proportions of major element oxides. The vertical axis shows the corresponding Chemical Index of Alteration (CIA) values. The dark grey arrows indicate a schematic weathering trend (modified from Nesbitt et al., 1997) showing the loss of labile elements from a felsic bedrock (represented by Upper Continental Crust; Taylor and McLennan, 1985), as well as the effect of K addition on the resultant weathered residue (Fedo et al., 1995). The dashed black lines represent the possible effects of sorting during transport and deposition, with mud toward the top of the arrow and sand toward the bottom(Nesbitt et al., 1996). **B.** A–L–F plot used to investigate mafic rock-weathering and extreme weathering processes (Nesbitt and Wilson, 1992), where L = labile = $CaO^*+Na_2O+K_2O+MgO$, and FeO_T represents the total Fe content expressed as FeO. The grey arrows highlight the array of weathering pathways for a basaltic source rock (Babechuk and Fedo, 2022) under various conditions involving Fe loss (i.e., via reducing weathering of Fe^{2+} or the leaching of Fe(III) complexes), as well as lateritisation. These data are consistent with a scenario whereby the McClure Formation mudstones (unlike other Tonian mudstones) experienced Fe loss during weathering, transport or diagenesis, whereas the ironstones and ferruginous siltstones were enriched in Fe. A felsic source (granodiorite from Nesbitt et al. 1997) is also shown. In both diagrams, the blue shaded area indicates the range of values from mudstones from other units in the Mackenzie Mountains Supergroup (MMSG) in the Wernecke Inlier (Hematite Creek and Little Dal groups; n = 39; Maloney et al., 2024) and Coal Creek Inlier (Fifteenmile Group; n = 186; Sperling et al., 2013), and the black shaded area shows the range of values from other Tonian mudstones reported from Svalbard (Kunzmann et al., 2015; n = 27), South China (Wang et al., 2011; n = 12) and North China (Hu et al., 2020; n = 20). The composition of selected key minerals are also shown: Bt = biotite; Chl = chlorite; FeOx = iron oxide; Ilt = illite; Kln = kaolinite; Ksp = K-feldspar; Mnt = montmorillonite; Ms = muscovite; Non = nontronite; Ol = olivine; Plg = plagioclase (Babechuk and Fedo, 2022).

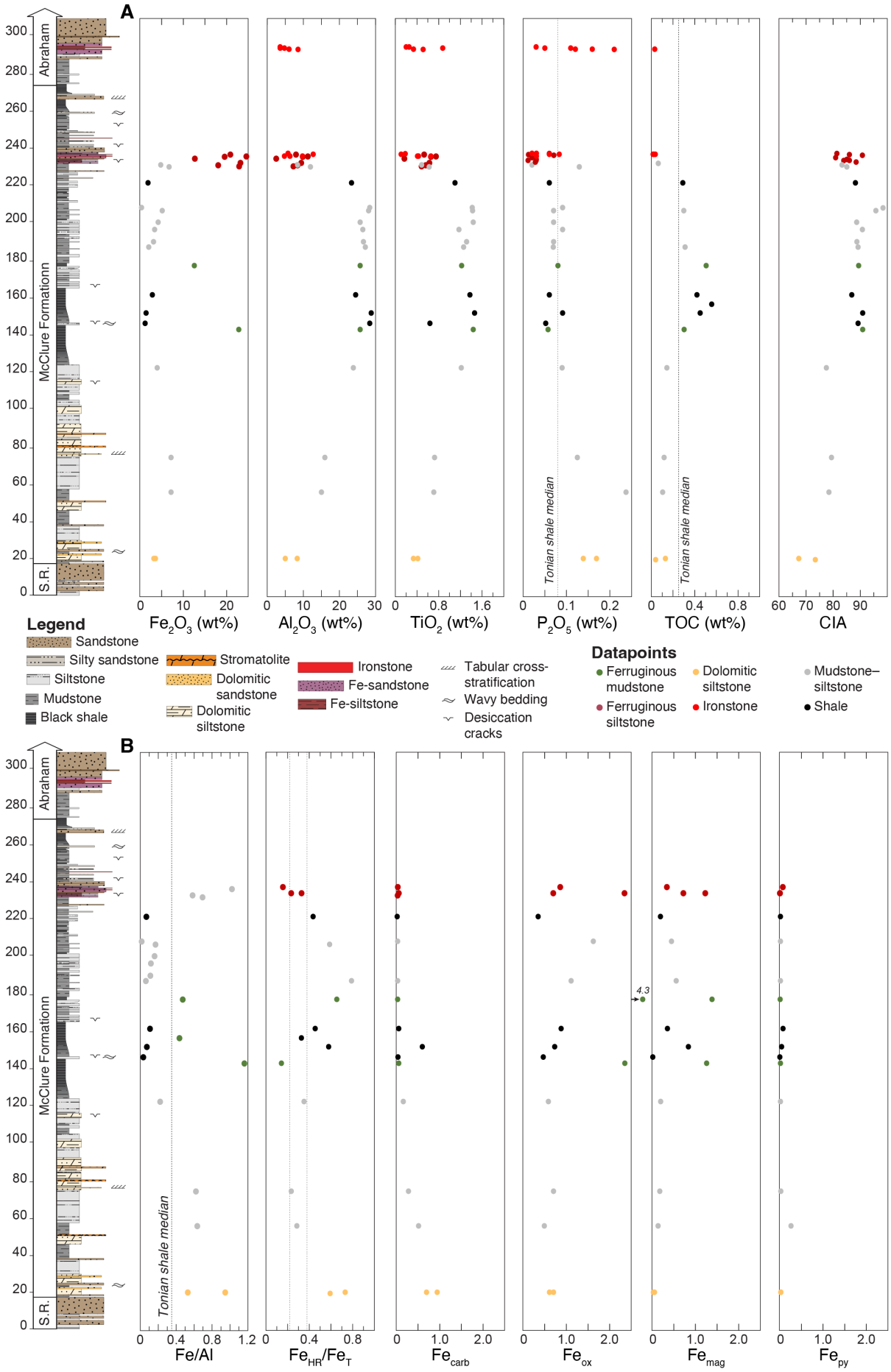
A
Abraham
McClure Formationn
S.R.
300
280
260
240
220
200
180
160
140
120
100
80
60
40
20
0
0 10 20
Fe2O3 (wt%)
0 10 20 30
Al2O3 (wt%)
0 0.8 1.6
TiO2 (wt%)
0 0.1 0.2
P2O5 (wt%)
Tonian shale median
0 0.4 0.8
TOC (wt%)
Tonian shale median
60 70 80 90
CIA
Legend
Sandstone
Silty sandstone
Siltstone
Mudstone
Black shale
Stromatolite
Dolomitic sandstone
Dolomitic siltstone
Ironstone
Fe-sandstone
Fe-siltstone
Tabular cross-stratification
Wavy bedding
Desiccation cracks
Datapoints
Ferruginous mudstone
Ferruginous siltstone
Dolomitic siltstone
Ironstone
Mudstone–siltstone
Shale
B
Abraham
McClure Formationn
S.R.
Tonian shale median
0 0.4 0.8 1.2
Fe/Al
0 0.4 0.8
FeHR/FeT
0 1.0 2.0
Fecarb
0 1.0 2.0
Feox
4.3
0 1.0 2.0
Femag
0 1.0 2.0
Fepy

1

Fig. 18. Chemostratigraphic profiles showing the stratigraphic variation in the bulk rock geochemical data and organic carbon content of fine-grained siliciclastic rocks (mudstones, siltstones) and ironstones. **A:** Major element oxide (from XRF data) and organic carbon (TOC) contents. General trends of fine-grained siliciclastic rocks (i.e., mudstones and siltstones) show an increase in the immobile elements Al_2O_3 and TiO_2—a proxy for detrital input—and a concomitant decrease in P_2O_5. This interpreted increase in detrital input corresponds to high Chemical Index of Alteration (CIA) values, which may suggest a flux of material from source rocks subject to intense chemical weathering. Median values for Tonian shales are based upon Reinhard et al. (2017) for P_2O_5 and Woltz et al. (2020) for TOC. **B.** Iron speciation data showing the ratio of highly reactive Fe (Fe_{HR}) to total Fe (Fe_T), with Fe_{HR}/Fe_T ratios greater than 0.22 and 0.38 highlighted with a dotted line (median Tonian shale Fe/Al ratio from Sperling et al., 2013; Thomson et al., 2015). The Fe enrichments of the ferruginous mudstones are largely due to Fe-rich phyllosilicates, with only relatively minor contributions of Fe oxides and Fe carbonates (as indicated by XRD data; Fig. 8), hence the muted Fe_{HR}/Fe_T values.

5.4 In situ major and trace elements

Electron microprobe analyses indicate that several distinct phyllosilicate phases are present, including: (1) a K-rich berthierine that is abundant in the ironstone matrix and form the cortical laminae of ooids, pisoids and oncoids; (2) a K-, Mg-rich berthierine that overprints the cortical laminae of iron oncoids; (3) a pore-filling, K-, Fe-rich phyllosilicate; (4) a pore-filling, K-, Mg-, Fe-rich phyllosilicate; and (5) a crack filling Fe-rich phyllosilicate cement (Fig. 19A). The differences in in-situ Al/Si ratios as well as K and Mg contents of the different phyllosilicates (Fig. 16) show that these are distinct phases. However, because the phyllosilicates are often mixed at a scale smaller than the spot size of the electron microprobe analyses (25 μm), the results incorporate multiple phases (usually hematite). These data also show an enrichment of P in the pore-filling, K-, Fe-rich phyllosilicate, and significantly elevated P contents in the oncoid berthierine (mean = 0.15 wt% P; n = 11; Fig. 19B) compared to the matrix berthierine (mean = 0.04 wt% P; n = 7). There is a strong correlation between Mn, Co and Zn (Fig. 19C). A similar relationship was not clearly observed for other transition metals (V, Fe, Cr, Ni), despite a positive correlation between Co, Zn and Ni for all phases (Fig. 19D), with greater enrichments in the phyllosilicate phases than in the hematite components.

When considering all ironstone components, P does not typically show a clear correlation with other elements. However, focusing specifically on the berthierine oncoid laminae, several trends emerge. For these components, P contents show a strong positive correlation with Ca (Pearson's correlation coefficient R = 0.77), Co (R = 0.71), Zn (R = 0.71), Ba (R = 0.87), and Th (R = 0.96). Iron contents show a positive correlation with redox-sensitive metals V (R = 0.83), Mo (R = 0.70), W (R = 0.84) and U (R = 0.86) for the berthierine oncoid laminae, and yet generally show a negative correlation with V and W for the hematite phases.

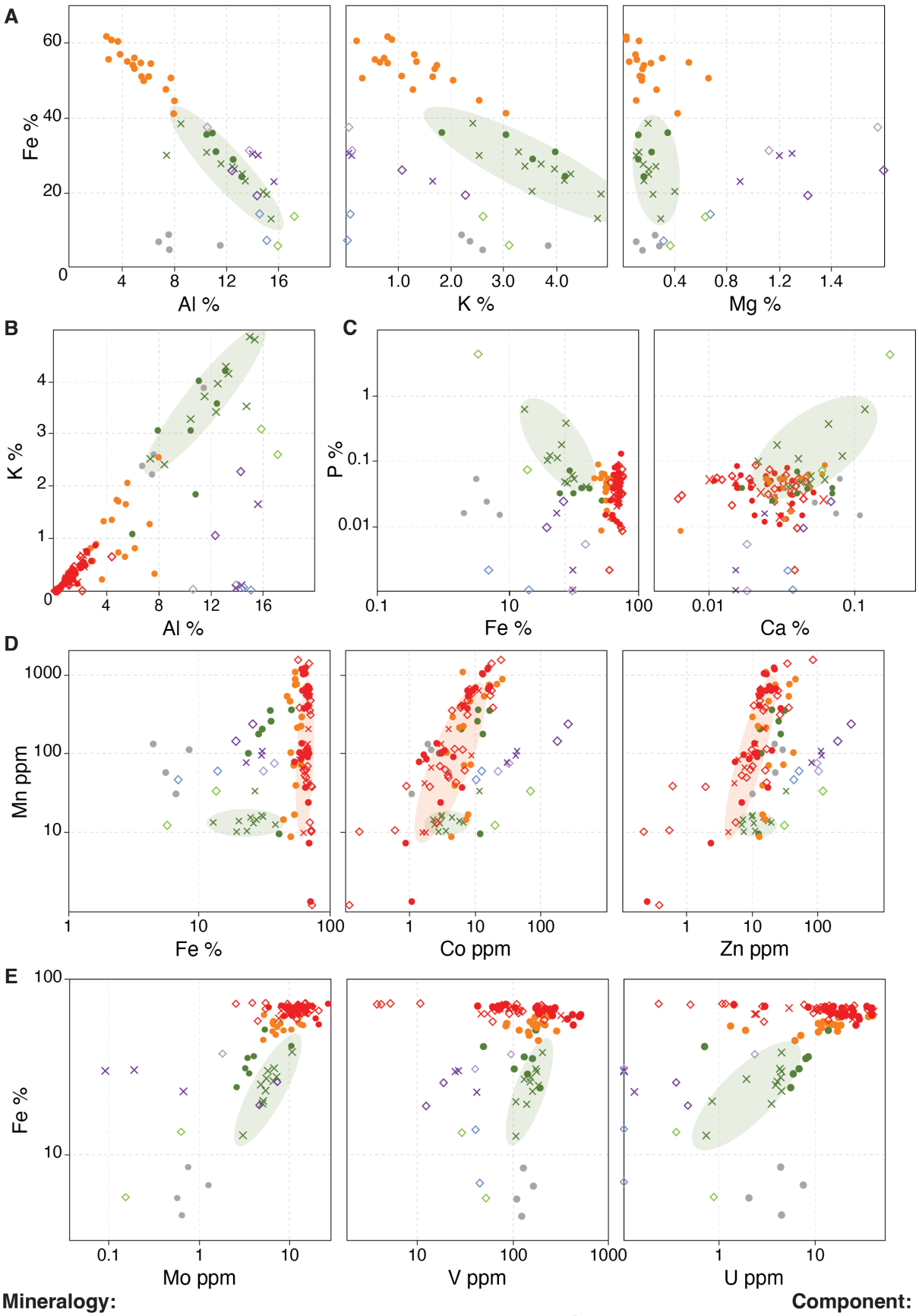

Fig. 19. Electron microprobe and LA-ICP-MS data showing the in situ geochemical composition of the various components of the Katherine ironstone. Green ellipses are data from berthierine oncoid cortices; red ellipses are

from hematite oncoid cortices. **A.** In situ major element geochemistry of the ironstone phyllosilicate phases. Values for hematite phases (which are close to 100 % Fe_2O_3) are not shown. **B.** Cross plot showing a strong positive correlation between K and Al, as these elements are mostly hosted by K-berthierine. **C.** Distribution of ironstone Fe and P contents, showing a relative enrichment of P in the berthierine oncoid cortices compared to the hematite components. **D.** Cross plot showing the relationship between Mn and other transition metals, showing a positive relationship between Mn, Co and Zn for the hematite components; this relationship is not observed for the berthierine oncoid cortices. **E.** Cross plots showing a positive correlation between Fe, Mo, V and U for the berthierine oncoid cortices.

6. Geochemical interpretation

6.1 Insights from major and trace element geochemistry

The major element geochemistry of Fe-rich sedimentary rocks can be used to constrain the source and cycling of their various geochemical components. The abundant K–Mg–Fe phyllosilicates and the strong positive correlations between Al, K and Mg (Table 2; Figs. 16–17) suggest that phyllosilicate authigenesis controls much of the variation in the Al contents of the upper Katherine Group lithologies. However, the positive correlation between Al_2O_3 and TiO_2 contents (Table 2; Figs. 16–17) supports the interpretation that Al availability was ultimately controlled by detrital (continental) flux.

There is a distinct chemostratigraphic trend throughout the McClure Formation with respect to the Al and Ti contents (Fig. 18), which steadily increase up-section. This increase in immobile elements suggests an increased detrital input which coincides with regression from a subtidal to a peritidal environment. The sudden decrease in Al and Ti contents in siltstones interbedded with the lowermost ironstone interval (Fig. 18) coincides with an increase in Si content related to an increased quartz sand supply. Despite these trends, the lack of a clear correlation between Fe and proxies for detrital input (e.g., Al, Ti; Figs. 17–18) suggests that Fe enrichment is not simply controlled by detrital input and shows that Fe cycling was involved.

Phosphorus in seawater is effectively scavenged by the precipitation of authigenic Fe minerals, such as ferrihydrite, green rust, and vivianite (Bjerrum and Canfield, 2002; Zegeye et al., 2012; Derry, 2015). Therefore, the P content of marine Fe-rich chemical sedimentary rocks has been used to constrain nutrient availability in the geologic past (Bjerrum and Canfield, 2002; Planavsky et al., 2010b). Authigenic phosphates (francolite, monazite, rhabdophane) are an important control on P distribution in the Katherine ironstone, and these phases are preferentially incorporated into the berthierine components (as shown in Fig. 15). A broad decreasing trend in P content accompanies an increase in detrital proxies (Al, Ti), which may be due to dilution from quartz and other detrital minerals.

Manganese is supplied to seawater from silicate weathering (Gross, 1965b) and hydrothermal exhalation (Von Damm, 1990). Manganese is soluble in aqueous systems under reducing conditions (as (Mn(II)) and relatively insoluble (as Mn(III) or Mn(IV)) under oxidising conditions (Tribovillard et al., 2006). The MnO_2/Mn(II) couple has a relatively high redox potential (Lide, 2004), and Mn oxides can be reduced in the presence of aqueous Fe(II) (coupled to Fe(II) oxidation; Hongve, 1997). Therefore, Mn oxides are susceptible to reductive dissolution during early diagenesis (Calvert and Pedersen, 1996; Johnson et al., 2016), and the Mn contents of marine sediments can potentially be used as a palaeoredox indicator. The positive correlation between Mn, Co and Zn for both the hematite and berthierine-dominated phases of the Katherine ironstone (Fig. 19) may be due to the scavenging of dissolved Co(II) and Zn(II) from seawater by adsorption onto the negatively charged surface of precipitating Mn oxides (Fernex et al., 1992; Moffett, 1994), as documented for Cenozoic marine ferromanganese deposits (Hein et al., 2017). However, the lack of Mn enrichment in the bulk rock ironstone likely implies reductive Mn oxide dissolution during suboxic diagenesis and may suggest that Mn oxidation was not a major process during ironstone deposition.

While cations such as Co, Zn, Ni and Ba sorb to negatively charged Mn oxides, the negatively-charged complexes of anions such as V, Th and U sorb more readily to the positively charged Fe oxyhydroxides (Koschinsky and Hein, 2017). The positive relationship between Fe, V and U in the berthierine oncoid cortices implicates primary Fe oxyhydroxide precipitation and shuttling in the formation of the berthierine precursor phases.

6.2 Chemical weathering indices

The major element composition of siliciclastic sedimentary rocks can be used to gain insights into source-to-sink petrogenesis, including source rock geochemistry, the nature and extent of catchment weathering, and other sedimentary processes. In particular, the Chemical Index of Alteration (CIA) can be used as a proxy for the degree of weathering experienced by the source material of sedimentary rocks (Nesbitt and Young, 1982). Chemical weathering preferentially leaches mobile cations such as

Ca^{2+}, Na^{+} and K^{+} ions by hydrolysis reactions, leaving behind immobile elements such as Al_2O_3, and this process scales with temperature and moisture. Therefore, the CIA has been used as a proxy for the integrated weathering history of the drainage of a sedimentary basin—and therefore local climate conditions—in deep time (Li and Yang, 2010; Wang et al., 2020). Although it is difficult to compare CIA values between different sedimentary successions due to variable influence of other factors such as sediment grain size and source rock composition, the extremely high CIA values of the Katherine Group sedimentary rocks (up to 98 for mudstones and siltstones; Fig. 18A) are consistent with a deeply weathered provenance (Nesbitt and Young, 1982). Drainage basins related to sites of modern tropical weathering are associated with Fe phyllosilicate authigenesis (Rude and Aller, 1989), and Phanerozoic oolitic ironstones are often associated with high CIA values and suggested to be genetically linked to periods of lateritic weathering (Myers, 1989; Salama et al., 2014; Baioumy et al., 2017; Rahiminejad and Zand-Moghadam, 2018). Similar intense weathering may have been an important process supplying the requisite cations for ironstone genesis to the Katherine basin. However, there are several independent processes which can affect the major element composition of clastic sedimentary rocks during source weathering, transportation, diagenesis and post-depositional alteration, and caution is needed when interpreting CIA values.

Weathering processes can be investigated using molar oxide ternary plots (Fig. 17)(Nesbitt and Wilson, 1992; Fedo et al., 1995; Babechuk and Fedo, 2022), by comparing the geochemistry of sedimentary rocks to the trends expected for the weathering of different parent rock lithologies. An A–CN–K ternary diagram, which plots the molar proportions of bulk-rock Al_2O_3, CaO^*+Na_2O, and K_2O, can be used to assess the extent of feldspar weathering, as well as sorting and diagenesis in siliciclastic sedimentary rocks (Nesbitt and Young, 1982; Nesbitt et al., 1996; Nesbitt et al., 1997). The post-weathering addition of K can lower the CIA of sedimentary rocks, a process which may have affected the Katherine ironstone during diagenesis based upon the observation of K-bearing phyllosilicates described above. Plotted on the A–CN–K diagram, the Katherine ironstone and mudstone data do not show clear evidence for a strong influence of this process on CIA values (Fedo et al., 1995). Mechanical sorting of the muds and sands of weathering residues by fluvial, estuarine and tidal processes can also affect the CIA value (Nesbitt et al., 1996), and while this likely (at least in part) explains the variability in the Al_2O_3 content of the Katherine Group sedimentary rocks, on the A–CN–K plot the Katherine ironstone and mudstone samples appear to have experienced a greater extent of weathering compared to other Tonian mudstones, including those from other units in the Mackenzie Mountains Supergroup (Fig. 17A).

The nature of the controls on the variability of the major element geochemistry of the Katherine Group sedimentary rocks can be explored in more detail using an A–L–F plot, where L refers collectively to the molar contents of the more labile element oxides (CaO, Na_2O, K_2O, and MgO). These can be contrasted to the more immobile FeO_T (total iron) and Al_2O_3 to investigate mafic rock-weathering and extreme weathering processes (Nesbitt and Wilson, 1992; Babechuk and Fedo, 2022). Within this framework, the Katherine mudstones are consistent with the extreme weathering and Fe loss during weathering, transport and/or diagenesis. For the Katherine ironstones the different possible pathways of authigenic Fe enrichment complicate this interpretation. These trends in A–L–F space may have been affected by the physichochemical separation of terrestrial Fe complexes from clay minerals resulting from estuarine mixing, or may be the product of mixing between a mixed clay composition and Fe oxides. In any case, the deposition of iron-rich sedimentary rocks would be promoted in scenarios where the drainage from the weathering of an Fe-rich parent rock results in Fe mobilisation, with connectivity to the marine realm. The nature of the parent rock that was weathered to supply sediment to the depositional basin of the Katherine Group is enigmatic, because crystalline basement is not exposed in Yukon (Norris and Dyke, 1997; Thorkelson et al., 2005), and Proterozoic palaeosols have not been documented. However, it is possible that Fe-rich residues may have derived from the weathering of late Palaeoproterozoic–early Mesoproterozoic units in the region, such as the mafic volcanics of the Bonnet Plume River Intrusions (Thorkelson et al., 2001), Slab volcanics (Laughton et al., 2001), and/or the Fe-rich, hydrothermal breccia zones that crosscut the Wernecke Supergroup (Delaney, 1981; Hunt et al., 2010). Because similarly values that suggest high degrees of chemical weathering are not observed in other Tonian units from the Mackenzie Mountains Supergroup in the region—and ironstones have not been observed elsewhere in Yukon—this may imply a local or short-lived process supplying Fe to the depositional setting.

6.3 Insights from iron speciation

Iron speciation is a geochemical proxy that uses the relative abundance of different pools of Fe minerals (as defined by sequential extraction techniques) of sedimentary rocks in order to infer the redox conditions of the water column during deposition (Canfield, 1989; Raiswell and Canfield, 1998). This

technique is primarily calibrated for fine-grained siliciclastic sediments. Specifically, the amount of highly reactive Fe (Fe_{HR} = Fe_{carb} + Fe_{ox} + Fe_{mag} + Fe_{py}) present in sedimentary rocks is normalised to the total amount of Fe (Fe_T) to allow for dilution by detrital input, and the Fe_{HR}/Fe_T ratio is used to track authigenic Fe enrichment. Because of the poor solubility of Fe(III), low levels of Fe_{HR} (i.e., Fe_{HR}/Fe_T < 0.22) are characteristic of sediments deposited under well-oxygenated water columns (Poulton and Canfield, 2011). Conversely, high proportions of Fe_{HR} (i.e., Fe_{HR}/Fe_T > 0.38) are interpreted to indicate authigenic Fe enrichment in an anoxic water column (Poulton and Canfield, 2011). Because Fe_{HR} enrichments can be diluted by rapid sedimentation (Raiswell and Canfield, 1998), and Fe_{HR} can be transformed into less-reactive phases or lost to the water column as a result of diagenetic processes (Chen et al., 2020; Poulton, 2021), intermediate values are equivocal (Poulton and Canfield, 2011).

These iron pools are operationally defined, and the sequential leach steps can dissolve more minerals than those targeted by the leaching method. In particular, iron phyllosilicates may be partly extracted during ammonium oxalate leaching (Hepburn et al., 2020; Slotznick et al., 2020). Petrographic examination indicates that magnetite is near-absent in these samples. Therefore, it is likely that the leaching of berthierine during the ammonium oxalate extraction is responsible for the high Fe_{mag} contents of the McClure Formation mudstones. This may also explain why some of the iron-rich mudstones (i.e., with Fe/Al ratios in excess of 1) can have relatively low Fe_{HR}/Fe_T ratios (Fe_{HR}/Fe_T < 0.22); much of the iron which was originally supplied as Fe_{HR} has been converted to phyllosilicates which are not quantitatively leached using the standard extraction procedure. This scenario may be analogous to the modern Amazon shelf, where nearly a quarter of the Fe_{HR} delivered to the sediment pile is converted to authigenic phyllosilicates, which can complicate the interpretation of Fe speciation data (Vosteen et al., 2022). As such, we interpret the iron speciation data from the Katherine ironstone to be consistent with a high flux of reactive iron to the sediment pile and Fe phyllosilicate authigenesis.

The chemical weathering of continental rocks supplies sulphate to the sedimentary realm, which can lead to the precipitation of sulphate minerals, and H_2S generation during subsequent diagenetic sulphate reduction can lead to pyritization of reactive Fe. The proportion of Fe_{HR} present as pyrite (Fe_{py}) in sedimentary rocks tracks this process as a measure of the degree of pyritization. The negligible Fe_{py} content of the McClure Formation sedimentary rocks suggests that H_2S activity was low during sedimentation and early diagenesis (Poulton et al., 2004). A combination of a high flux of highly reactive Fe (oxhydr)oxides (such as during lateritic weathering) and persistent sedimentary reworking can maintain the dominance of bacterial Fe reduction over sulphate reduction (Aller et al., 1986; Lovley and Phillips, 1987), which may explain the paucity of pyrite in the McClure Formation. Instead, the sulphate could be transported laterally to deeper settings where bacterial sulphate reduction proceeds, leading to an offshore pyrite burial sink (Wijsman et al., 2001; Severmann et al., 2010). Commonly, Phanerozoic ironstones are temporally associated with offshore pyritic shales (Hallam and Bradshaw, 1979; Van Houten and Arthur, 1989; Gharaie et al., 2004; Pufahl et al., 2020). Geochemical evidence for euxinia around the time of deposition of the Katherine Group has been reported from basinal sediments of the Mackenzie Mountains Supergroup (Sperling et al., 2013) and correlative Tonian units in the Amundsen Basin (Thomson et al., 2015).

Importantly, the continental flux of Fe_{HR} to the coastal environment of the upper Katherine Group strata would likely have differed greatly from that of the contemporaneous open marine–basinal sediments. The intense weathering of continental silicate minerals leads to river waters enriched in Fe_{HR} (Schwertmann, 1988), and much of this Fe_{HR} is sequestered in coastal environments (such as estuaries and tidal flats) due to the effect of salinity on organometallic complexes (Raiswell, 2011). The average Fe_{HR}/Fe_T ratios of modern river sediments are therefore much higher than that of average modern marine sediments (Poulton and Raiswell, 2002), and the supply of Fe_{HR} from intense chemical weathering can affect the interpretation of iron speciation profiles in ancient sedimentary rocks (e.g., Wei et al., 2021). As such, we suggest that the iron speciation data of the coastal Katherine Group deposits are likely more indicative of local processes including chemical weathering inputs rather than basinal redox conditions. The resulting inference is that ironstone genesis took place in a setting supplied by Fe_{HR} from chemical weathering inputs in which iron cycling dominated over sulphide generation.

6.4 Rare earth element and Nd isotope constraints

Because of the strong association between rare-earth elements (REE) and Fe, REE systematics have long been used to investigate the iron source of iron-rich chemical sediments in deep time. Unlike the geochemically similar trivalent REE, Eu is redox sensitive and can be reduced to Eu(II) (Sverjensky, 1984). Divalent Eu is more compatible than other REE(III) in feldspars during magma differentiation, and high-temperature hydrothermal fluids typically feature strongly positive Eu anomalies due to the breakdown of feldspar in igneous rocks (Klinkhammer et al., 1983; Michard et al., 1983; Bau, 1991).

Positive Eu anomalies (i.e., $Eu_n/Eu_n^* > 1$) are characteristic features of Cenozoic ferromanganese crusts deposited in proximity to hydrothermal vent sites (e.g., Bau et al., 2014), as well as Archaean banded iron formations, which is considered to be indicative of a contribution of hydrothermally sourced Fe to these deposits (e.g., Fryer, 1977; Graf Jr, 1978; Barrett et al., 1988; Danielson et al., 1992; Bau and Dulski, 1996). The Eu anomalies in Fe-rich chemical sedimentary rocks are difficult to overprint during metamorphism and fluid alteration except under very high fluid–rock ratios (Bau, 1991). The incorporation of a strongly positive Eu anomaly into chemical sediments is sensitive to redox conditions, and is more readily preserved in dominantly anoxic oceans (Bau and Dulski, 1999). However, the documentation of positive Eu anomalies in some Neoproterozoic iron formations (Hu et al., 2017; Lei et al., 2020; Sun et al., 2023) suggests that the transport of a hydrothermal Eu signature was possible during this time as well. Therefore, the lack of positive Eu anomalies in the Katherine ironstone is consistent with a continental, rather than hydrothermal, Fe source. The negative Eu anomalies present to some degree in the Katherine ironstone, and to a greater extent in the host mudstones, may reflect the contribution of rare earth elements from a highly weathered continental source material with significant decomposition of feldspar to kaolinite (Babechuk et al., 2019). Similarly, negative Eu anomalies in some Phanerozoic oolitic ironstones have been interpreted as a signal inherited from source material (Sturesson, 1995). Regardless, we suggest that there is no evidence from REE enrichments for a high-temperature hydrothermal origin of the Katherine ironstone.

The initial Nd-isotopic ratio ($\varepsilon Nd(t)$) of marine chemical sediments is widely used as a proxy for the composition of the fluids from which they precipitated (e.g., Shaw and Wasserburg, 1985; van de Flierdt et al., 2004; Tachikawa et al., 2014). Because Sm is a more compatible element during partial melting of the mantle, REE sourced from the weathering of ancient, continental rocks have negative $\varepsilon Nd(t)$ values, whereas those sourced from younger, mantle-derived sources such as hydrothermal venting and volcanism are characterised by more positive $\varepsilon Nd(t)$ values (Piepgras et al., 1979; Goldstein and Jacobsen, 1987; Jeandel et al., 2007). Like the Eu anomaly, Nd isotope systematics have been used as a proxy for tracking iron sources to iron formations. Radiogenic Nd isotope characteristics (typically $-3 \leq \varepsilon Nd(t) \leq +4$) are interpreted to represent a hydrothermal Fe contribution to these deposits (Miller and O'Nions, 1985; Jacobsen and Pimentel-Klose, 1988; Alexander et al., 2009; Li et al., 2015; Cox et al., 2016a). In contrast, the Katherine ironstone is characterised by crustal $\varepsilon Nd(t)$ values. While few studies have investigated the Nd isotope composition of ironstones, similarly negative $\varepsilon Nd(t)$ values have been documented in oolitic ironstones from the Statherian (average $\varepsilon N(t) = -6.8$, n = 6; Li and Zhu, 2012), Ordovician (average $\varepsilon Nd(t) = -8.3$, n = 5; Sturesson, 2003) and Jurassic (average $\varepsilon Nd(t) = -8.2$, n = 19; Schunck et al., 2023). Generally these have been interpreted to represent a continental Fe source (Li and Zhu, 2012; Schunck et al., 2023). Conversely, Sturesson (2003) suggested that a primary, juvenile signal of the iron ooids could have been overprinted by Nd sourced from associated detrital material during diagenesis, as has been observed in modern marine sediments (e.g., Jang et al., 2018). However, studies have shown that positive $\varepsilon Nd(t)$ values can be preserved in iron formations with a close association with siliciclastic rocks (e.g., Derry and Jacobsen, 1990; Stern et al., 2013; Yang et al., 2021), as is the case for Cryogenian-aged iron formation in the Windermere Supergroup of the Mackenzie Mountains (Cox et al., 2016a). Therefore, we suggest that the radiogenic $\varepsilon Nd(t)$ values of the Katherine ironstone are consistent with the supply of weathered continental material to the site of ironstone genesis rather than a strong hydrothermal influence on the source of Fe to these rocks. Finally, the consistently evolved Nd isotopic composition of Tonian shales from the underlying Hematite Creek Group and the Fifteenmile Group in the Coal Creek and Hart River inliers ($\varepsilon Nd(t) = -11$ to -3; Cox et al., 2016b) supports the interpretation that this region was subject to intense weathering conditions. The isolated occurrence of ironstone in the Mackenzie Mountains Supergroup demonstrates that ironstone genesis also required additional local environmental conditions.

7. Discussion

7.1 Ironstone depositional setting

Several factors such as continental relief, vegetation and climatic conditions play important roles in the supply of reactive Fe from the continents to the marine realm. As discussed in Section 4, the Katherine ironstone was deposited in nearshore settings, following a transition from a subtidal marine to tidal mudflats and an estuarine environment dominated by subaqueous sand dunes. We argue that this low-energy, protected coastal setting, is important for ironstone genesis. This stratigraphic placement of the Katherine ironstone within this sequence is similar to that of the iron ooids described from lagoonal–estuarine facies of the Vindeggen Group (Rjukan Rift Basin, southern Norway;

Köykkä and Lamminen, 2011), which overlie subtidal marine deposits and are overlain by a ravinement surface and shoreface-offshore environments. Phanerozoic oolitic ironstones are often interpreted to have been deposited in embayed coastal environments, including lagoonal, estuarine, back-barrier, shoal and tidal flat settings (e.g., Sheldon, 1970; Bayer, 1989; Guerrak, 1989, 1991; Khedr, 1991; Chan, 1992; Taylor et al., 2002; Salama et al., 2014; Durbano et al., 2015; Rudmin et al., 2017; Sokol et al., 2020). Other environments, such as lacustrine, shoreface and basinal settings have also been proposed for some ironstones (e.g., Siehl and Thein, 1989; Madon, 1992; Cranfield et al., 1994; Collin et al., 2005; Rahiminejad and Zand-Moghadam, 2018; Matheson and Pufahl, 2021). Continental oolitic ironstones (also known as channel iron deposits) are rare, and are best developed in Western Australia where iron is directly sourced from the abundant banded iron formation-hosted iron ore deposits of the Hamersley Basin (Morris and Ramanaidou, 2007). Therefore, we suggest that the most widely applicable depositional environments for oolitic ironstones are protected, nearshore environments which likely featured pH, Eh and salinity conditions that promoted ironstone genesis and accumulation. Further, barrier bars may have facilitated sorting as well as stratigraphic condensation (Sheldon, 1970; Bayer, 1989; Sokol et al., 2020).

Basin evolution and sea level regime are also important for ironstone genesis. The Katherine Group is interpreted to have been deposited following a first-order regression (Gibson et al., 2019), and experienced multiple phases of higher-order transgressions leading to the alternation of subtidal marine and peritidal–fluvial facies (Long et al., 2008; Turner and Long, 2008). Following this, ironstone was deposited near the top of the Katherine Group, and is overlain by a maximum flooding surface of a major transgression represented by the shales of the Little Dal Group (Turner, 2011b). Many other ironstones are interpreted to have been deposited during the latter stages of marine regressions (Hemingway, 1951; Hallam and Bradshaw, 1979; Bayer, 1989; Dreesen, 1989; Khedr, 1991; Madon, 1992; Salama et al., 2014), or the onset of transgression (Young, 1989; Chan, 1992; Donaldson et al., 1999; Abbott and Sweet, 2000; Taylor et al., 2002; Williams, 2003; Köykkä and Lamminen, 2011; Clement et al., 2020; Fürsich et al., 2021). Long-term (normal) regression would have led to the development of a broad coastal plain, which would have been suitable for the development of muddy tidal flats and provided a large area over which chemical conditions would have varied with tides, storms, and minor fluctuations in sea level. Channel migration would naturally recycle these sediments. These conditions may have promoted ironstone genesis. These environments would have been periodically affected by wave action, providing the agitation necessary for the fragmentation of intraclasts and the winnowing away fine-grained detritus. Regression would have promoted bed-load sediment transport and led to clastic traps along palaeotopographic highs, allowing ironstone accumulation in palaeodepressions (Hallam and Bradshaw, 1979). Deposition in these types of environments explains the spatial distribution of ironstones, which are often lenticular in the stratigraphic record, with the thickness controlled by depositional relief.

7.2 Iron source

The source of Fe for oolitic ironstones has been debated for over a century, and genetic models can broadly be grouped into those favouring Fe sourced from continental weathering (e.g., Cayeux, 1922; Taylor, 1949; Hallam, 1966; Chowns, 1968; Van Houten and Bhattacharyya, 1982; Myers, 1989; Rude and Aller, 1989; Zhao and Bi, 2000; Reolid et al., 2008; Andreeva and Chatalov, 2011; Yilmaz et al., 2015; Baioumy et al., 2017; Garnit and Bouhlel, 2017; Novoselov et al., 2018; Rahiminejad and Zand-Moghadam, 2018), and those favouring upwelling of ferruginous seawater, hydrothermalism and/or volcanism (Dreesen, 1989; Petránek, 1991; Cotter and Link, 1993; Kimberley, 1994; Heikoop et al., 1996; Sturesson et al., 2000; Yan et al., 2015; Di Bella et al., 2019; Lin et al., 2019; Todd et al., 2019; Abram and Holz, 2020; Pufahl et al., 2020; Bansal et al., 2021; Matheson et al., 2022; Vodrážková et al., 2022; Zhu et al., 2022; Yang et al., 2024). There is no clear geological evidence for contemporaneous volcanism or proximal hydrothermal activity in the depositional basin of the Katherine Group. Further, as discussed above, the geochemistry of the Katherine ironstone (i.e., continental Nd isotope composition, lack of Eu anomalies) argue against a dominant hydrothermal or volcanic Fe source.

The humid, coastal depositional setting of the Katherine ironstone would have likely experienced a high flux of continental Fe, Al and Si required for ironstone genesis, as gradients in salinity and pH at the freshwater–seawater interface would have affected the complexation of continental weathering products (Poulton and Raiswell, 2002; Raiswell, 2011; Pufahl et al., 2013; Sokol et al., 2020). The stratigraphic association of the ironstone with mature quartz arenite and mudstones with extremely high Chemical Index of Alteration values (Figs. 17–18) may suggest a deeply weathered, possibly Fe-rich source (Fig. 17), although further work is needed to substantiate the origins of this high

CIA signal. A lateritic source has been argued for many Phanerozoic ironstones (Van Houten and Karasek, 1981; Gorter, 1991; Opeloye et al., 2021). This inference is supported by palaeogeographic reconstructions of Rodinia, which suggest that northwestern Canada was probably located within tropical latitudes for most of the Tonian Period (Denyszyn et al., 2009; Eyster et al., 2017; Merdith et al., 2017). The lack of evidence for evaporites in the Katherine Group may also support the interpretation of a humid climate during deposition (Rankey and Berkeley, 2012; O'Connell et al., 2020), and evaporites are not commonly reported from ironstone-bearing successions in general. A lower sulphate supply may potentially explain the lack of sulphate evaporites in Precambrian ironstone successions, but the lack of halite (NaCl) argues against evaporitic conditions (Turner and Bekker, 2016).

High temperatures and humidity can also promote basin anoxia due to basin warming and eutrophication (e.g., Gharaie et al., 2004). Regardless of any local climate contribution, the Tonian oceans in general are considered to have been dominantly ferruginous (e.g., Sperling et al., 2013; Guilbaud et al., 2015; Kunzmann et al., 2015; Thomson et al., 2015; Gibson et al., 2020). Although the Fe concentrations of the marine reservoir are not well constrained (e.g., Song et al., 2017), it is likely that oceanic Fe contributed to the Katherine ironstone to some extent. Some models for oolitic ironstones argue for both continental input and more distal marine sources of Fe (e.g., Maynard, 1986; Dorland, 1999; Abram and Holz, 2020; Johnson et al., 2020a). However, if seawater was the most important Fe source, Fe deposits should occur more widely and in more distal marine environments in the Mackenzie Mountains Supergroup. More broadly, if the upwelling of Fe-rich seawater was the dominant control on ironstone genesis in general then these deposits would be expected to be much more common than their sporadic distribution in the Precambrian sedimentary record (Fig. 1), given lower marine O_2 and sulphate during this time (e.g., Poulton and Canfield, 2011). Further, because the Precambrian oceans were silica-rich (Siever, 1992), Precambrian ironstones forming from upwelling seawater would be expected to be cherty (due to Si scavenging and co-precipitation with Fe (oxyhydr)oxides; Fischer and Knoll, 2009), which is not the case for the Katherine and other Precambrian ironstones (Dorland, 1999; Pufahl et al., 2013; Lin et al., 2019; Johnson et al., 2020a; Qiu et al., 2020). Instead, we argue that continentally derived Fe controlled ironstone deposition during this time.

In modern circumneutral river waters, iron is largely transported as Fe(III) in organometallic colloids and nanoparticulate aggregates (Raiswell and Canfield, 2012). Compared to the modern, the Proterozoic atmosphere had low pO_2 (e.g., Liu et al., 2021) and high pCO_2 (e.g., Fiorella and Sheldon, 2017; Isson and Planavsky, 2018), and therefore low-Eh and low-pH river waters could have transported Fe^{2+} to coastal settings (e.g., Petránek, 1964; Pufahl et al., 2013), consistent with the Fe loss documented in some paleosols from this time (e.g., Mitchell and Sheldon, 2016). In addition, submarine groundwater discharge could have also been a significant source. In modern groundwater systems, much of the Fe^{2+} carried by groundwater gets trapped in the oxygenated margins of subterranean estuaries (e.g., Charette and Sholkovitz, 2002; Roy et al., 2010), yet the lower O_2 concentrations of Proterozoic shallow seawater may have facilitated a greater Fe^{2+} flux from groundwater (i.e., iron seeps) during this time. In particular, acidic groundwaters can be rich in Fe(II)-sulphatocomplexes and/or Fe(III)-hydroxocomplexes (Egal et al., 2008), and acid-rock drainage has been suggested as a potential source of Fe for Phanerozoic oolitic ironstones (Catt et al., 1971; Dabous, 2002; Salama et al., 2014). Therefore, river waters and groundwaters could have supplied large quantities of highly reactive Fe (including Fe^{2+}) to ironstone depositional environments. Regardless of the availability of acidic waters, we suggest that the Katherine ironstone was most likely dominated by continental Fe sources.

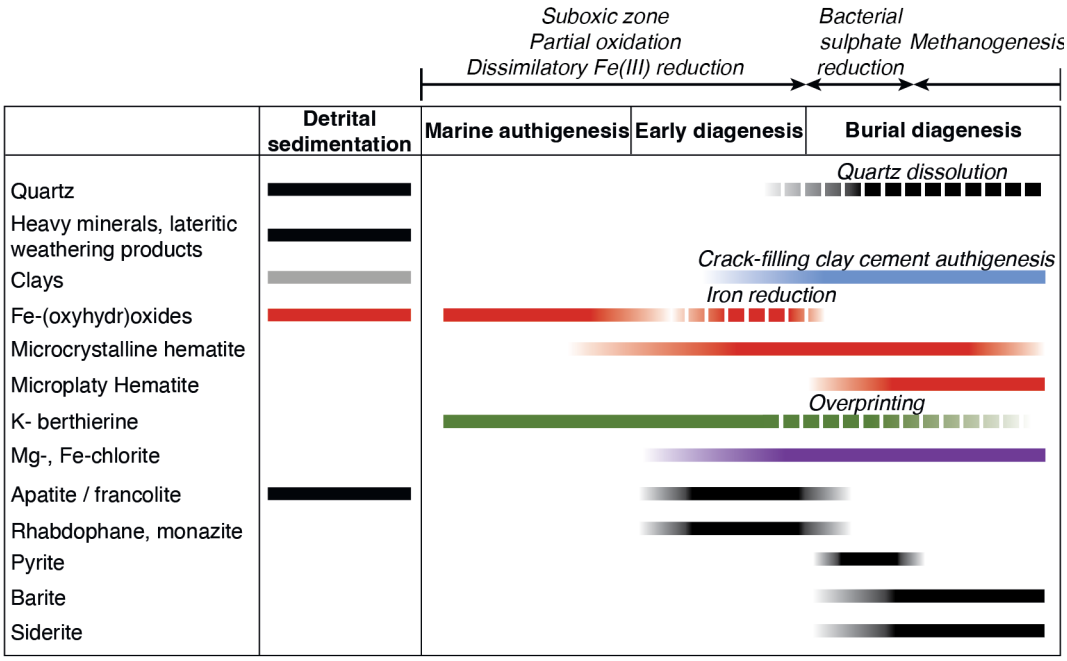

Fig. 20. Paragenesis of the Katherine ironstone, based upon petrographic textures and overprinting relationships of the mineral assemblage. In addition to the detrital material, the ironstone is largely composed of the diagenetic products of authigenic Fe (oxyhydr)oxides, Fe phyllosilicates, and phosphate minerals.

7.3 Ironstone paragenetic pathways and biogeochemical cycling

The textural relationships and fine interlamination of the Fe(III) (oxyhydr)oxides and Fe(II) phyllosilicates (with microcrystalline phosphates), show that these phases precipitated during sedimentation (Fig. 20). This observation, combined with the lack of sulphide or carbonate minerals, suggests that redox conditions oscillated between ferruginous and suboxic–oxic during sedimentation and early diagenesis. Deciphering the paragenesis of the ironstone therefore requires consideration of the Fe, Al, Si, P, C and S cycles. Chemical weathering of continental rocks could have supplied the site of ironstone genesis with the requisite cations, while the coastal setting created the Eh–pH conditions necessary for the precipitation of the authigenic components of the Katherine ironstone, as outlined below.

There are several distinct mechanisms by with Fe can be liberated during chemical weathering. The oxidative weathering of Fe sulphides (i.e., acid-rock drainage) solubilises Fe^{2+} and produces sulphuric acid (Kleinmann et al., 1981):

$$FeS_2 + 14Fe^{3+} + 8H_2O \rightarrow 15Fe^{2+} + 2SO_4^{2-} + 16H^+ \quad (6)$$

This process, facilitated by acidophilic iron-oxidising proteobacteria (Singer and Stumm, 1968), typically leads to the generation of Fe(III) (oxyhydr)oxides and sulphate under oxic conditions. Subsequent bacterial sulphate reduction produces H_2S during diagenesis which can lead to Fe sulphide generation (Curtis and Spears, 1968; Curtis, 1987a), e.g.:

$$15CH_2O + 2Fe_2O_3 + 8SO_4^{2-} \rightarrow 4FeS_2 + 7H_2O + 15HCO_3^- + OH^- \quad (7)$$

Pyrite is rare in ironstones, and is typically found as a post-depositional phase (Taylor and Curtis, 1995), though some ironstones contain authigenic aluminium phosphate–sulphate minerals (Salama, 2014; Xie et al., 2024). These minerals can form during early diagenesis in terrestrial and coastal marine sedimentary rocks due to a supply of amorphous $Al(OH)_3$, HPO_4^{2-}, and $2SO_4^{2-}$ produced from the oxidising and acidic weathering of sheet silicates, phosphates and sulphide minerals (Pe-Piper and Dolansky, 2005; Galán-Abellán et al., 2013). Sulphur-bearing minerals are near-absent in the Katherine ironstone, and rare in the Katherine Group in general. However, acid-rock drainage produces much more Fe^{2+} than sulphate (Equation 6), and while Fe(II) hydroxysulphates and jarosite are common acid-rock drainage products at low pH, Fe(III) hydroxide precipitation dominates at higher alkalinity and when sulphate availability is low (Carlson and Schwertmann, 1980; Clarke et al., 1997). In general, the Tonian oceans are considered to have been sulphate-poor (Guilbaud et al., 2015; Fakhraee et al., 2019), and any continental sulphate would have been diluted in marine environments. Any diagenetic sulphide could have also been subsequently reoxidised by chemolithotrophic sulphide-oxidizing bacteria (Aller and Rude, 1988). Further, Fe reducers can outcompete sulphate reducers when Fe oxides availability

is high (Lovley and Phillips, 1987), and where sediment regeneration is extensive (as seen in the mobile mud belts associated with modern tropical deltaic systems; Aller et al., 1986). In any case, the mineralogy of the Katherine ironstone shows that sulphate reduction and pyritisation were not major processes during ironstone genesis.

In addition to sulphide oxidation, the chemical weathering of Fe-bearing silicate minerals can also produce Fe^{2+} and acidity, e.g.:

$$Fe_2SiO_4 + 4H_2CO_3 \rightarrow 2Fe^{2+} + 4HCO_3^- + H_4SiO_4 \quad (8)$$

This silicate weathering can lead to Fe phyllosilicate formation in several ways. The weathering of aluminosilicates provides the Al and Si cations necessary for authigenic clay formation (Ryan and Reynolds, 1996), and can lead to the neoformation of clays such as kaolinite, e.g.:

$$2KAlSi_3O_8 + 2H_2CO_3 + 9H_2O \rightarrow 2Al_2Si_2O_5(OH)_4 + 4H_4SiO_4 + 2K^+ + 2HCO_3^- \quad (9)$$

These neoformed, cation-poor clays can be transported to sedimentary environments where they can undergo further diagenesis. In particular, kaolinite can be readily transformed to berthierine in the presence of Fe^{2+} (Burton et al., 1987):

$$Al_2Si_2O_5(OH)_4 + 4Fe^{2+} + 8HCO_3^- \rightarrow Fe_2Al_2SiO_5(OH)_4 + H_4SiO_4 + 4CO_2 \quad (10)$$

In warm and humid environments, chemical weathering can proceed further:

$$2Al_2Si_2O_5(OH)_4 \rightarrow 4Al(OH)_3 + 4H_4SiO_4 + 5H_2O \quad (11)$$

This produces highly reactive lateritic residues that readily undergo diagenetic transformations to authigenic Mg-, K-, and Fe-bearing phyllosilicates (Rude and Aller, 1989), which can lead to berthierine authigenesis:

$$2Fe^{2+} + H_4SiO_4 + 2Al(OH)_3 + 4HCO_3^- \rightarrow Fe_2Al_2SiO_5(OH)_4 + 4CO_2 + 5H_2O \quad (12)$$

The berthierine of the Katherine ironstone could have been the product of early diagenetic reactions of these lateritic weathering products supplied to coastal environments.

The Katherine ironstone berthierine is intercalated with K-rich, chlorite-like layers, for which the K^+ cations could have been supplied from chemical weathering (Equation 9) (Meunier and El Albani, 2007), but was most likely sourced from the K-rich seawater. The incorporation of seawater K^+ would have been promoted by sediment resuspension, as is documented in the modern Amazon shelf (Michalopoulos and Aller, 2004; Spiegel et al., 2021).

Authigenic clay formation (i.e., Equations 10 and 12) consumes alkalinity while producing CO_2 and generating acidity; as such, these “reverse weathering” reactions can play an important role in terms of the buffering of Earth’s climate and marine pH over geological time (Garrels, 1965; Mackenzie and Kump, 1995; Michalopoulos and Aller, 1995). Reverse weathering is observed in modern tropical environments where Fe- and Al- (oxyhydr)oxides are supplied by lateritic weathering, and are rate-limited by the regeneration of biogenic silica (Michalopoulos and Aller, 2004). Reverse weathering rates are suggested to have been significantly higher in the comparatively Si-rich Precambrian marine environments (Isson and Planavsky, 2018; Krissansen-Totton and Catling, 2020), and sedimentary Fe-phyllosilicates have been used to track reverse weathering in deep time (Isson and Planavsky, 2018; Johnson et al., 2020a; Ma et al., 2022). Although syndepositional, authigenic berthierine has been documented in Proterozoic shales (Ma et al., 2022), Fe-poor phyllosilicates (such as illite) typically predominate (e.g., Subarkah et al., 2022). This shows that ironstone depositional environments (i.e., protected settings supplied with continental weathering products) were especially suited for reverse weathering.

The interlamination of oxidised and reduced Fe species in the coated grains (Fig. 13) suggests that Fe^{2+} oxidation was involved in ironstone genesis, and this inference is supported by the fractionated Fe isotope composition of the Katherine ironstone (and other Proterozoic oolitic ironstones; Wang et al., 2022) which is generally taken as a fingerprint of redox processes (Johnson et al., 2020b). The oxidation of Fe^{2+} is rapid in oxygenated, circumneutral aqueous environments, i.e.:

$$4Fe^{2+} + O_2 + 10H_2O \rightarrow 4Fe(OH)_3 + 8H^+ \quad (13)$$

This reaction is typically outcompeted by biological Fe^{2+} oxidation, which can be coupled to O_2 reduction under microaerobic conditions (facilitated by neutrophilic proteobacteria), nitrate reduction (facilitated by neutrophilic, nitrate-reducing proteobacteria), or photochemical reactions by photoautotrophic proteobacteria under anaerobic conditions (Emerson et al., 2012; Bryce et al., 2018; Kappler et al., 2021). In acid-rock drainage environments, acidophilic iron-oxidisers are often active, which are facultative anaerobes that can also reduce Fe(III) coupled to sulphide oxidation (Hedrich et al., 2011).

However, most modern iron seeps are dominated by neutrophilic, microaerobic iron oxidising proteobacteria (Druschel et al., 2008; Emerson et al., 2010):

$$12Fe^{2+} + O_2 + 2CO_2 + 32H_2O \rightarrow 2CH_2O + 12Fe(OH)_3 + 24H^+ \quad (14)$$

This process has been suggested to have contributed to the formation of other oolitic ironstones (Dahanayake and Krumbein, 1986; Salama et al., 2013; Lin et al., 2019; Qiu et al., 2020). Although estimates for seawater pH in the Precambrian span a wide range (Halevy and Bachan, 2017), seawater was likely more alkaline than river waters during the Tonian Period. Therefore, Fe^{2+} in low-pH river waters could have been oxidised by this process following discharge into the more alkaline, microaerobic seawater (e.g., Pufahl et al., 2013).

In addition to explaining the authigenic phases that are characteristic of the Katherine ironstone, a genetic model also needs to explain the absence of several notable minerals. For instance, the silicic acid produced by silicate weathering (Equation 8) can lead to silica precipitation (Krauskopf, 1956), and the Precambrian oceans were rich in Si (Siever, 1992), yet the Katherine ironstone lacks chert (like ironstones in general). Silica is less soluble under acidic conditions (Alexander et al., 1954), and acid weathering could have instead promoted the neoformation of clays (e.g., Equation 9). We suggest that the enhanced delivery of Al and other requisite geochemical inputs to coastal marine environments promoted Fe phyllosilicate authigenesis (e.g., Johnson et al., 2020a) rather than the precipitation of solid silica phases. The etched detrital quartz grains (Fig. 13) are evidence of diagenetic silica dissolution during diagenesis, likely due to complexation with organic acids produced by organic matter degradation which increases the solubility of silica in water (Bennett and Siegel, 1987).

Ferric iron in marine sediments can be reduced during organic matter oxidation (Berner, 1970), e.g.:

$$4Fe_2O_3 + CH_3COO^- + 7H_2O \rightarrow 8Fe^{2+} + 2HCO_3^- + 15OH^- \quad (15)$$

This dissimilatory iron reduction is mediated by bacteria (Lovley and Phillips, 1988; Canfield, 1989; Thamdrup, 2000) and is considered to be an ancient metabolism (Vargas et al., 1998). In modern environments, Fe-oxidising bacteria and Fe-reducing bacteria often work in tandem (Bruun et al., 2010; Roden et al., 2012). Given that the organic carbon contents of the Katherine ironstones are an order of magnitude lower than that of their host mudstones (despite evidence for lower clastic input), organic matter remineralisation rates were likely elevated during ironstone deposition. This may have been due to an Fe oxyhydroxide flux leading to enhanced dissimilatory Fe reduction (e.g., Aller et al., 1986; Taylor and Curtis, 1995), sediment regeneration during stratigraphic condensation leading to enhanced organic matter oxidation, or a combination of these factors. Local dissimilatory iron reduction could have provided Fe^{2+} and crucially raised pH, necessary for the formation of Fe(II) phyllosilicates (Fritz and Toth, 1997).

Fe(II) phyllosilicates such as berthierine are rarely found as synsedimentary to early diagenetic phases, and more commonly form as pore-lining cements in sandstones during burial diagenesis (Curtis, 1987b), as other phases typically take precedence during early diagenesis. For example, because dissimilatory iron reduction process produces Fe^{2+} and bicarbonate (Equation 15), this process can lead to siderite formation under reducing conditions:

$$Fe^{2+} + HCO^{3-} + OH^- \rightarrow FeCO_3 + H_2O \quad (16)$$

Siderite is only present in the Katherine ironstone in minor amounts, as is the case for many other ironstones (Castaño and Garrels, 1950; Schellmann, 1969; Bhattacharyya, 1983; Todd et al., 2019). If the availability of ferric minerals is not the limiting factor, dissimilatory iron reduction produces much more Fe^{2+} than bicarbonate (Equation 15), and in the presence of O_2, the formation of Fe(III) (oxyhydr)oxides and carbonic acid is favoured:

$$FeCO_3 + O_2 + 4H_2O \rightarrow 2Fe_2O_3 + 4H_2CO_3 \quad (17)$$

Any minor siderite could have also been transformed to Fe(III) (oxyhydr)oxides in the presence of humic acid (Xing et al., 2020), which may explain the lack of siderite in the Katherine ironstone.

The Katherine ironstone features minor authigenic phosphate minerals (Fig. 15), which are commonly documented in other oolitic ironstones (Maynard, 1986; Gehring, 1989; Kearsley, 1989; Pufahl et al., 2014; Todd et al., 2019; Johnson et al., 2020a; Rudmin et al., 2020). Apatite authigenesis typically occurs in modern marine sediments via organic matter remineralisation during early diagenesis (Sundby et al., 1992; Ruttenberg, 2003). As well as remineralising P from organophosphate compounds, dissimilatory Fe reduction releases P sorbed to Fe(III) (oxyhydr)oxides, which can also enrich the local waters in P (Curtis, 1987a), e.g.:

$$212Fe_2O_3 + (CH_2O)_{106}(NH_3)_{16}H_3PO_4 + 318H_2O \rightarrow 424Fe^{2+} + 106HCO_3^- + 16NH_3 + H_3PO_4 + 742OH^- \quad (18)$$

For the Katherine ironstone, P was most likely sourced from continental weathering. Lateritic weathering of minerals such as apatite and monazite releases P and REE and can lead to the formation of authigenic phosphates in close association with kaolinite (Banfield and Eggleton, 1989), including LREE-rich phosphates such as rhabdophane (Braun et al., 1990). This process leads to the adsorption of phosphate onto clays, which is subsequently released in nearshore marine environments upon mixing with the more alkaline and saline seawater (Hao et al., 2021). This process, followed by Fe and P cycling in the coastal sediments, could have led to the supersaturation and precipitation of monazite, rhabdophane, and francolite in the Katherine ironstone during early diagenesis. Alternatively (or in addition), authigenic phosphates formed in lateritic soil profiles and incorporated into kaolinite could have been transported to marine sediments, and during progressive diagenetic transformation of kaolinite these phosphates could be inherited by neoformed Fe phyllosilicate phases, as seen in modern shelf sediments experiencing glauconitisation (Bayon et al., 2023).

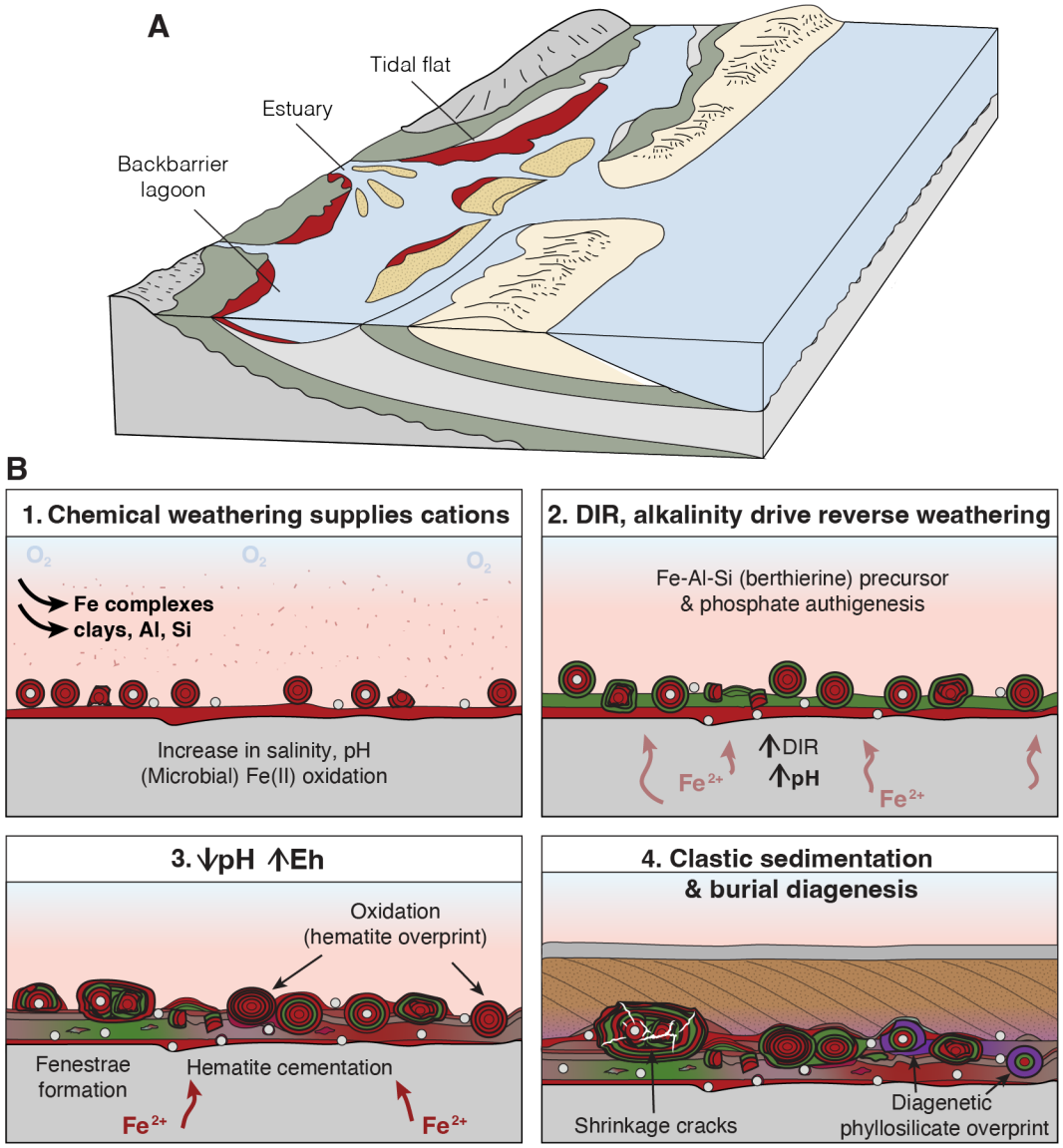

Fig. 21. A. Block model schematic for the range of depositional environments proposed for the Katherine ironstone (shown in red), and other similar ironstones globally (figure adapted from Reinson, 1979). **B.** Genetic model for ironstone deposition in low-energy, shallow marine environments. Chemical weathering can supply the requisite Fe (as Fe(III) aggregates, colloids and/or Fe(II) complexes under acidic conditions), as well as cation-poor clays, Al and Si compounds. Mixing with seawater leads to a flux of Fe(III) (oxyhydr)oxides to the seafloor. Subsequent dissimilatory iron reduction increases pH which drives the authigenesis of Fe phyllosilicate precursor phases (reverse weathering). Ironstone oncoids, pisoids and ooids form via the alternating precipitation of Fe(III) oxyhydroxides and Fe(II) phyllosilicate precursor gels under fluctuating redox conditions, with varying degrees of overprinting during diagenesis.

7.4 Ironstone genetic model

As discussed above, the Katherine ironstone was the product of intense iron cycling in coastal marine environments (Fig. 21A). The locus of deposition of the ironstone was spatially restricted and was likely controlled by the supply of cations from intense chemical weathering (Equations 8–9). This enhanced weathering may have been the result of tropical palaeogeography, as well as the long-term regressive trend leading to the development of a broad coastal plain. The ironstones were deposited as a hardground during relative stratigraphic condensation facilitated by minor transgression (e.g., Johnson et al., 2020a). River waters and groundwaters could have supplied Fe(III) as aggregates and organic colloids, as well as Fe(II) complexes under acidic conditions. This Fe flux would have been preferentially captured during estuarine mixing as a result of a pronounced gradient in pH and salinity (Krachler et al., 2010; Raiswell, 2011; Hao et al., 2021), as has been proposed for some other oolitic ironstone deposits (Pufahl et al., 2013; Novoselov et al., 2018; Sokol et al., 2020), with the oxidation of any Fe(II) likely facilitated by bacteria.

Collectively, this would have led to a flux of Fe(III) (oxyhydr)oxides and organic matter to the seafloor. Sediment regeneration during stratigraphic condensation would have promoted organic matter oxidation coupled to Fe(III) reduction, as evidenced by the low organic carbon contents of the ironstone compared to the host rocks. Dissimilatory iron reduction during early diagenesis would have further increased pH (Equation 15) which, combined with Al and Si compounds supplied from chemical weathering products, promoted Fe(II) phyllosilicate authigenesis (Equation 12). Fluctuation in pH and Eh in bottom waters and porewaters drove the alternating precipitation of Fe(III) (oxyhydr)oxides and berthierine precursor phases (Fig. 21B), while the remineralisation of organic- and Fe-bound phosphate led to the precipitation of minor authigenic phosphates. Frequent synsedimentary reworking led to the formation of composite iron ooids and oncoids at the sediment–seawater interface. Eventually, continued transgression shut off the requisite supply of continental solutes, and buried the ironstone precursor phases, leading to further diagenetic transformation (Fig. 21B).

This model invoking continental weathering and intense iron cycling in coastal marine environments is consistent with some models put forward for some other Precambrian ironstone deposits (Taylor, 1973; Dorland, 1999; Abbott and Sweet, 2000; Pufahl et al., 2013; Johnson et al., 2020a). Importantly, this model is distinct from those proposed for banded and granular iron formations (Konhauser et al., 2017). The elevated Al contents of ironstones compared to granular iron formations (Table 1) supports a stronger role of continental input in ironstone genesis. The abundance of chert in iron formations compared to ironstones (James, 1954; Kimberley, 1994; Klein, 2005) shows that while the sorption of seawater Si onto precipitating Fe (oxyhydr)oxides led to chert formation in more detritus-starved marine environments, Si was instead incorporated into Fe phyllosilicates in ironstone depositional settings. Chert in iron formations may also have been linked to hydrothermal Si supply, as evidenced by strong positive Eu anomalies (Planavsky et al., 2010a; Thurston et al., 2012). As such, given their distinct mineralogy, petrography, geochemistry, and depositional environment, oolitic ironstones and iron formations should be considered as a unique deposit types. Importantly, any genetic model for these deposits needs to be able to account for their unique spatiotemporal distribution in deep time (Fig. 1), and we re-evaluate the stratigraphic record of these deposits below.

7.5 Controls on ironstone spatiotemporal distribution

While non-oolitic, granular iron formations are found from the early Palaeoproterozoic, those with iron-coated grains are near-exclusively contemporaneous at ca. 1890 Ma (Fig. 1). These oolitic and cherty granular iron formations are predominantly found in the Lake Superior region and correlative basins in northern Laurentia, with a similar deposit in Western Australia (Frere Formation; Hall and Goode, 1978; Rasmussen et al., 2012) and possibly India (Chilpi Group; Mohanty and Mishra, 2022), and have been linked to enhanced hydrothermal Fe flux (e.g., Baragar, 1967; Fryer, 1977; Li et al., 2022; Zajac and Peter, 2022). By contrast, non-cherty, oolitic ironstones are found sporadically throughout the Proterozoic Eon (Fig. 1). While the temporal distribution of Phanerozoic ironstones has been linked to ocean anoxic events and upwelling ferruginous seawater (Van Houten and Arthur, 1989; Cotter and Link, 1993; McLaughlin et al., 2012; Bekker et al., 2014; Yan et al., 2015; Pufahl et al., 2020; Dunn et al., 2021; Matheson and Pufahl, 2021), the oceans were dominantly anoxic throughout the Proterozoic (Poulton and Canfield, 2011; Reinhard et al., 2013; Sperling et al., 2015). Proterozoic marine Fe concentrations may have been relatively low compared to the Archaean (Pufahl et al., 2013; Planavsky et al., 2018), and therefore hydrothermal pulses could have led to fluctuations in marine Fe (e.g., Song et al., 2017) and influenced Proterozoic ironstones (e.g., Lin et al., 2019; Zhu et al., 2022). However, hydrothermal Fe would have been more readily titrated by dissolved sulphate in the middle Proterozoic

(Kump and Seyfried, 2005), and ironstones are not associated with the numerous volcano-sedimentary successions that record episodes of active tectonism, volcanism and hydrothermalism throughout this time. Instead, temporal trends must have been controlled by continental weatherability, basin evolution, palaeogeography, and atmospheric conditions.

The evolving nature of weathering regimes would have exerted a dominant control on ironstone genesis. The oldest known example of iron-coated grains in the sedimentary record is found in the Mesoarchaean Nconga Formation (Mozaan Basin, South Africa; Fig. 1), which features chert granules coated with thin, concentric layers of magnetite (Smith et al., 2017; Smith et al., 2020). The chert-rich mineralogy, distinct texture, and lack of association with siliciclastic material (Smith et al., 2017) stand in contrast with typical oolitic ironstones, suggesting that this is a unique deposit. As such, we propose that noncherty, oolitic ironstones are absent from the Archaean, and that the oldest such example is the Siderian Timeball Hill Formation (Transvaal Basin, South Africa; Fig. 1) deposited during (or shortly following) the transition to an oxidising atmosphere (i.e., the Great Oxidation Event; Dorland, 1999; Warke et al., 2020; Poulton et al., 2021). There is evidence for continental emergence and large continental weathering fluxes dating back to at least the middle–late Archaean (Satkoski et al., 2016; Korenaga et al., 2017), and atmospheric CO_2 levels would have been significantly higher during this time (Kasting, 1993; Sheldon et al., 2021). Therefore, if the absence of Archean ironstones is not simply due to a lack of preservation, this would imply that the weathering regime of that time was incapable of producing these deposits, even though palaeosols from this time show evidence for Fe mobility during anoxic weathering (Babechuk et al., 2019; Heard et al., 2021). Indeed, while there are Neoarchaean iron formations deposited at the fluvial–marine interface (Fralick and Pufahl, 2006), these lack ooids or other ironstone features. This may be because pH during CO_2-driven weathering (the dominant mechanism in the Archaean; e.g., Sheldon, 2006) is buffered by the hydrolysis of aluminosilicates (Equations 8–10; Brady and Carroll, 1994). The deposition of the Timeball Hill ironstone has been linked to acid-rock drainage (Equation 6; Konhauser et al., 2011), which could have been an important Fe^{2+} supply to the oceans via acidic streams or groundwater from the early Proterozoic (Konhauser et al., 2011; Havig et al., 2017). Therefore, although some degree of pyrite oxidation may have been possible during the Archaean (e.g., Stüeken et al., 2012; Wu et al., 2023), the coincidence between the Timeball Hill and the Great Oxidation Event may imply that more extensive oxidative weathering of redox-sensitive, Fe-bearing minerals (such as pyrite, olivine and pyroxene) was a prerequisite for ironstone genesis. Alternatively, the coincidence with atmospheric oxygenation may implicate the onset of (sub)oxic Fe redox cycling in shallow waters.

By compiling ironstone occurrences throughout the remainder of the Proterozoic (Fig. 1) we show that these deposits appear to be grouped geographically, which implies a local control over ironstone deposition during the Proterozoic, such as regional climate or weatherability (e.g., relief or catchment lithology). Following the deposition of the Timeball Hill ironstone in the Siderian, there are two more South African ironstones deposited during the Rhyacian (Dwaal Heuvel, Strubenkop, Daspoort, and Silverton formations; Schweigart, 1965; Dorland, 1999). To our knowledge, the next oldest oolitic ironstone is found in the ca. 2050 Ma Kolasjoki Sedimentary Formation in the Kola Peninsula (Akhmedov, 1972). Following this, ironstone deposition shifts to Western Australia in the Orosirian (Chiall Formation; Pufahl et al., 2013); Statherian oolitic ironstones have been reported from North China (Chuanlinggou and Yunmengshan formations; Hou et al., 1983; Qiu et al., 2020) and India (Saha and Tripathy, 2012); followed by Northern Australia in the Calymmian–Ectasian (Mainoru, Corocoran, Wondoan Hill, Mullera and Sherwin formations; Harms, 1965; Abbott et al., 2001; Johnson, 2021); and finally to Laurentia (Katherine and Chuar groups, this study; Wang et al., 2022) during the Tonian Period. With the possible exception of the Kolasjoki Sedimentary Formation, for which the palaeolatitude is poorly resolved but may have been subtropical (Veselovskiy et al., 2017), all of the Proterozoic ironstones appear to have been deposited at tropical–equatorial latitudes (Beukes et al., 2002; Williams et al., 2004; Cai et al., 2020; Eyster et al., 2020; Kirscher et al., 2021), which may imply a climate control.

Because most (but not all) Phanerozoic ironstones are associated with greenhouse conditions (Van Houten and Bhattacharyya, 1982), ironstone genesis has been linked to climate, yet the causal mechanism is debated. Greenhouse eustatic sea level rise and associated stratigraphic condensation has been proposed (Van Houten and Arthur, 1989; Garzanti, 1993), but there was no glacial ice during the deposition of the Proterozoic ironstones (Young, 2013), with the possible of exception of the Timeball Hill and Chuar ironstones deposited on the eve of glaciation (Coetzee et al., 2006; MacLennan et al., 2020). Further, it is also difficult to apply models linking warm climate to marine anoxia (e.g., Banerjee et al., 2020; Dunn et al., 2021) to the predominantly anoxic oceans of the Proterozoic. The warm and humid conditions of tropical climates enhanced chemical weathering and mobilised Fe and Al (Pope, 2022), and we suggest that this was important in ironstone genesis. While lateritic weathering

has been previously linked to the formation of Phanerozoic ironstones (e.g., Adeleye, 1973; Hallam, 1985; Berendsen et al., 1992; Schwarz and Germann, 1993; Mücke, 2000; Zhao and Bi, 2000; Gharaie et al., 2004; Andreeva and Chatalov, 2011; Durbano et al., 2015; Yilmaz et al., 2015; Li et al., 2021), some key examples exist of ironstones deposited at high latitude (Van Houten and Arthur, 1989) or in temperate climates (Guerrak, 1991). If the apparent association with tropical latitudes in the Proterozoic is robust, then perhaps this dependency was broken by the greater oxidising power of the Phanerozoic atmosphere (Bayon et al., 2022), or the expansion of land plants (e.g., Algeo and Scheckler, 1998).

Biological processes exert an important influence on continental weathering processes and the flux of metals to the oceans. Organic acids can intensify silicate weathering and cation solubilisation (Drever and Stillings, 1997), although limited by clay neoformation in soils (Lawrence et al., 2014). Iron-binding ligands (such as siderophores, organic acids and extracellular polymeric substances) can help to keep Fe in solution during transport (e.g., Hunter and Boyd, 2007), and organic matter complexes (such as humic or fulvic acids) also play a major role in stabilising colloidal Fe in suspension (e.g., Sholkovitz, 1976). Salinity-driven flocculation and scavenging of these complexes captures Fe in modern coastal environments (Krachler et al., 2010; Raiswell, 2011). Purucker (1984) proposed that the first appearance of widespread oolitic ironstone in the stratigraphic record (then suggested to be the middle Cambrian Period) could have been related to the expansion of the terrestrial biosphere and a concomitant increase in continental weatherability. Although land plants did not evolve until the Palaeozoic (Donoghue et al., 2021), the Precambrian likely hosted an extensive terrestrial microbial biosphere (Lalonde and Konhauser, 2015; Finke et al., 2019), and there is palaeosol evidence for organic acid weathering dating back to the Mesoarchaean (Rye and Holland, 2000; Beaty and Planavsky, 2021). Therefore, organic weathering and transport likely contributed to the Proterozoic cation flux, and this may have influenced the temporal variation of ironstones. Specifically, coastal wetlands (such as swamps, marshes and floodplains) are highly productive and dominantly anoxic because of permanent water saturation (Mitsch et al., 2013), and these settings could have led to the leaching of abundant Fe (Krachler et al., 2010; Sanders et al., 2015). The proliferation of land plants in the Phanerozoic may, at least in part, explain the more widespread and frequent episodes of ironstone deposition during this time.

Finally, the tectonic setting and basin evolution appear to be significant. The Mackenzie Mountains Supergroup is considered to have been deposited in a series of intra-continental (epeiric) basins (Rainbird et al., 1996; Macdonald et al., 2012). Proterozoic oolitic ironstones in general are largely interpreted to have been deposited in intracratonic basins, foreland basins, or interior seaways, such as those of the Pretoria (Transvaal Basin, South Africa; Eriksson and Reczko, 1998; Eriksson et al., 2002), Vindeggen (Rjukan Rift Basin, Norway; Köykkä and Lamminen, 2011), Roper (McArthur Basin, northern Australia; Abbott and Sweet, 2000) and Chuar (Galeros Formation, Grand Canyon, USA; Dehler et al., 2017) groups (Fig. 1). Intra-continental marine basins are characterised by low-gradient shelves which dampens wave energy, promoting the development and preservation of tide-dominated environments (e.g., Sarkar et al., 2004). Because much of the Proterozoic sedimentary record is preserved in these types of basins (Bose et al., 2012), this may merely be a preservational bias. However, many Phanerozoic ironstones also share a similar intra-continental setting (Knox, 1970; Van Houten and Karasek, 1981; Van Houten and Arthur, 1989; Gorter, 1991; Chan, 1992; Cotter and Link, 1993; Taylor et al., 2002), and those that have been interpreted to have been deposited in shelf settings are often found in narrow seaways such as the Ordovician Rheic Ocean (Todd et al., 2019; Pufahl et al., 2020; Dunn et al., 2021) and the Cretaceous Western Interior Seaway (Chan, 1992; Taylor et al., 2002). The development of choked coastal lagoons (those with restricted water exchange through a narrow entrance channel) facilitates water stratification, strong gradients and temporal fluctuations in physico-chemical conditions, and trapping materials supplied by rivers and marine upwelling (Kjerfve and Magill, 1989; Roselli et al., 2013), all of which may promote ironstone genesis. The geomorphologically ephemeral nature of these settings (Kjerfve and Magill, 1989) may explain their distribution in the stratigraphic record. Further, the stable nature of the tectonic setting of many of these Proterozoic ironstones may have been important, and Phanerozoic ironstones have also been noted to be associated with anorogenic basins (Guerrak, 1991; Petránek and Van Houten, 1997). Tectonic quiescence may have been important in maintaining relatively low uplift and denudation rates required for intense chemical weathering (Ameijeiras-Mariño et al., 2017), shifting the balance towards incongruent weathering and promoting ironstone genesis.

Further work is needed to elucidate the relative importance of tectonic setting versus weathering controls on ironstone deposition. This re-evaluation of the spatiotemporal distribution of oolitic ironstones shows that ironstones were deposited in every Proterozoic period except for the Stenian, Cryogenian and Ediacaran (Fig. 1). The reasons for the lack of ironstone deposition during those periods, alongside the dearth of ironstones from the Carboniferous, Permian, Triassic and

modern records (Petránek and Van Houten, 1997), continue to be enigmatic. Regardless, we suggest that consideration of the distribution of ironstones in the Precambrian and Phanerozoic is crucial to presenting a holistic genetic model.

8. Conclusions

The middle Tonian Katherine Group of the Wernecke Inlier (Yukon) includes well-preserved oolitic ironstone, which represents a rare example of this type of deposit from the Precambrian. The implications of younger ironstones for understanding the Phanerozoic world remain controversial, and the Katherine Group presents an important opportunity to re-evaluate ironstone genetic models in light of their applicability to the Precambrian. Here we compare Precambrian oolitic ironstones to iron formations and their Phanerozoic equivalents to explore their implications for understanding environmental change in deep time.

The Katherine ironstone contains abundant coated grains (iron ooids and oncoids) composed of interlaminated hematite and berthierine. Textural evidence indicates that these coated grains formed on the seafloor (rather than precipitating as in-situ concretions) and experienced extensive sedimentary reworking. Ironstone horizons occur in the transition from the tidal flat environments of the McClure Formation to the tide-influenced estuary setting of the Abraham Plains Formation. The overall stratigraphic context of the Mackenzie Mountains Supergroup suggests that the ironstones were deposited toward the end of a first-order regressive sequence, during the onset of a transgressive phase which facilitated stratigraphic condensation and the development of protected, low-energy marine conditions. Given the tropical latitude (Denyszyn et al., 2009; Merdith et al., 2017), the high Chemical Index of Alteration values of the host shales (Figs. 17–18), we suggest that the drainage basin experienced extensive weathering. A continental Fe source is supported by the lenticular nature of the deposit, as well as the radiogenic Nd isotope composition and lack of positive Eu anomalies.

We present a model whereby this continental input supplied the requisite flux of Fe (as well as Al, Si, and P) for ironstone genesis. Iron could have been transported in rivers and groundwaters either in solution (under anoxic or acidic conditions, or stabilised by organic ligands) or in suspension (as organometallic colloids), and this Fe would have been effectively removed upon mixing with seawater due to increased salinity and pH. This flux of highly reactive Fe to estuarine environments would have facilitated vigorous Fe cycling, likely mediated by bacteria, resulting in a flux of Fe(III) (oxyhydr)oxides and organic matter to the seafloor. Increased pH of the local waters, as well as Al and Si compounds supplied by intense chemical weathering, promoted Fe phyllosilicate authigenesis (i.e., reverse weathering). Reworking and sediment regeneration sustained these processes and maintained the dominance of Fe reduction over sulphate reduction (Aller et al., 1986). This interplay between chemical processes and dynamic hydrological conditions led to fluctuations of pH–Eh and the alternating precipitation of hematite and berthierine precursor phases as iron ooids and oncoids. Concomitant remineralisation of P compounds drove the precipitation of authigenic phosphates (i.e., sink switching). Ironstone deposition eventually ceased due to transgression, which cut off the continental solute supply. As such, the ironstone records several important biogeochemical processes.

This model is consistent with the distribution of ironstones as lenticular marker horizons in the geological record, which suggests that their deposition requires a confluence of several important environmental factors (Petránek and Van Houten, 1997). A critical review of available literature data shows that oolitic ironstones contrast with other deposits such as cherty, granular iron formations (which may also feature iron ooids; Table 1), and that similar oolitic ironstones can be found throughout the Proterozoic stratigraphic record (Fig. 1). The genetic model presented here shares similarities with those for similar deposits from the Proterozoic (Abbott and Sweet, 2000; Pufahl et al., 2013; Johnson et al., 2020a). Because this ironstone genetic model invokes a predominantly continental Fe source, ironstones do not necessarily reflect global ocean chemistry, although they are strongly influenced by atmospheric conditions (c.f. Zhang et al., 2021). The restriction of Proterozoic ironstones to coastal marine settings and the cessation of widespread iron formation deposition during the Palaeoproterozoic may be consistent with models for low Fe^{2+} oceans during the middle Proterozoic (Pufahl et al., 2013). The temporal distribution of ironstones is likely controlled by a number of Earth's surface processes, that play an integral role in major global biogeochemical cycles, including continental weathering, microbial iron oxidation, dissimilatory iron reduction, reverse weathering, and phosphate remineralisation and authigenesis. As such, the extension of the record of "Phanerozoic-style" oolitic ironstones back into the Precambrian provides a critical archive of these processes that can be used to better understand tectonic evolution, climate, and the evolving chemistry of the ocean–atmosphere system in deep time.

Funding
This work was supported by funding from the Fonds de Recherche du Québec – Nature et Technologies (FRQNT) to M.A.L., and from Natural Sciences and Engineering Research Council of Canada, Natural Resources Canada (Polar Continental Shelf Program), and the Agouron Institute to G.P.H. A.H. acknowledges funding from an ARC DECRA DE190100988; and M.W., G.H. and A.H. were also funded by ARC DP210103715. C.L.W. acknowledges funding from the Strategy Priority Research Program (Category B) of the Chinese Academy of Sciences (No. XDB0710000), the Key Research Program of the Institute of Geology and Geophysics, Chinese Academy of Sciences (grant IGGCAS-201905 and IGGCAS-202204), and Youth Innovation Promotion Association, Chinese Academy of Sciences.

Data availability
This work includes a review of previously published geochemical data from sedimentary iron deposits. All new data is included in the manuscript and supplementary data tables.

Acknowledgements
The authors thank Graham Hutchison for assistance with electron microprobe and scanning electron microscopy work, Alan Grieg for laser ablation analyses, and Allan Pring for assistance with X-ray diffraction and insights into clay mineral identification. We thank the Yukon Geological Survey, Tyler Ambrose, and Justin Emberley for help with field logistics, and Kelsey Lamothe for field assistance. This manuscript benefitted from discussions with Noah Planavsky, Kurt Konhauser, Brennan O'Connell and Rob Rainbird. We thank Edward Matheson and Michael Babechuk for thorough and constructive reviews of the original draft, which greatly improved the manuscript, as well as Christopher Fielding for editorial handling.

References
Abbott, G., 1997, Geology of the upper Hart River area, eastern Ogilvie Mountains, Yukon Territory (116A/10,116 A/11). Indian and Northern Affairs Canada, Exploration and Geological Services Division, Yukon Region: Bulletin, v. 9, p. 92.

Abbott, S., and Sweet, I., 2000, Tectonic control on third-order sequences in a siliciclastic ramp-style basin: An example from the Roper Superbasin (Mesoproterozoic), northern Australia: Australian Journal of Earth Sciences, v. 47, no. 3, p. 637-657.

Abbott, S., Sweet, I., Plumb, K., Young, D., Cutovinos, A., Ferenczi, P., Brakel, A., and Pietsch, B., 2001, Roper Region: Urapunga - Roper River, Northern Territory : combined explanatory notes: Northern Territory Geological Survey.

Abram, M. B., and Holz, M., 2020, Early to Middle Devonian ironstone and phosphorite in the northwestern Gondwana Parnaíba Basin, Brazil: A record of an epeiric margin paleoceanographic changes: Sedimentary Geology, v. 402, p. 105646.

Adeleye, D., 1973, Origin of ironstones, an example from the middle Niger Valley, Nigeria: Journal of Sedimentary Research, v. 43, no. 3, p. 709-727.

Afroz, M., Fralick, P., and Lalonde, S., 2023, Sedimentology and geochemistry of basinal lithofacies in the Mesoarchean (2.93 Ga) Red Lake carbonate platform, northwest Ontario, Canada: Precambrian Research, v. 388, p. 106996.

Aitken, J., 1981, Stratigraphy and sedimentology of the Upper Proterozoic Little Dal Group, Mackenzie Mountains, Northwest Territories: Proterozoic basins of Canada: Geological Survey of Canada Paper, v. 81, no. 10, p. 47-71.

Aitken, J., Long, D., and Semikhatov, M., 1978a, Correlation of Helikian strata, Mackenzie Mountains-Brock Inlier-Victoria Island: Current research, part A. Geological Survey of Canada, Paper, v. 78, p. 485-486.

Aitken, J., Long, D., and Semikhatov, M., 1978b, Progress in Helikian stratigraphy, Mackenzie Mountains: Current research, part A. Geological Survey of Canada, Paper, v. 78, p. 481-484.

Akhmedov, A., 1972, Hematite oolites in sedimentary rocks of the Pechenga Complex: Materials on mineralogy of the Kola Peninsula: Nauka, v. 9, p. 135-137.

Akin, S. J., Pufahl, P. K., Hiatt, E. E., and Pirajno, F., 2013, Oxygenation of shallow marine environments and chemical sedimentation in Palaeoproterozoic peritidal settings: Frere Formation, Western Australia: Sedimentology, v. 60, no. 7, p. 1559-1582.

Alexander, B. W., Bau, M., and Andersson, P., 2009, Neodymium isotopes in Archean seawater and implications for the marine Nd cycle in Earth's early oceans: Earth and Planetary Science Letters, v. 283, no. 1-4, p. 144-155.

Alexander, G. B., Heston, W., and Iler, R. K., 1954, The solubility of amorphous silica in water: The Journal of Physical Chemistry, v. 58, no. 6, p. 453-455.

Algeo, T. J., and Scheckler, S. E., 1998, Terrestrial-marine teleconnections in the Devonian: links between the evolution of land plants, weathering processes, and marine anoxic events: Philosophical Transactions of the Royal Society of London. Series B: Biological Sciences, v. 353, no. 1365, p. 113-130.
Allen, G. P., and Posamentier, H. W., 1993, Sequence stratigraphy and facies model of an incised valley fill; the Gironde Estuary, France: Journal of Sedimentary Research, v. 63, no. 3, p. 378-391.
Allen, J., 1980, Sand waves: a model of origin and internal structure: Sedimentary Geology, v. 26, no. 4, p. 281-328.
Aller, R., Mackin, J., and Cox Jr, R., 1986, Diagenesis of Fe and S in Amazon inner shelf muds: apparent dominance of Fe reduction and implications for the genesis of ironstones: Continental Shelf Research, v. 6, no. 1-2, p. 263-289.
Aller, R. C., and Rude, P. D., 1988, Complete oxidation of solid phase sulfides by manganese and bacteria in anoxic marine sediments: Geochimica et Cosmochimica Acta, v. 52, no. 3, p. 751-765.
Ameijeiras-Mariño, Y., Opfergelt, S., Schoonejans, J., Vanacker, V., Sonnet, P., De Jong, J., and Delmelle, P., 2017, Impact of low denudation rates on soil chemical weathering intensity: A multiproxy approach: Chemical Geology, v. 456, p. 72-84.
Andreeva, P., and Chatalov, A., 2011, Origin of the Eifelian Ironstones from Well R-119 Kardam, Northeastern Bulgaria: Comptes rendus de l'Académie bulgare des Sciences, v. 64, no. 1.
Anthony, E. J., Gardel, A., Gratiot, N., Proisy, C., Allison, M. A., Dolique, F., and Fromard, F., 2010, The Amazon-influenced muddy coast of South America: A review of mud-bank–shoreline interactions: Earth-Science Reviews, v. 103, no. 3-4, p. 99-121.
Ashley, G. M., 1990, Classification of large-scale subaqueous bedforms; a new look at an old problem: Journal of Sedimentary Research, v. 60, no. 1, p. 160-172.
Assereto, R. L., and Kendall, C. G., 1977, Nature, origin and classification of peritidal tepee structures and related breccias: Sedimentology, v. 24, no. 2, p. 153-210.
Babechuk, M. G., and Fedo, C. M., 2022, Analysis of chemical weathering trends across three compositional dimensions: applications to modern and ancient mafic-rock weathering profiles: Canadian Journal of Earth Sciences, v. 60, no. 7, p. 839-864.
Babechuk, M. G., Weimar, N. E., Kleinhanns, I. C., Eroglu, S., Swanner, E. D., Kenny, G. G., Kamber, B. S., and Schoenberg, R., 2019, Pervasively anoxic surface conditions at the onset of the Great Oxidation Event: New multi-proxy constraints from the Cooper Lake paleosol: Precambrian Research, v. 323, p. 126-163.
Bailey, S., 1988, Odinite, a new dioctahedral-trioctahedral Fe 3+-rich 1: 1 clay mineral: Clay minerals, v. 23, no. 3, p. 237-247.
Baioumy, H., Omran, M., and Fabritius, T., 2017, Mineralogy, geochemistry and the origin of high-phosphorus oolitic iron ores of Aswan, Egypt: Ore Geology Reviews, v. 80, p. 185-199.
Banerjee, S., Choudhury, T. R., Saraswati, P. K., and Khanolkar, S., 2020, The formation of authigenic deposits during Paleogene warm climatic intervals: a review: Journal of Palaeogeography, v. 9, no. 1, p. 1-27.
Banfield, J. F., and Eggleton, R. A., 1989, Apatite replacement and rare earth mobilization, fractionation, and fixation during weathering: Clays and Clay Minerals, v. 37, p. 113-127.
Bansal, U., Banerjee, S., Chauhan, G., Rudmin, M., Borgohain, D., and Upadhyay, A., 2021, Geochemistry of Callovian Ironstone in Kutch and Its Stratigraphic Implications, Mesozoic Stratigraphy of India, Springer, p. 215-239.
Baragar, W. R. A., 1967, Wakuach Lake Map-area Quebec-Labrador (23 0), Queen's Printer.
Barnard, P. L., Hanes, D. M., Rubin, D. M., and Kvitek, R. G., 2006, Giant sand waves at the mouth of San Francisco Bay: Eos, Transactions American Geophysical Union, v. 87, no. 29, p. 285-289.
Barrett, T. J., Fralick, P. W., and Jarvis, I., 1988, Rare-earth-element geochemistry of some Archean iron formations north of Lake Superior, Ontario: Canadian Journal of Earth Sciences, v. 25, no. 4, p. 570-580.
Basta, F. F., Maurice, A. E., Fontboté, L., and Favarger, P.-Y., 2011, Petrology and geochemistry of the banded iron formation (BIF) of Wadi Karim and Um Anab, Eastern Desert, Egypt: implications for the origin of Neoproterozoic BIF: Precambrian Research, v. 187, no. 3, p. 277-292.
Bau, M., 1991, Rare-earth element mobility during hydrothermal and metamorphic fluid-rock interaction and the significance of the oxidation state of europium: Chemical Geology, v. 93, no. 3, p. 219-230.
Bau, M., and Dulski, P., 1996, Distribution of yttrium and rare-earth elements in the Penge and Kuruman iron-formations, Transvaal Supergroup, South Africa: Precambrian Research, v. 79, no. 1, p. 37-55.
Bau, M., and Dulski, P., 1999, Comparing yttrium and rare earths in hydrothermal fluids from the Mid-Atlantic Ridge: implications for Y and REE behaviour during near-vent mixing and for the Y/Ho ratio of Proterozoic seawater: Chemical Geology, v. 155, no. 1, p. 77-90.
Bau, M., Schmidt, K., Koschinsky, A., Hein, J., Kuhn, T., and Usui, A., 2014, Discriminating between different genetic types of marine ferro-manganese crusts and nodules based on rare earth elements and yttrium: Chemical Geology, v. 381, p. 1-9.
Baumgartner, J., and Faivre, D., 2015, Iron solubility, colloids and their impact on iron (oxyhydr) oxide formation from solution: Earth-Science Reviews, v. 150, p. 520-530.
Bayer, U., 1989, Stratigraphic and environmental patterns of ironstone deposits: Geological Society, London, Special Publications, v. 46, no. 1, p. 105-117.
Bayon, G., Bindeman, I. N., Trinquier, A., Retallack, G. J., and Bekker, A., 2022, Long-term evolution of terrestrial weathering and its link to Earth's oxygenation: Earth and Planetary Science Letters, v. 584, p. 117490.

Bayon, G., Giresse, P., Chen, H., Rouget, M., Gueguen, B., Moizinho, G., Barrat, J.-A., and Beaufort, D., 2023, The Behavior of Rare Earth Elements during Green Clay Authigenesis on the Congo Continental Shelf: Minerals, v. 13.
Beaty, B. J., and Planavsky, N. J., 2021, A 3 by record of a biotic influence on terrestrial weathering: Geology, v. 49, no. 4, p. 407-411.
Bekker, A., Planavsky, N., Rasmussen, B., Krapez, B., Hofmann, A., Slack, J., Rouxel, O., and Konhauser, K., 2014, Iron formations: Their origins and implications for ancient seawater chemistry, Treatise on geochemistry, Volume 12, Elsevier, p. 561-628.
Bekker, A., Slack, J. F., Planavsky, N., Krapež, B., Hofmann, A., Konhauser, K. O., and Rouxel, O. J., 2010, Iron formation: the sedimentary product of a complex interplay among mantle, tectonic, oceanic, and biospheric processes: Economic Geology, v. 105, no. 3, p. 467-508.
Bennett, P., and Siegel, D., 1987, Increased solubility of quartz in water due to complexing by organic compounds: Nature, v. 326, no. 6114, p. 684-686.
Berendsen, P., Doveton, J. H., and Speczik, S., 1992, Distribution and characteristics of a Middle Ordovician oolitic ironstone in northeastern Kansas based on petrographic and petrophysical properties: a Laurasian ironstone case study: Sedimentary geology, v. 76, no. 3-4, p. 207-219.
Berner, R. A., 1970, Sedimentary pyrite formation: American journal of science, v. 268, no. 1, p. 1-23.
Beukes, N., 1980, Suggestions towards a classification of and nomenclature for iron-formation: South African Journal of Geology, v. 83, no. 2, p. 285-290.
Beukes, N., 1983, Palaeoenvironmental setting of iron-formations in the depositional basin of the Transvaal Supergroup, South Africa: Developments in Precambrian Geology, v. 6, p. 131-198.
Beukes, N., and Klein, C., 1992, Models for iron-formation deposition: The Proterozoic biosphere: a multidisciplinary study, p. 147-156.
Beukes, N. J., Dorland, H., Gutzmer, J., Nedachi, M., and Ohmoto, H., 2002, Tropical laterites, life on land, and the history of atmospheric oxygen in the Paleoproterozoic: Geology, v. 30, no. 6, p. 491-494.
Beukes, N. J., and Klein, C., 1990, Geochemistry and sedimentology of a facies transition—from microbanded to granular iron-formation—in the early Proterozoic Transvaal Supergroup, South Africa: Precambrian Research, v. 47, no. 1-2, p. 99-139.
Bhattacharyya, D. P., 1983, Origin of berthierine in ironstones: Clays and clay minerals, v. 31, no. 3, p. 173-182.
Bhattacharyya, D. P., and Kakimoto, P. K., 1982, Origin of ferriferous ooids; an SEM study of ironstone ooids and bauxite pisoids: Journal of Sedimentary Research, v. 52, no. 3, p. 849-857.
Bjerrum, C. J., and Canfield, D. E., 2002, Ocean productivity before about 1.9 Gyr ago limited by phosphorus adsorption onto iron oxides: Nature, v. 417, no. 6885, p. 159.
Bose, P. K., and Chakraborty, P. P., 1994, Marine to fluvial transition: proterozoic upper Rewa sandstone, Maihar, India: Sedimentary Geology, v. 89, no. 3-4, p. 285-302.
Bose, P. K., Eriksson, P. G., Sarkar, S., Wright, D., Samanta, P., Mukhopadhyay, S., Mandal, S., Banerjee, S., and Altermann, W., 2012, Sedimentation patterns during the Precambrian: A unique record?: Marine and Petroleum Geology, v. 33, no. 1, p. 34-68.
Boyd, P. W., and Ellwood, M. J., 2010, The biogeochemical cycle of iron in the ocean: Nature Geoscience, v. 3, no. 10, p. 675-682.
Brady, P. V., and Carroll, S. A., 1994, Direct effects of CO2 and temperature on silicate weathering: Possible implications for climate control: Geochimica et Cosmochimica Acta, v. 58, no. 7, p. 1853-1856.
Braun, J.-J., Pagel, M., Muller, J.-P., Bilong, P., Michard, A., and Guillet, B., 1990, Cerium anomalies in lateritic profiles: Geochimica et Cosmochimica Acta, v. 54, no. 3, p. 781-795.
Brigatti, M. F., Galan, E., and Theng, B., 2013, Structure and mineralogy of clay minerals, Developments in clay science, Volume 5, Elsevier, p. 21-81.
Bruun, A.-M., Finster, K., Gunnlaugsson, H. P., N∅ rnberg, P., and Friedrich, M. W., 2010, A comprehensive investigation on iron cycling in a freshwater seep including microscopy, cultivation and molecular community analysis: Geomicrobiology Journal, v. 27, no. 1, p. 15-34.
Bryce, C., Blackwell, N., Schmidt, C., Otte, J., Huang, Y. M., Kleindienst, S., Tomaszewski, E., Schad, M., Warter, V., and Peng, C., 2018, Microbial anaerobic Fe (II) oxidation–Ecology, mechanisms and environmental implications: Environmental microbiology, v. 20, no. 10, p. 3462-3483.
Burkhalter, R. M., 1995, Ooidal ironstones and ferruginous microbialites: origin and relation to sequence stratigraphy (Aalenian and Bajocian, Swiss Jura mountains): Sedimentology, v. 42, no. 1, p. 57-74.
Burton, J., Krinsley, D., and Pye, K., 1987, Authigenesis of kaolinite and chlorite in Texas Gulf Coast sediments: Clays and Clay Minerals, v. 35, no. 4, p. 291-296.
Cai, Y., Pei, J., Zhang, S.-H., Tong, Y., Yang, Z., and Zhao, Y., 2020, New paleomagnetic results from the ca. 1.68–1.63 Ga mafic dyke swarms in Western Shandong Province, Eastern China: implications for the reconstruction of the Columbia supercontinent: Precambrian Research, v. 337, p. 105531.
Calvert, S., and Pedersen, T., 1996, Sedimentary geochemistry of manganese; implications for the environment of formation of manganiferous black shales: Economic Geology, v. 91, no. 1, p. 36-47.
Canfield, D. E., 1989, Reactive iron in marine sediments: Geochimica et Cosmochimica Acta, v. 53, no. 3, p. 619-632.
Carbone, C. A., Narbonne, G. M., Macdonald, F. A., and Boag, T. H., 2015, New Ediacaran fossils from the uppermost Blueflower Formation, northwest Canada: disentangling biostratigraphy and paleoecology: Journal of Paleontology, v. 89, no. 2, p. 281-291.

Carlson, L., and Schwertmann, U., 1980, Natural occurrence of feroxyhite (δ′-FeOOH): Clays and Clay Minerals, v. 28, no. 4, p. 272-280.
Carozzi, A. V., 1961, Distorted oolites and pseudoolites: Journal of Sedimentary Research, v. 31, no. 2, p. 262-274.
Castaño, J. R., and Garrels, R. M., 1950, Experiments on the deposition of iron with special reference to the Clinton iron ore deposits: Economic Geology, v. 45, no. 8, p. 755-770.
Catt, J., Gad, M., Le Riche, H., and Lord, A., 1971, Geochemistry, micropalaeontology and origin of the middle Lias ironstones in northeast Yorkshire (Great Britain): Chemical Geology, v. 8, no. 1, p. 61-76.
Cayeux, L., 1922, Les minerals defer oolithiques de France, Fascicule II, Minerals de fer secondaires. Memoir Explicative de la Carte ….
Chan, M. A., 1992, Oolitic ironstone of the Cretaceous Western Interior seaway, east-central Utah: Journal of Sedimentary Research, v. 62, no. 4, p. 693-705.
Charette, M. A., and Sholkovitz, E. R., 2002, Oxidative precipitation of groundwater-derived ferrous iron in the subterranean estuary of a coastal bay: Geophysical research letters, v. 29, no. 10, p. 85-81-85-84.
Chauvel, J.-J., and Guerrak, S., 1989, Oolitization processes in Palaeozoic ironstones of France, Algeria and Libya: Geological Society, London, Special Publications, v. 46, no. 1, p. 165-173.
Chen, X., Li, M., Sperling, E. A., Zhang, T., Zong, K., Liu, Y., and Shen, Y., 2020, Mesoproterozoic paleo-redox changes during 1500–1400 Ma in the Yanshan Basin, North China: Precambrian Research, v. 347, p. 105835.
Chowns, T. M., 1968, Environmental and diagenetic studies of the Cleveland ironstone formation of north east Yorkshire: Newcastle University.
Clarke, W. A., Konhauser, K. O., Thomas, J. C., and Bottrell, S. H., 1997, Ferric hydroxide and ferric hydroxysulfate precipitation by bacteria in an acid mine drainage lagoon: FEMS Microbiology Reviews, v. 20, no. 3-4, p. 351-361.
Clement, A. M., Tackett, L. S., Ritterbush, K. A., and Ibarra, Y., 2020, Formation and stratigraphic facies distribution of early Jurassic iron oolite deposits from west central Nevada, USA: Sedimentary Geology, v. 395, p. 105537.
Clifton, H. E., 2006, A reexamination of facies models for clastic shorelines.
Cloud, P., 1973, Paleoecological significance of the banded iron-formation: Economic Geology, v. 68, no. 7, p. 1135-1143.
Coetzee, L., Beukes, N., Gutzmer, J., and Kakegawa, T., 2006, Links of organic carbon cycling and burial to depositional depth gradients and establishment of a snowball Earth at 2.3 Ga. Evidence from the Timeball Hill Formation, Transvaal Supergroup, South Africa: South African Journal of Geology, v. 109, no. 1-2, p. 109-122.
Cohen, P. A., Irvine, S. W., and Strauss, J. V., 2017a, Vase-shaped microfossils from the Tonian Callison Lake Formation of Yukon, Canada: taxonomy, taphonomy and stratigraphic palaeobiology: Palaeontology, v. 60, no. 5, p. 683-701.
Cohen, P. A., Strauss, J. V., Rooney, A. D., Sharma, M., and Tosca, N., 2017b, Controlled hydroxyapatite biomineralization in an~ 810 million-year-old unicellular eukaryote: Science Advances, v. 3, no. 6, p. e1700095.
Collin, P., Loreau, J., and Courville, P., 2005, Depositional environments and iron ooid formation in condensed sections (Callovian–Oxfordian, south-eastern Paris basin, France): Sedimentology, v. 52, no. 5, p. 969-985.
Colpron, M., Israel, S., Murphy, D., Pigage, L., and Moynihan, D., 2016, Yukon Bedrock Geology Map, 1:1,000,000 scale map and legend: Yukon Geological Survey, v. Open File 2016-1.
Cotter, E., 1977, The evolution of fluvial style, with special reference to the central Appalachian Paleozoic.
Cotter, E., and Link, J. E., 1993, Deposition and diagenesis of Clinton ironstones (Silurian) in the Appalachian Foreland Basin of Pennsylvania: Geological Society of America Bulletin, v. 105, no. 7, p. 911-922.
Cox, G. M., Halverson, G. P., Minarik, W. G., Le Heron, D. P., Macdonald, F. A., Bellefroid, E. J., and Strauss, J. V., 2013, Neoproterozoic iron formation: An evaluation of its temporal, environmental and tectonic significance: Chemical Geology, v. 362, p. 232-249.
Cox, G. M., Halverson, G. P., Poirier, A., Le Heron, D., Strauss, J. V., and Stevenson, R., 2016a, A model for Cryogenian iron formation: Earth and Planetary Science Letters, v. 433, p. 280-292.
Cox, G. M., Halverson, G. P., Stevenson, R. K., Vokaty, M., Poirier, A., Kunzmann, M., Li, Z.-X., Denyszyn, S. W., Strauss, J. V., and Macdonald, F. A., 2016b, Continental flood basalt weathering as a trigger for Neoproterozoic Snowball Earth: Earth and Planetary Science Letters, v. 446, p. 89-99.
Cranfield, L., Carmichael, D., and Wells, A., 1994, Ferruginous oolite and associated lithofacies from the Clarence-Moreton and related basins in southeast Queensland: Geology and petroleum potential of the Clarence-Moreton basin, New South Wales and Queensland, v. 241, p. 144-163.
Curtis, C., 1987a, Données récentes sur les réactions entre matières organiques et substances minérales dans les sédiments et sur leurs conséquences minéralogiques: Mémoires de la Société géologique de France (1924), no. 151, p. 127-141.
Curtis, C., 1987b, Mineralogical consequences of organic matter degradation in sediments: inorganic/organic diagenesis, Marine clastic sedimentology, Springer, p. 108-123.
Curtis, C., and Spears, D., 1968, The formation of sedimentary iron minerals: Economic Geology, v. 63, no. 3, p. 257-270.
Dabous, A. A., 2002, Uranium isotopic evidence for the origin of the Bahariya iron deposits, Egypt: Ore Geology Reviews, v. 19, no. 3-4, p. 165-186.

Dahanayake, K., and Krumbein, W. E., 1986, Microbial structures in oolitic iron formations: Mineralium Deposita, v. 21, no. 2, p. 85-94.
Dalrymple, R. W., and Choi, K., 2007, Morphologic and facies trends through the fluvial–marine transition in tide-dominated depositional systems: a schematic framework for environmental and sequence-stratigraphic interpretation: Earth-Science Reviews, v. 81, no. 3-4, p. 135-174.
Dalrymple, R. W., Knight, R. J., and Lambiase, J. J., 1978, Bedforms and their hydraulic stability relationships in a tidal environment, Bay of Fundy, Canada: Nature, v. 275, no. 5676, p. 100-104.
Dalrymple, R. W., Mackay, D. A., Ichaso, A. A., and Choi, K. S., 2012, Processes, morphodynamics, and facies of tide-dominated estuaries, Principles of tidal sedimentology, Springer, p. 79-107.
Dalrymple, R. W., and Rhodes, R. N., 1995, Estuarine dunes and bars, Developments in sedimentology, Volume 53, Elsevier, p. 359-422.
Dalrymple, R. W., and Rivers, J. M., 2023, A new look at modern carbonate shoals and coastal barrier systems: Earth-Science Reviews, p. 104553.
Danielson, A., Möller, P., and Dulski, P., 1992, The europium anomalies in banded iron formations and the thermal history of the oceanic crust: Chemical Geology, v. 97, no. 1, p. 89-100.
Dashtgard, S. E., Gingras, M. K., and MacEachern, J. A., 2009, Tidally modulated shorefaces: Journal of Sedimentary Research, v. 79, no. 11, p. 793-807.
Dashtgard, S. E., Vaucher, R., Yang, B., and Dalrymple, R. W., 2021, Hutchison medallist 1. Wave-dominated to tide-dominated coastal systems: a unifying model for tidal shorefaces and refinement of the coastal-environments classification scheme: Geoscience Canada, v. 48, no. 1, p. 5-22.
Davies, G., 1970, Algal-laminated sediments, Gladstone Embayment, Shark Bay, Western Australia.
Dehler, C., Gehrels, G., Porter, S., Heizler, M., Karlstrom, K., Cox, G., Crossey, L., and Timmons, M., 2017, Synthesis of the 780–740 Ma Chuar, Uinta Mountain, and Pahrump (ChUMP) groups, western USA: Implications for Laurentia-wide cratonic marine basins: Bulletin, v. 129, no. 5-6, p. 607-624.
Delaney, G., 1981, The mid-Proterozoic Wernecke Supergroup, Wernecke Mountains, Yukon Territory, Proterozoic basins of Canada, Volume 81, Geol. Surv. Can, p. 1-23.
Dennen, K. O., Johnson, C. A., Otter, M. L., Silva, S. R., and Wandless, G. A., 2006, delta 15N and non-carbonate delta 13C values for two petroleum source rock reference materials and a marine sediment reference material, 2331-1258.
Denyszyn, S. W., Halls, H. C., Davis, D. W., and Evans, D. A., 2009, Paleomagnetism and U–Pb geochronology of Franklin dykes in High Arctic Canada and Greenland: a revised age and paleomagnetic pole constraining block rotations in the Nares Strait region: Canadian Journal of Earth Sciences, v. 46, no. 9, p. 689-705.
Derry, L. A., 2015, Causes and consequences of mid-Proterozoic anoxia: Geophysical Research Letters, v. 42, no. 20, p. 8538-8546.
Derry, L. A., and Jacobsen, S. B., 1990, The chemical evolution of Precambrian seawater: Evidence from REEs in banded iron formations: Geochimica et Cosmochimica Acta, v. 54, no. 11, p. 2965-2977.
Di Bella, M., Sabatino, G., Quartieri, S., Ferretti, A., Cavalazzi, B., Barbieri, R., Foucher, F., Messori, F., and Italiano, F., 2019, Modern Iron ooids of Hydrothermal origin as a proxy for Ancient Deposits: Scientific reports, v. 9, no. 1, p. 1-9.
Dimroth, E., and Chauvel, J.-J., 1973, Petrography of the Sokoman iron formation in part of the central Labrador trough, Quebec, Canada: Geological Society of America Bulletin, v. 84, no. 1, p. 111-134.
Dimroth, E., and Wolf, K., 1976, Aspects of the sedimentary pertrology of cherty iron-formation, Au, U, Fe, Mn, Hg, Sb, W, and P Deposits, Elsevier, p. 203-254.
Dodd, M. S., Papineau, D., She, Z., Fogel, M. L., Nederbragt, S., and Pirajno, F., 2018, Organic remains in late Palaeoproterozoic granular iron formations and implications for the origin of granules: Precambrian Research, v. 310, p. 133-152.
Donaldson, W. S., Plint, A. G., and Longstaffe, F. J., 1999, Tectonic and eustatic control on deposition and preservation of Upper Cretaceous ooidal ironstone and associated facies: Peace River Arch area, NW Alberta, Canada: Sedimentology, v. 46, no. 6, p. 1159-1182.
Donoghue, P. C., Harrison, C. J., Paps, J., and Schneider, H., 2021, The evolutionary emergence of land plants: Current Biology, v. 31, no. 19, p. R1281-R1298.
Dorland, H. C., 1999, Paleoproterozoic laterites, red beds and ironstones of the Pretoria Group with reference to the history of atmospheric oxygen: University of Johannesburg.
Dreesen, R., 1989, Oolitic ironstones as event-stratigraphical marker beds within the Upper Devonian of the Ardenno-Rhenish Massif: Geological Society, London, Special Publications, v. 46, no. 1, p. 65-78.
Dreesen, R., Savary, X., and Geomaere, E., 2016, Definition, classification and microfacies characteristics of oolitic ironstone used in the manufacture of red ochre. A comparative petrographic analysis of Palaeozoic samples from France, Belgium and Germany: Anthropologica et Praehistorica, v. 125, no. 5, p. 203-223.
Drever, J., and Stillings, L., 1997, The role of organic acids in mineral weathering: Colloids and Surfaces A: physicochemical and engineering aspects, v. 120, no. 1-3, p. 167-181.
Druschel, G. K., Emerson, D., Sutka, R., Suchecki, P., and Luther III, G. W., 2008, Low-oxygen and chemical kinetic constraints on the geochemical niche of neutrophilic iron (II) oxidizing microorganisms: Geochimica et Cosmochimica Acta, v. 72, no. 14, p. 3358-3370.
Dumas, S., and Arnott, R., 2006, Origin of hummocky and swaley cross-stratification—The controlling influence of unidirectional current strength and aggradation rate: Geology, v. 34, no. 12, p. 1073-1076.

Duncanson, S., Brengman, L., Johnson, J., Eyster, A., Fournelle, J., and Moy, A., 2024, Reconstructing diagenetic mineral reactions from silicified horizons of the Paleoproterozoic Biwabik Iron Formation, Minnesota: American Mineralogist, v. 109, no. 2, p. 339-358.
Duncanson, S., Brengman, L., Johnson, J. E., Eyster, A., Fournelle, J., and Moy, A., 2023, Reconstructing diagenetic mineral reactions from silicified horizons of the Paleoproterozoic Biwabik Iron Formation, Minnesota: American Mineralogist.
Dunham, R. J., 1962, Classification of carbonate rocks according to depositional textures.
Dunn, S. K., Pufahl, P. K., Murphy, J. B., and Lokier, S. W., 2021, Middle Ordovician Upwelling-Related Ironstone of North Wales: Coated Grains, Ocean Chemistry, and Biological Evolution: Frontiers in Earth Science, p. 709.
Durbano, A. M., Pratt, B. R., Hadlari, T., and Dewing, K., 2015, Sedimentology of an early Cambrian tide-dominated embayment: Quyuk formation, Victoria Island, Arctic Canada: Sedimentary Geology, v. 320, p. 1-18.
Egal, M., Elbaz-Poulichet, F., Casiot, C., Motelica-Heino, M., Négrel, P., Bruneel, O., Sarmiento, A. M., and Nieto, J., 2008, Iron isotopes in acid mine waters and iron-rich solids from the Tinto–Odiel Basin (Iberian Pyrite Belt, Southwest Spain): Chemical Geology, v. 253, no. 3-4, p. 162-171.
Eisbacher, G., 1978, Two major Proterozoic unconformities, northern Cordillera: Current research, part A. Geological Survey of Canada, Paper, v. 78, p. 53-58.
Eisbacher, G., 1985, Late Proterozoic rifting, glacial sedimentation, and sedimentary cycles in the light of Windermere deposition, western Canada: Palaeogeography, Palaeoclimatology, Palaeoecology, v. 51, no. 1-4, p. 231-254.
El-Shazly, A. K., Khalil, K. I., and Helba, H., 2019, Geochemistry of banded iron formations and their host rocks from the Central Eastern Desert of Egypt: a working genetic model and tectonic implications: Precambrian Research, v. 325, p. 192-216.
Emerson, D., Fleming, E. J., and McBeth, J. M., 2010, Iron-oxidizing bacteria: an environmental and genomic perspective: Annual review of microbiology, v. 64, p. 561-583.
Emerson, D., Roden, E., and Twining, B. S., 2012, The microbial ferrous wheel: iron cycling in terrestrial, freshwater, and marine environments, Volume 3, Frontiers Media SA, p. 383.
Eriksson, P., Altermann, W., Eberhardt, L., Arend-Heidbrinck, S., and Bumby, A., 2002, Palaeoproterozoic epeiric sea palaeoenvironments: the Silverton formation (Pretoria group, Transvaal supergroup), South Africa: Precambrian sedimentary environments: a modern approach to ancient depositional systems, p. 351-367.
Eriksson, P. G., and Cheney, E. S., 1992, Evidence for the transition to an oxygen-rich atmosphere during the evolution of red beds in the Lower Proterozoic sequences of southern Africa: Precambrian Research, v. 54, no. 2-4, p. 257-269.
Eriksson, P. G., Condie, K., Tirsgaard, H., Mueller, W., Altermann, W., Miall, A., Aspler, L., Catuneanu, O., and Chiarenzelli, J., 1998, Precambrian clastic sedimentation systems: Sedimentary Geology, v. 120, no. 1-4, p. 5-53.
Eriksson, P. G., and Reczko, B. F., 1998, Contourites associated with pelagic mudrocks and distal delta-fed turbidites in the Lower Proterozoic Timeball Hill Formation epeiric basin (Transvaal Supergroup), South Africa: Sedimentary Geology, v. 120, no. 1-4, p. 319-335.
Eyster, A., Weiss, B. P., Karlstrom, K., and Macdonald, F. A., 2020, Paleomagnetism of the Chuar Group and evaluation of the late Tonian Laurentian apparent polar wander path with implications for the makeup and breakup of Rodinia: GSA Bulletin, v. 132, no. 3-4, p. 710-738.
Eyster, A. E., Fu, R. R., Strauss, J. V., Weiss, B. P., Roots, C. F., Halverson, G. P., Evans, D. A., and Macdonald, F. A., 2017, Paleomagnetic evidence for a large rotation of the Yukon block relative to Laurentia: Implications for a low-latitude Sturtian glaciation and the breakup of Rodinia: Bulletin, v. 129, no. 1-2, p. 38-58.
Fakhraee, M., Hancisse, O., Canfield, D. E., Crowe, S. A., and Katsev, S., 2019, Proterozoic seawater sulfate scarcity and the evolution of ocean–atmosphere chemistry: Nature Geoscience, v. 12, no. 5, p. 375-380.
Fan, D., 2012, Open-Coast Tidal Flats, *in* Davis Jr, R. A., and Dalrymple, R. W., eds., Principles of Tidal Sedimentology: Dordrecht, Springer, p. 187-229.
Fedo, C. M., Wayne Nesbitt, H., and Young, G. M., 1995, Unraveling the effects of potassium metasomatism in sedimentary rocks and paleosols, with implications for paleoweathering conditions and provenance: Geology, v. 23, no. 10, p. 921-924.
Fernex, F., Février, G., Bénaïm, J., and Arnoux, A., 1992, Copper, lead and zinc trapping in Mediterranean deep-sea sediments: probable coprecipitation with Mn and Fe: Chemical Geology, v. 98, no. 3-4, p. 293-306.
Finke, N., Simister, R., O'Neil, A., Nomosatryo, S., Henny, C., MacLean, L., Canfield, D., Konhauser, K., Lalonde, S., and Fowle, D. A., 2019, Mesophilic microorganisms build terrestrial mats analogous to Precambrian microbial jungles: Nature Communications, v. 10, no. 1, p. 4323.
Fiorella, R. P., and Sheldon, N. D., 2017, Equable end Mesoproterozoic climate in the absence of high CO2: Geology, v. 45, no. 3, p. 231-234.
Fischer, W. W., and Knoll, A. H., 2009, An iron shuttle for deepwater silica in Late Archean and early Paleoproterozoic iron formation: Geological Society of America Bulletin, v. 121, no. 1-2, p. 222-235.
Flanagan, F. J., and Gottfried, D., 1980, USGS rock standards; III, Manganese-nodule reference samples USGS-Nod-A-1 and USGS-Nod-P-1: US Govt. Print Off., 2330-7102.
Flemming, B. W., 2012, Siliciclastic Back-Barrier Tidal Flats, Principles of Tidal Sedimentology, Springer Science + Business Media, p. 231-267.

Fralick, P., Davis, D. W., and Kissin, S. A., 2002, The age of the Gunflint Formation, Ontario, Canada: single zircon U–Pb age determinations from reworked volcanic ash: Canadian Journal of Earth Sciences, v. 39, no. 7, p. 1085-1091.
Fralick, P., and Pufahl, P. K., 2006, Iron formation in Neoarchean deltaic successions and the microbially mediated deposition of transgressive systems tracts: Journal of Sedimentary Research, v. 76, no. 9, p. 1057-1066.
French, B. M., 1973, Mineral assemblages in diagenetic and low-grade metamorphic iron-formation: Economic Geology, v. 68, no. 7, p. 1063-1074.
Fritz, S. J., and Toth, T. A., 1997, An Fe-berthierine from a Cretaceous laterite: Part II. Estimation of Eh, pH and pCO 2 conditions of formation: Clays and Clay Minerals, v. 45, no. 4, p. 580-586.
Fryer, B., 1977, Rare earth evidence in iron-formations for changing Precambrian oxidation states: Geochimica et Cosmochimica Acta, v. 41, no. 3, p. 361-367.
Fujisaki, W., Matsui, Y., Ueda, H., Sawaki, Y., Suzuki, K., and Maruoka, T., 2022, Pre-treatment methods for accurate determination of total nitrogen and organic carbon contents and their stable Isotopic compositions: Re-evaluation from geological reference materials: Geostandards and Geoanalytical Research, v. 46, no. 1, p. 5-19.
Fürsich, F. T., Alberti, M., and Pandey, D. K., 2021, Palaeoecological analysis of maximum flooding zones from the Tithonian (Upper Jurassic) of the Kachchh Basin, western India: Facies, v. 67, no. 1, p. 1-27.
Gabrielse, H., Blusson, S. L., and Roddick, J. A., 1973, Geology of Flat River, Glacier Lake, and Wrigley Lake map-areas, District of Mackenzie and Yukon Territory: Geological Survey of Canada Memoir, v. 366, p. 153.
Galán-Abellán, A. B., Barrenechea, J. F., Benito, M., De la Horra, R., Luque, F., Alonso-Azcárate, J., Arche, A., López-Gómez, J., and Lago, M., 2013, Palaeoenvironmental implications of aluminium phosphate-sulphate minerals in Early–Middle Triassic continental sediments, SE Iberian Range (Spain): Sedimentary Geology, v. 289, p. 169-181.
Galy, V., Bouchez, J., and France-Lanord, C., 2007, Determination of total organic carbon content and δ13C in carbonate-rich detrital sediments: Geostandards and Geoanalytical research, v. 31, no. 3, p. 199-207.
Garcia-Frank, A., Ureta, S., and Mas, R., 2012, Iron-coated particles from condensed Aalenian–Bajocian deposits: evolutionary model (Iberian Basin, Spain): Journal of Sedimentary Research, v. 82, no. 12, p. 953-968.
Garnit, H., and Bouhlel, S., 2017, Petrography, mineralogy and geochemistry of the Late Eocene oolitic ironstones of the Jebel Ank, Southern Tunisian Atlas: Ore Geology Reviews, v. 84, p. 134-153.
Garrels, R. M., 1965, Silica: role in the buffering of natural waters: Science, v. 148, no. 3666, p. 69-69.
Garzanti, E., 1993, Himalayan ironstones," superplumes," and the breakup of Gondwana: Geology, v. 21, no. 2, p. 105-108.
Gehling, J. G., 1999, Microbial mats in terminal Proterozoic siliciclastics; Ediacaran death masks: Palaios, v. 14, no. 1, p. 40-57.
Gehring, A., 1985, A microchemical study of iron ooids: Eclogae Geologicae Helvetiae, v. 78, no. 3, p. 451-457.
Gehring, A., 1989, The formation of goethitic ooids in condensed Jurassic deposits in northern Switzerland: Geological Society, London, Special Publications, v. 46, no. 1, p. 133-139.
Geijer, P., 1962, Some aspects of phosphorus in Precambrian sedimentation: Ark. Miner. Geol., v. 3, p. 165-186.
Gharaie, M. H. M., Matsumoto, R., Kakuwa, Y., and Milroy, P. G., 2004, Late Devonian facies variety in Iran: volcanism as a possible trigger of the environmental perturbation near the Frasnian-Famennian boundary: Geological Quarterly, v. 48, no. 4, p. 323-332.
Gibson, T., Halverson, G., Macdonald, F., Cumming, V., Kunzmann, M., Wörndle, S., Lechte, M., Maloney, K., Millikin, A., and Murphy, J., 2019, Tectono-stratigraphy and facies architecture of the Tonian Hematite Creek and Katherine groups, Wernecke Mountains, Yukon: GAC-MAC-IAH Québec 2019.
Gibson, T. M., Kunzmann, M., Poirier, A., Schumann, D., Tosca, N. J., and Halverson, G. P., 2020, Geochemical signatures of transgressive shale intervals from the 811 Ma Fifteenmile Group in Yukon, Canada: Disentangling sedimentary redox cycling from weathering alteration: Geochimica et Cosmochimica Acta.
Gibson, T. M., Millikin, A. E., Anderson, R. P., Myrow, P. M., Rooney, A. D., and Strauss, J. V., 2021, Tonian deltaic and storm-influenced marine sedimentation on the edge of Laurentia: The Veteranen Group of northeastern Spitsbergen, Svalbard: Sedimentary Geology, v. 426, p. 106011.
Glaessner, M. F., Preiss, W. V., and Walter, M. R., 1969, Precambrian columnar stromatolites in Australia: morphological and stratigraphic analysis: Science, v. 164, no. 3883, p. 1056-1058.
Goldstein, S., O'nions, R., and Hamilton, P., 1984, A Sm-Nd isotopic study of atmospheric dusts and particulates from major river systems: Earth and planetary Science letters, v. 70, no. 2, p. 221-236.
Goldstein, S. J., and Jacobsen, S. B., 1987, The Nd and Sr isotopic systematics of river-water dissolved material: Implications for the sources of Nd and Sr in seawater: Chemical Geology: Isotope Geoscience section, v. 66, no. 3-4, p. 245-272.
Goodwin, A., 1962, Structure, stratigraphy, and origin of iron formations, Michipicoten area, Algoma District, Ontario, Canada: Geological Society of America Bulletin, v. 73, no. 5, p. 561-586.
Goodwin, A., 1973, Archean iron-formations and tectonic basins of the Canadian Shield: Economic Geology, v. 68, no. 7, p. 915-933.
Gorter, J. D., 1991, Oolitic and pisolitic ironstones in the Early Ordovician (Arenig) of the Amadeus Basin, central Australia: Geological and Geophysical Studies in the Amadeus Basin, Central Australia, Bulletin 236, p. 303-315.

Graf Jr, J. L., 1978, Rare earth elements, iron formations and sea water: Geochimica et Cosmochimica Acta, v. 42, no. 12, p. 1845-1850.
Grenne, T., and Slack, J. F., 2003, Bedded jaspers of the Ordovician Løkken ophiolite, Norway: seafloor deposition and diagenetic maturation of hydrothermal plume-derived silica-iron gels: Mineralium Deposita, v. 38, no. 5, p. 625-639.
Grgic, D., Giraud, A., and Auvray, C., 2013, Impact of chemical weathering on micro/macro-mechanical properties of oolithic iron ore: International Journal of Rock Mechanics and Mining Sciences, v. 64, p. 236-245.
Gross, G., 1965a, Iron-formation of Snake River area, Yukon and Northwest Territories, Report of Activities: Field, 1964, p. 143.
Gross, G., and Zajac, I., 1983, Iron-formation in fold belts marginal to the Ungava craton, Developments in Precambrian Geology, Volume 6, Elsevier, p. 253-294.
Gross, G. A., 1965b, Geology of iron deposits in Canada, Department of Mines and Technical Surveys, Canada, v. 22.
Gross, G. A., 1980, A classification of iron formations based on depositional environments: The Canadian Mineralogist, v. 18, no. 2, p. 215-222.
Gross, G. A., 1983, Tectonic systems and the deposition of iron-formation: Precambrian Research, v. 20, no. 2-4, p. 171-187.
Grotzinger, J. P., 1989, Facies and evolution of Precambrian carbonate depositional systems: emergence of the modern platform archetype.
Gruner, J. W., 1922, The origin of sedimentary iron formations: the Biwabik Formation of the Mesabi Range: Economic Geology, Vol. XVII, No. 6, September 1922, pages 407-460.
Guerrak, S., 1989, Time and space distribution of Palaeozoic oolitic ironstones in the Tindouf Basin, Algerian Sahara: Geological Society, London, Special Publications, v. 46, no. 1, p. 197-212.
Guerrak, S., 1991, Paleozoic patterns of oolitic ironstone sedimentation in the Sahara: Journal of African Earth Sciences (and the Middle East), v. 12, no. 1-2, p. 31-39.
Guilbaud, R., Poulton, S. W., Butterfield, N. J., Zhu, M., and Shields-Zhou, G. A., 2015, A global transition to ferruginous conditions in the early Neoproterozoic oceans: Nature Geoscience, v. 8, no. 6, p. 466.
Gygi, R., 1981, Oolitic iron formations: marine or not marine?: Eclogae Geologicae Helvetiae, v. 74, no. 1, p. 233-254.
Halevy, I., and Bachan, A., 2017, The geologic history of seawater pH: Science, v. 355, no. 6329, p. 1069-1071.
Hall, W., and Goode, A., 1978, The early Proterozoic Nabberu Basin and associated iron formations of Western Australia: Precambrian Research, v. 7, no. 2, p. 129-184.
Hallam, A., 1963, Observations on the palaeoecology and ammonite sequence of the Frodingham Ironstone (Lower Jurassic): Palaeontology, v. 6, no. 3, p. 554-574.
Hallam, A., 1966, Depositional environment of British Liassic ironstones considered in the context of their facies relationships: Nature, v. 209, no. 5030, p. 1306-1309.
Hallam, A., 1967, An environmental study of the upper Domerian and lower Toarcian in Great Britain: Philosophical Transactions of the Royal Society of London. Series B, Biological Sciences, v. 252, no. 778, p. 393-445.
Hallam, A., 1985, A review of Mesozoic climates: Journal of the Geological Society, v. 142, no. 3, p. 433-445.
Hallam, A., and Bradshaw, M., 1979, Bituminous shales and oolitic ironstones as indicators of transgressions and regressions: Journal of the Geological Society, v. 136, no. 2, p. 157-164.
Hallimond, A., Dunham, K., Hemingway, J., Taylor, J., Davies, W., Dixie, R., and Bannister, F., 1951, The constitution and origin of sedimentary iron ores: a symposium: Proceedings of the Yorkshire Geological Society, v. 28, no. 2, p. 61-101.
Hallimond, A. F., 1925, Iron Ores: Bedded ores of England and Wales: Petrography and chemistry, HM Stationery Office.
Halverson, G., Shen, C., Davies, J., and Wu, L., 2022, A Bayesian Approach to Inferring Depositional Ages Applied to a Late Tonian Reference Section in Svalbard. Front: Earth Sci, v. 10, p. 798739.
Halverson, G. P., 2006, A Neoproterozoic chronology, Neoproterozoic geobiology and paleobiology, Springer, p. 231-271.
Hao, W., Mänd, K., Li, Y., Alessi, D. S., Somelar, P., Moussavou, M., Romashkin, A. E., Lepland, A., Kirsimäe, K., and Planavsky, N. J., 2021, The kaolinite shuttle links the Great Oxidation and Lomagundi events: Nature communications, v. 12, no. 1, p. 2944.
Harder, H., 1989, Mineral genesis in ironstones: a model based upon laboratory experiments and petrographic observations: Geological Society, London, Special Publications, v. 46, no. 1, p. 9-18.
Harms, J., Iron ore deposits of Constance Range, *in* Proceedings Eighth Commonwealth Mining and Metallurgical Congress of
Australia and New Zealand, Melbourne, 1965, The Australian Institute of Mining and Metallurgy, p. 264-269.
Hatch, F., 1920, The iron ore supplies of the world: Geological Magazine, v. 57, no. 11, p. 504-517.
Haugaard, R., Pecoits, E., Lalonde, S., Rouxel, O., and Konhauser, K., 2016, The Joffre banded iron formation, Hamersley Group, Western Australia: assessing the palaeoenvironment through detailed petrology and chemostratigraphy: Precambrian Research, v. 273, p. 12-37.
Havig, J. R., Grettenberger, C., and Hamilton, T. L., 2017, Geochemistry and microbial community composition across a range of acid mine drainage impact and implications for the Neoarchean-Paleoproterozoic transition: Journal of Geophysical Research: Biogeosciences, v. 122, no. 6, p. 1404-1422.

Heard, A. W., Aarons, S. M., Hofmann, A., He, X., Ireland, T., Bekker, A., Qin, L., and Dauphas, N., 2021, Anoxic continental surface weathering recorded by the 2.95 Ga Denny Dalton Paleosol (Pongola Supergroup, South Africa): Geochimica et Cosmochimica Acta, v. 295, p. 1-23.
Hedrich, S., Schlömann, M., and Johnson, D. B., 2011, The iron-oxidizing proteobacteria: Microbiology, v. 157, no. 6, p. 1551-1564.
Heikoop, J. M., Tsujita, C. J., Risk, M. J., Tomascik, T., and Mah, A. J., 1996, Modern iron ooids from a shallow-marine volcanic setting: Mahengetang, Indonesia: Geology, v. 24, no. 8, p. 759-762.
Hein, J. R., Koschinsk, A., Bau, M., Manheim, F. T., Kang, J.-K., and Roberts, L., 2017, Cobalt-rich ferromanganese crusts in the Pacific, Handbook of marine mineral deposits, Routledge, p. 239-279.
Hemingway, J., 1951, Cyclic sedimentation and the deposition of ironstone in the Yorkshire Lias: Proceedings of the Yorkshire Geological Society, v. 28, p. 67-74.
Hemingway, J., 1974, Jurassic. 161-233 in Rayner, DH and Hemingway, JE (eds), The geology and mineral resources of Yorkshire: Leeds: Yorkshire Geological Society.
Hepburn, L. E., Butler, I. B., Boyce, A., and Schröder, C., 2020, The use of operationally-defined sequential Fe extraction methods for mineralogical applications: A cautionary tale from Mössbauer spectroscopy: Chemical Geology, v. 543, p. 119584.
Heubeck, C., 2019, The Moodies Group—a high-resolution archive of Archaean surface processes and basin-forming mechanisms: The Archaean Geology of the Kaapvaal Craton, Southern Africa, p. 133-169.
Hofmann, H., and Altken, J., 1979, Precambrian biota from the Little Dal Group, Mackenzie Mountains, northwestern Canada: Canadian Journal of Earth Sciences, v. 16, no. 1, p. 150-166.
Hofmann, H., Fritz, W., and Narbonne, G., 1983, Ediacaran (Precambrian) fossils from the wernecke mountains, northwestern Canada: Science, v. 221, no. 4609, p. 455-457.
Hofmann, H. J., 1985, The mid-Proterozoic Little Dal macrobiota, Mackenzie Mountains, north-west Canada: Palaeontology, v. 28, no. 2, p. 331-354.
Holland, H. D., 1973, The oceans; a possible source of iron in iron-formations: Economic Geology, v. 68, no. 7, p. 1169-1172.
Hollis, S. P., Cooper, M. R., Herrington, R. J., Roberts, S., Earls, G., Verbeeten, A., Piercey, S. J., and Archibald, S. M., 2015, Distribution, mineralogy and geochemistry of silica-iron exhalites and related rocks from the Tyrone Igneous Complex: Implications for VMS mineralization in Northern Ireland: Journal of Geochemical Exploration, v. 159, p. 148-168.
Hongve, D., 1997, Cycling of iron, manganese, and phosphate in a meromictic lake: Limnology and Oceanography, v. 42, no. 4, p. 635-647.
Hou, K., Chen, Z., and Yu, J., 1983, Ore fabric and effect of blue-algae on iron enrichment in the Xuanlong iron mine, Heibei: Chinese Journal of Geology, v. 3.
Hu, J., Jin, W., Tian, Y., Deng, X., Li, S., Kong, L., Santosh, M., Liu, Y., Wang, J., and Xu, D., 2023, Deposition of a newly identified Mesoproterozoic iron formation from the Dabie orogen: Influenced by high-T hydrothermal fluid and redox stratification: Precambrian Research, v. 390, p. 107043.
Hu, J., Wang, H., and Wang, M., 2017, Geochemistry and origin of the Neoproterozoic Dahongliutan banded iron formation (BIF) in the Western Kunlun orogenic belt, Xinjiang (NW China): Ore Geology Reviews, v. 89, p. 836-857.
Hu, J., Wang, M., Wang, H., Li, S., Santosh, M., Zhao, Y., Li, D., Yan, Q., Dong, R., and Ren, H., 2022, The source and depositional environment of early Silurian iron formation in NW China: Constraints from element and isotope (Fe, C, O) geochemistry: Ore Geology Reviews, p. 105165.
Hu, S., Wang, K., Wang, T., Yang, T., Luo, P., Shi, S., Wang, S., and Su, J., 2020, Sedimentary environment and organic matter accumulation of Neoproterozoic black shale in the North China Craton: A case study of the Tonian Baishugou Formation in the Luonan area: Palaeogeography, palaeoclimatology, palaeoecology, v. 547, p. 109694.
Huerta-Diaz, M. A., and Morse, J. W., 1992, Pyritization of trace metals in anoxic marine sediments: Geochimica et Cosmochimica Acta, v. 56, no. 7, p. 2681-2702.
Hume, G. S., and Link, T. A., 1945, Canol geological investigations in the Mackenzie River area, Northwest Territories and Yukon, Canada Department of Mines and Resources, Mines and Geology Branch.
Hunt, J. A., Baker, T., and Thorkelson, D. J., 2010, Wernecke Breccia: Proterozoic IOCG mineralised breccia system, Yukon, Canada: Hydrothermal iron oxide copper-gold and related deposits: a global perspective, v. 4, p. 345-356.
Hunter, K. A., and Boyd, P. W., 2007, Iron-binding ligands and their role in the ocean biogeochemistry of iron: Environmental Chemistry, v. 4, no. 4, p. 221-232.
Huston, D. L., and Logan, G. A., 2004, Barite, BIFs and bugs: evidence for the evolution of the Earth's early hydrosphere: Earth and Planetary Science Letters, v. 220, no. 1, p. 41-55.
Hutchinson, R., RH, R., and GG, S., 1971, Metallogenic relationships in the Abitibi belt, Canada: a model for Archean metallogeny.
Ielpi, A., and Rainbird, R. H., 2016, Highly variable Precambrian fluvial style recorded in the Nelson Head Formation of Brock Inlier (Northwest Territories, Canada): Journal of Sedimentary Research, v. 86, no. 3, p. 199-216.
Isley, A. E., 1995, Hydrothermal plumes and the delivery of iron to banded iron formation: The Journal of Geology, v. 103, no. 2, p. 169-185.
Isley, A. E., and Abbott, D. H., 1999, Plume-related mafic volcanism and the deposition of banded iron formation: Journal of Geophysical Research: Solid Earth, v. 104, no. B7, p. 15461-15477.

Isson, T. T., and Planavsky, N. J., 2018, Reverse weathering as a long-term stabilizer of marine pH and planetary climate: Nature, v. 560, no. 7719, p. 471-475.
Jackson, M., Muir, M., and Sweet, I., Sedimentology of the Middle Proterozoic McArthur Basin, Northern Australia—Field Excursion 13A, *in* Proceedings 12th International Sedimentological Congress1986, Bureau of Mineral Resources Canberra.
Jacobsen, S. B., and Pimentel-Klose, M. R., 1988, A Nd isotopic study of the Hamersley and Michipicoten banded iron formations: the source of REE and Fe in Archean oceans: Earth and Planetary Science Letters, v. 87, no. 1, p. 29-44.
Jacobsen, S. B., and Wasserburg, G., 1980, Sm-Nd isotopic evolution of chondrites: Earth and Planetary Science Letters, v. 50, no. 1, p. 139-155.
James, H. L., 1954, Sedimentary facies of iron-formation: Economic Geology, v. 49, no. 3, p. 235-293.
James, H. L., 1966, Chemistry of the iron-rich sedimentary rocks, US Government Printing Office.
James, H. L., 1992, Precambrian iron-formations: nature, origin, and mineralogic evolution from sedimentation to metamorphism, Developments in sedimentology, Volume 47, Elsevier, p. 543-589.
James Jr, H. E., and Van Houten, F. B., 1979, Miocene goethitic and chamositic oolites, northeastern Colombia: Sedimentology, v. 26, no. 1, p. 125-133.
Jang, K., Huh, Y., and Han, Y., 2018, Diagenetic overprint on authigenic Nd isotope records: A case study of the Bering Slope: Earth and Planetary Science Letters, v. 498, p. 247-256.
Jeandel, C., Arsouze, T., Lacan, F., Techine, P., and Dutay, J.-C., 2007, Isotopic Nd compositions and concentrations of the lithogenic inputs into the ocean: A compilation, with an emphasis on the margins: Chemical Geology, v. 239, no. 1-2, p. 156-164.
Jefferson, C., and Young, G., 1988, Late Proterozoic orange-weathering stromatolite biostrome Mackenzie Mountains and western Arctic Canada.
Jochum, K. P., Weis, U., Schwager, B., Stoll, B., Wilson, S. A., Haug, G. H., Andreae, M. O., and Enzweiler, J., 2016, Reference values following ISO guidelines for frequently requested rock reference materials: Geostandards and Geoanalytical Research, v. 40, no. 3, p. 333-350.
Johnson, B., 2021, The sedimentology, mineralogy and geochemistry of the ~1.4 Ga Roper Superbasin Northern Australia: University of Oxford.
Johnson, B. R., Tostevin, R., Gopon, P., Wells, J., Robinson, S. A., and Tosca, N. J., 2020a, Phosphorus burial in ferruginous SiO2-rich Mesoproterozoic sediments: Geology, v. 48, no. 1, p. 92-96.
Johnson, C. M., Beard, B. L., and Weyer, S., 2020b, Iron Geochemistry: An Isotopic Perspective, Springer.
Johnson, J. E., Webb, S. M., Ma, C., and Fischer, W. W., 2016, Manganese mineralogy and diagenesis in the sedimentary rock record: Geochimica et Cosmochimica Acta, v. 173, p. 210-231.
Kamber, B. S., Greig, A., and Collerson, K. D., 2005, A new estimate for the composition of weathered young upper continental crust from alluvial sediments, Queensland, Australia: Geochimica et Cosmochimica Acta, v. 69, no. 4, p. 1041-1058.
Kappler, A., Bryce, C., Mansor, M., Lueder, U., Byrne, J., and Swanner, E. D., 2021, An evolving view on biogeochemical cycling of iron: Nature Reviews Microbiology.
Kasting, J. F., 1993, Earth's early atmosphere: Science, v. 259, no. 5097, p. 920-926.
Kearsley, A., 1989, Iron-rich ooids, their mineralogy and microfabric: clues to their origin and evolution: Geological Society, London, Special Publications, v. 46, no. 1, p. 141-164.
Kendall, C. G. S. C., and Warren, J., 1987, A review of the origin and setting of tepees and their associated fabrics: Sedimentology, v. 34, no. 6, p. 1007-1027.
Khedr, E. S., 1991, Structure and microchemistry of ferriferous coated grains evoluted in various ancient environments, southern Egypt: Mineralogist, v. 3, p. 57-94.
Kimberley, M., 1978, Paleoenvironmental classification of iron formations: Economic Geology, v. 73, no. 2, p. 215-229.
Kimberley, M. M., 1983, Ferriferous ooids, Coated grains, Springer, p. 100-108.
Kimberley, M. M., 1989, Nomenclature for iron formations: Ore Geology Reviews, v. 5, no. 1-2, p. 1-12.
Kimberley, M. M., 1994, Debate about ironstone: has solute supply been surficial weathering, hydrothermal convection, or exhalation of deep fluids?: Terra Nova, v. 6, no. 2, p. 116-132.
Kirscher, U., Mitchell, R. N., Liu, Y., Nordsvan, A. R., Cox, G. M., Pisarevsky, S. A., Wang, C., Wu, L., Murphy, J. B., and Li, Z.-X., 2021, Paleomagnetic constraints on the duration of the Australia-Laurentia connection in the core of the Nuna supercontinent: Geology, v. 49, no. 2, p. 174-179.
Kjerfve, B., and Magill, K. E., 1989, Geographic and hydrodynamic characteristics of shallow coastal lagoons: Marine geology, v. 88, no. 3-4, p. 187-199.
Klein, C., 2005, Some Precambrian banded iron-formations (BIFs) from around the world: Their age, geologic setting, mineralogy, metamorphism, geochemistry, and origins: American Mineralogist, v. 90, no. 10, p. 1473-1499.
Klein, C., and Beukes, N. J., 1993, Sedimentology and geochemistry of the glaciogenic late Proterozoic Rapitan iron-formation in Canada: Economic Geology, v. 88, no. 3, p. 542-565.
Kleinmann, R., Crerar, D., and Pacelli, R., 1981, Biogeochemistry of Acid Mine Drainage and a Method to Control Acid Formation: Mining Engineering, v. 33:3.
Klinkhammer, G., Elderfield, H., and Hudson, A., 1983, Rare earth elements in seawater near hydrothermal vents: Nature, v. 305, p. 185-188.
Knox, R. O. B., 1970, Chamosite ooliths from the Winter Gill ironstone (Jurassic) of Yorkshire, England: Journal of Sedimentary Research, v. 40, no. 4, p. 1216-1225.

Konhauser, K. O., Lalonde, S. V., Planavsky, N. J., Pecoits, E., Lyons, T. W., Mojzsis, S. J., Rouxel, O. J., Barley, M. E., Rosière, C., and Fralick, P. W., 2011, Aerobic bacterial pyrite oxidation and acid rock drainage during the Great Oxidation Event: Nature, v. 478, no. 7369, p. 369.
Konhauser, K. O., Planavsky, N. J., Hardisty, D. S., Robbins, L. J., Warchola, T. J., Haugaard, R., Lalonde, S. V., Partin, C. A., Oonk, P. B., and Tsikos, H., 2017, Iron formations: A global record of Neoarchaean to Palaeoproterozoic environmental history: Earth-Science Reviews, v. 172, p. 140-177.
Korenaga, J., Planavsky, N. J., and Evans, D. A., 2017, Global water cycle and the coevolution of the Earth's interior and surface environment: Philosophical Transactions of the Royal Society A: Mathematical, Physical and Engineering Sciences, v. 375, no. 2094, p. 20150393.
Koschinsky, A., and Hein, J. R., 2017, Marine ferromanganese encrustations: archives of changing oceans: Elements: An International Magazine of Mineralogy, Geochemistry, and Petrology, v. 13, no. 3, p. 177-182.
Köykkä, J., and Lamminen, J., 2011, Tidally influenced clastic epeiric sea at a Mesoproterozoic continental margin, Rjukan Rift Basin, southern Norway: Precambrian Research, v. 185, no. 3-4, p. 164-182.
Krachler, R., Krachler, R. F., von der Kammer, F., Süphandag, A., Jirsa, F., Ayromlou, S., Hofmann, T., and Keppler, B. K., 2010, Relevance of peat-draining rivers for the riverine input of dissolved iron into the ocean: Science of the Total Environment, v. 408, no. 11, p. 2402-2408.
Krauskopf, K. B., 1956, Dissolution and precipitation of silica at low temperatures: Geochimica et Cosmochimica Acta, v. 10, no. 1-2, p. 1-26.
Krissansen-Totton, J., and Catling, D. C., 2020, A coupled carbon-silicon cycle model over Earth history: Reverse weathering as a possible explanation of a warm mid-Proterozoic climate: Earth and Planetary Science Letters, v. 537, p. 116181.
Krumbein, W. C., and Garrels, R., 1952, Origin and classification of chemical sediments in terms of pH and oxidation-reduction potentials: The Journal of Geology, v. 60, no. 1, p. 1-33.
Kump, L. R., and Seyfried, W. E., 2005, Hydrothermal Fe fluxes during the Precambrian: effect of low oceanic sulfate concentrations and low hydrostatic pressure on the composition of black smokers: Earth and Planetary Science Letters, v. 235, no. 3, p. 654-662.
Kunzmann, M., Halverson, G. P., Scott, C., Minarik, W. G., and Wing, B. A., 2015, Geochemistry of Neoproterozoic black shales from Svalbard: Implications for oceanic redox conditions spanning Cryogenian glaciations: Chemical Geology, v. 417, p. 383-393.
Lalonde, K., Mucci, A., Ouellet, A., and Gélinas, Y., 2012, Preservation of organic matter in sediments promoted by iron: Nature, v. 483, no. 7388, p. 198-200.
Lalonde, S. V., and Konhauser, K. O., 2015, Benthic perspective on Earth's oldest evidence for oxygenic photosynthesis: Proceedings of the National Academy of Sciences, v. 112, no. 4, p. 995-1000.
Lan, C., Long, X., Zhai, M., and Wang, J., 2021, Depositional age and geochemistry of the 2.44–2.32 Ga granular iron formation in the Songshan Group, North China Craton: tracing the effects of atmospheric oxygenation on continental weathering and seawater environment: Precambrian Research, v. 357, p. 106142.
Lan, C., Zhou, Y., Wang, C., and Zhao, T., 2017, Depositional age and protoliths of the Paleoproterozoic upper Taihua Group in the Wuyang area in the southern margin of the North China Craton: New insights into stratigraphic subdivision and tectonic setting: Precambrian Research, v. 297, p. 77-100.
Laughton, J. R., Thorkelson, D. J., Brideau, M.-A., and Hunt, J. A., 2001, Paleoproterozoic volcanism and plutonism in the Wernecke Mountains, Yukon: Yukon exploration and geology, p. 139-145.
Lawrence, C., Harden, J., and Maher, K., 2014, Modeling the influence of organic acids on soil weathering: Geochimica et Cosmochimica Acta, v. 139, p. 487-507.
Lawrence, M. G., Greig, A., Collerson, K. D., and Kamber, B. S., 2006, Rare earth element and yttrium variability in South East Queensland waterways: Aquatic Geochemistry, v. 12, no. 1, p. 39-72.
Le Heron, D., Busfield, M., Smith, A., and Wimmer, S., 2022, A grounding zone wedge origin for the Palaeoproterozoic Makganyene Formation of South Africa: Frontiers in Earth Science, v. 10, p. 905602.
Lechte, M. A., Wallace, M. W., and Hoffmann, K.-H., 2019a, Glacio-marine iron formation deposition in a c. 700 Ma glaciated margin: insights from the Chuos Formation, Namibia: Geological Society, London, Special Publications, v. 475.
Lechte, M. A., Wallace, M. W., van Smeerdijk Hood, A., Li, W., Jiang, G., Halverson, G. P., Asael, D., McColl, S. L., and Planavsky, N. J., 2019b, Subglacial meltwater supported aerobic marine habitats during Snowball Earth: Proceedings of the National Academy of Sciences, v. 116, no. 51, p. 25478-25483.
Lechte, M. A., Wallace, M. W., van Smeerdijk Hood, A., and Planavsky, N., 2018, Cryogenian iron formations in the glaciogenic Kingston Peak Formation, California: Precambrian Research, v. 310, p. 443-462.
Lee Rodgers, J., and Nicewander, W. A., 1988, Thirteen ways to look at the correlation coefficient: The American Statistician, v. 42, no. 1, p. 59-66.
Lei, R.-X., Zhang, K., Muhtar, M., and Wu, C.-Z., 2020, Neoproterozoic non-glaciogenic iron formation: Insights from Fe isotope and elemental geochemistry of the Shalong iron formation from the Central Tianshan block, southern Altaids: Precambrian Research, v. 351, p. 105959.
Leith, C. K., 1908, The iron ores of Canada: Economic Geology, v. 3, no. 4, p. 276-291.
Li, C., and Yang, S., 2010, Is chemical index of alteration (CIA) a reliable proxy for chemical weathering in global drainage basins?: American Journal of Science, v. 310, no. 2, p. 111-127.
Li, F., Zhang, P., Ma, X., and Yuan, G., 2021, The iron oolitic deposits of the lower Devonian Yangmaba formation in the Longmenshan area, Sichuan Basin: Marine and Petroleum Geology, v. 130, p. 105137.

Li, F., Zhu, X., Ding, H., and Zhang, K., 2022, Local hydrothermal sources for Superior-type iron formations: Insights from the Animikie Basin: Precambrian Research, v. 377, p. 106736.
Li, W., Beard, B. L., and Johnson, C. M., 2015, Biologically recycled continental iron is a major component in banded iron formations: Proceedings of the National Academy of Sciences, v. 112, no. 27, p. 8193-8198.
Li, Z., and Zhu, X.-K., 2012, Geochemical features of Xuanlong type iron ore deposit in Hebei Province and their geological significance: Acta Petrologica Sinica, v. 28, no. 9, p. 2903-2911.
Li, Z.-Q., Zhang, L.-C., Xue, C.-J., Zheng, M.-T., Zhu, M.-T., Robbins, L. J., Slack, J. F., Planavsky, N. J., and Konhauser, K. O., 2018, Earth's youngest banded iron formation implies ferruginous conditions in the Early Cambrian ocean: Scientific reports, v. 8, no. 1, p. 9970.
Lide, D. R., 2004, CRC handbook of chemistry and physics, CRC press.
Lin, Y., Tang, D., Shi, X., Zhou, X., and Huang, K., 2019, Shallow-marine ironstones formed by microaerophilic iron-oxidizing bacteria in terminal Paleoproterozoic: Gondwana Research, v. 76, p. 1-18.
Little, C. T., Glynn, S. E., and Mills, R. A., 2004, Four-hundred-and-ninety-million-year record of bacteriogenic iron oxide precipitation at sea-floor hydrothermal vents: Geomicrobiology Journal, v. 21, no. 6, p. 415-429.
Liu, X.-M., Kah, L. C., Knoll, A. H., Cui, H., Wang, C., Bekker, A., and Hazen, R. M., 2021, A persistently low level of atmospheric oxygen in Earth's middle age: Nature Communications, v. 12, no. 1, p. 1-7.
Logan, B. W., 1974, Inventory of diagenesis in Holocene-recent carbonate sediments, Shark Bay, Western Australia.
Long, D., Rainbird, R., Turner, E., and MacNaughton, R., 2008, Early Neoproterozoic strata (Sequence B) of mainland northern Canada and Victoria and Banks islands: a contribution to the Geological Atlas of the Northern Canadian Mainland Sedimentary Basin: Geological Survey of Canada, Open File, v. 5700, no. 2008, p. 27.
Long, D., and Turner, E., 2012, Formal definition of the Neoproterozoic Mackenzie Mountains Supergroup (Northwest Territories), and formal stratigraphic nomenclature for terrigenous clastic units of the Katherine Group, Geological Survey of Canada.
Long, D. G., 1977, Proterozoic stream deposits: some problems of recognition and interpretation of ancient sandy fluvial systems.
Long, D. G., 2011a, Architecture and depositional style of fluvial systems before land plants: a comparison of Precambrian, early Paleozoic, and modern river deposits.
Long, D. G., 2011b, Katherine Group, *in* Martel, E., Turner, E., and Fisher, B., eds., Geology of the central Makenzie Mountains of the Northern Canadian Cordillera, Volume 1, NWT Geoscience Office, p. 39-56.
Lovley, D. R., and Phillips, E. J., 1987, Competitive mechanisms for inhibition of sulfate reduction and methane production in the zone of ferric iron reduction in sediments: Applied and Environmental Microbiology, v. 53, no. 11, p. 2636-2641.
Lovley, D. R., and Phillips, E. J., 1988, Novel mode of microbial energy metabolism: organic carbon oxidation coupled to dissimilatory reduction of iron or manganese: Applied and environmental microbiology, v. 54, no. 6, p. 1472-1480.
Lyons, T. W., Diamond, C. W., Planavsky, N. J., Reinhard, C. T., and Li, C., 2021, Oxygenation, life, and the planetary system during Earth's middle history: An overview: Astrobiology, v. 21, no. 8, p. 906-923.
Ma, J., Shi, X., Lechte, M., Zhou, X., Wang, Z., Huang, K., Rudmin, M., and Tang, D., 2022, Mesoproterozoic seafloor authigenic glauconite-berthierine: Indicator of enhanced reverse weathering on early Earth: American Mineralogist, v. 107, no. 1, p. 116-130.
Macdonald, F., Halverson, G., Strauss, J., Smith, E., Cox, G., Sperling, E., and Roots, C., 2012, Early Neoproterozoic Basin Formation in Yukon, Canada:: Implications for the make-up and break-up of Rodinia: Geoscience Canada, v. 39, no. 2, p. 77-100.
Macdonald, F. A., Schmitz, M. D., Crowley, J. L., Roots, C. F., Jones, D. S., Maloof, A. C., Strauss, J. V., Cohen, P. A., Johnston, D. T., and Schrag, D. P., 2010, Calibrating the cryogenian: Science, v. 327, no. 5970, p. 1241-1243.
Macdonald, F. A., Schmitz, M. D., Strauss, J. V., Halverson, G. P., Gibson, T. M., Eyster, A., Cox, G., Mamrol, P., and Crowley, J. L., 2018, Cryogenian of Yukon: Precambrian Research, v. 319, p. 114-143.
Mackenzie, F. T., and Kump, L. R., 1995, Reverse weathering, clay mineral formation, and oceanic element cycles: Science, v. 270, no. 5236, p. 586-586.
MacLennan, S. A., Eddy, M. P., Merschat, A. J., Mehra, A. K., Crockford, P. W., Maloof, A. C., Southworth, C. S., and Schoene, B., 2020, Geologic evidence for an icehouse Earth before the Sturtian global glaciation: Science Advances, v. 6, no. 24, p. eaay6647.
Madon, M. B., 1992, Depositional setting and origin of berthierine oolitic ironstones in the lower Miocene Terengganu Shale, Tenggol Arch, offshore peninsular Malaysia: Journal of Sedimentary Research, v. 62, no. 5, p. 899-916.
Maloney, K., Halverson, G., Lechte, M., Gibson, T., Bui, T. H., Schiffbauer, J. D., and Laflamme, M., 2024, The paleoredox context of early eukaryotic evolution: insights from the Tonian Mackenzie Mountains Supergroup, Canada: Geobiology.
Maloney, K. M., Halverson, G. P., Schiffbauer, J. D., Xiao, S., Gibson, T. M., Lechte, M. A., Cumming, V. M., Millikin, A. E., Murphy, J. G., Wallace, M. W., Selby, D., and Laflamme, M., 2021, New multicellular marine macroalgae from the early Tonian of northwestern Canada: Geology.
Maloney, K. M., Maverick, D. P., Schiffbauer, J. D., Halverson, G. P., Xiao, S., and Laflamme, M., 2023, Systematic paleontology of macroalgal fossils from the Tonian Mackenzie Mountains Supergroup: Journal of Paleontology, v. 97, no. 2, p. 499-515.

Martins, P. L., Toledo, C. L., Silva, A. M., Chemale Jr, F., Archer, C., and de Assis, L. M., 2022, Chemostratigraphy of the Carajás banded iron formation, Brazil: A record of Neoarchean Ocean chemistry: Gondwana Research, v. 105, p. 217-242.
Matheson, E., and Pufahl, P. K., 2021, Clinton ironstone revisited and implications for Silurian Earth system evolution: Earth Science Reviews.
Matheson, E. J., Pufahl, P. K., Voinot, A., Murphy, J. B., and Fitzgerald, D. M., 2022, Ironstone as a proxy of Paleozoic ocean oxygenation: Earth and Planetary Science Letters, v. 594, p. 117715.
Maynard, J. B., 1986, Geochemistry of oolitic iron ores, an electron microprobe study: Economic Geology, v. 81, no. 6, p. 1473-1483.
McLaughlin, P. I., Emsbo, P., and Brett, C. E., 2012, Beyond black shales: the sedimentary and stable isotope records of oceanic anoxic events in a dominantly oxic basin (Silurian; Appalachian Basin, USA): Palaeogeography, Palaeoclimatology, Palaeoecology, v. 367, p. 153-177.
McLennan, S. M., 1993, Weathering and global denudation: The Journal of Geology, v. 101, no. 2, p. 295-303.
McMahon, S., van Smeerdijk Hood, A., and McIlroy, D., 2017, The origin and occurrence of subaqueous sedimentary cracks: Geological Society, London, Special Publications, v. 448, no. 1, p. 285-309.
Medig, K., Turner, E., Thorkelson, D., and Rainbird, R., 2016, Rifting of Columbia to form a deep-water siliciclastic to carbonate succession: The Mesoproterozoic Pinguicula Group of northern Yukon, Canada: Precambrian Research, v. 278, p. 179-206.
Merdith, A. S., Collins, A. S., Williams, S. E., Pisarevsky, S., Foden, J. D., Archibald, D. B., Blades, M. L., Alessio, B. L., Armistead, S., and Plavsa, D., 2017, A full-plate global reconstruction of the Neoproterozoic: Gondwana Research, v. 50, p. 84-134.
Meunier, A., and El Albani, A., 2007, The glauconite–Fe-illite–Fe-smectite problem: a critical review: Terra Nova, v. 19, no. 2, p. 95-104.
Michalopoulos, P., and Aller, R. C., 1995, Rapid clay mineral formation in Amazon delta sediments: reverse weathering and oceanic elemental cycles: Science, v. 270, no. 5236, p. 614-617.
Michalopoulos, P., and Aller, R. C., 2004, Early diagenesis of biogenic silica in the Amazon delta: alteration, authigenic clay formation, and storage: Geochimica et Cosmochimica Acta, v. 68, no. 5, p. 1061-1085.
Michard, A., Albarede, F., Michard, G., Minster, J., and Charlou, J., 1983, Rare-earth elements and uranium in high-temperature solutions from East Pacific Rise hydrothermal vent field (13 N): Nature, v. 303, no. 5920, p. 795-797.
Miller, R., and O'Nions, R., 1985, Source of Precambrian chemical and clastic sediments: Nature, v. 314, no. 6009, p. 325-330.
Mills, B. J., Scotese, C. R., Walding, N. G., Shields, G. A., and Lenton, T. M., 2017, Elevated CO2 degassing rates prevented the return of Snowball Earth during the Phanerozoic: Nature communications, v. 8, no. 1, p. 1110.
Milton, J. E., Hickey, K. A., Gleeson, S. A., and Friedman, R. M., 2017, New U-Pb constraints on the age of the Little Dal Basalts and Gunbarrel-related volcanism in Rodinia: Precambrian Research, v. 296, p. 168-180.
Mitchell, R. L., and Sheldon, N. D., 2016, Sedimentary provenance and weathering processes in the 1.1 Ga Midcontinental Rift of the Keweenaw Peninsula, Michigan, USA: Precambrian Research, v. 275, p. 225-240.
Mitsch, W. J., Bernal, B., Nahlik, A. M., Mander, Ü., Zhang, L., Anderson, C. J., Jørgensen, S. E., and Brix, H., 2013, Wetlands, carbon, and climate change: Landscape Ecology, v. 28, no. 4, p. 583-597.
Moffett, J. W., 1994, The relationship between cerium and manganese oxidation in the marine environment: Limnology and Oceanography, v. 39, no. 6, p. 1309-1318.
Mohanty, S. P., and Mishra, P. K., 2022, Petrography and geochemistry of the iron-rich rocks in the banded iron formation of the Chilpi Group, Central India: Implications on the level of oxygen in the Paleoproterozoic atmosphere before the "Proterozoic iron ore gap": Geochemistry, p. 125943.
Moorbath, S., O'nions, R., and Pankhurst, R., 1973, Early Archaean age for the Isua iron formation, West Greenland: Nature, v. 245, no. 5421, p. 138.
Morey, G., 1992, Chemical composition of the eastern Biwabik iron-formation (early Proterozoic), Mesabi Range, Minnesota: Economic Geology, v. 87, no. 6, p. 1649-1658.
Morris, R., and Ramanaidou, E., 2007, Genesis of the channel iron deposits (CID) of the Pilbara region, Western Australia: Australian Journal of Earth Sciences, v. 54, no. 5, p. 733-756.
Mücke, A., 2000, Environmental conditions in the Late Cretaceous African Tethys: conclusions from a microscopic-microchemical study of ooidal ironstones from Egypt, Sudan and Nigeria: Journal of African Earth Sciences, v. 30, no. 1, p. 25-46.
Myers, K., 1989, The origin of the Lower Jurassic Cleveland Ironstone Formation of North-East England: evidence from portable gamma-ray spectrometry: Geological Society, London, Special Publications, v. 46, no. 1, p. 221-228.
Nahon, D., Carozzi, A. V., and Parron, C., 1980, Lateritic weathering as a mechanism for the generation of ferruginous ooids: Journal of Sedimentary Research, v. 50, no. 4, p. 1287-1298.
Nesbitt, H., and Wilson, R., 1992, Recent chemical weathering of basalts: American Journal of science, v. 292, no. 10, p. 740-777.
Nesbitt, H., and Young, G., 1982, Early Proterozoic climates and plate motions inferred from major element chemistry of lutites: nature, v. 299, no. 5885, p. 715-717.
Nesbitt, H., Young, G., McLennan, S., and Keays, R., 1996, Effects of chemical weathering and sorting on the petrogenesis of siliciclastic sediments, with implications for provenance studies: The journal of geology, v. 104, no. 5, p. 525-542.

Nesbitt, H. W., Fedo, C. M., and Young, G. M., 1997, Quartz and feldspar stability, steady and non-steady-state weathering, and petrogenesis of siliciclastic sands and muds: The Journal of Geology, v. 105, no. 2, p. 173-192.
Neuweiler, F., Turner, E. C., and Burdige, D. J., 2009, Early Neoproterozoic origin of the metazoan clade recorded in carbonate rock texture: Geology, v. 37, no. 5, p. 475-478.
Norris, D., and Dyke, L., 1997, Proterozoic: The geology, mineral and hydrocarbon potential of northern Yukon Territory and northwestern District of Mackenzie, p. 65-84.
Novoselov, K., Belogub, E., Kotlyarov, V., Filippova, K., and Sadykov, S., 2018, Mineralogical and Geochemical Features of Oolitic Ironstones from the Sinara–Techa Deposit, Kurgan District, Russia: Geology of Ore Deposits, v. 60, no. 3, p. 265-276.
O'Connell, B., Wallace, M. W., vS Hood, A., Lechte, M. A., and Mahon, E. M., 2022, Nearshore environments before the evolution of land plants: Precambrian Research, v. 382, p. 106883.
O'Connell, B., Wallace, M. W., vS Hood, A., Lechte, M. A., and Planavsky, N. J., 2020, Iron-rich carbonate tidal deposits, Angepena Formation, South Australia: A redox-stratified Cryogenian basin: Precambrian Research, v. 342, p. 105668.
O'Neil, J., Carlson, R., Papineau, D., Levine, E., and Francis, D., 2018, The Nuvvuagittuq Greenstone Belt: a glimpse of Earth's earliest crust, Elsevier.
Odin, G., RWO'B, K., Gygi, R., and Guerrak, S., 1988, Chapter A2 Green Marine Clays from the Oolitic Ironstone Facies: Habit, Mineralogy, Environment, Developments in Sedimentology, Volume 45, Elsevier, p. 29-52.
Odin, G. S., 1988, Green Marine Clays: Oolitic Ironstone Facies, Verdine Facies, Glaucony Facies and Celadonite-Bearing Rock Facies-A Comparative Study, Elsevier.
Ojakangas, R. W., 1983, Tidal deposits in the early Proterozoic basin of the Lake Superior region—The Palms and the Pokegama Formations: Evidence for subtidal-shelf deposition of Superior-type banded iron-formation.
Olariu, C., Steel, R. J., Dalrymple, R. W., and Gingras, M. K., 2012, Tidal dunes versus tidal bars: The sedimentological and architectural characteristics of compound dunes in a tidal seaway, the lower Baronia Sandstone (Lower Eocene), Ager Basin, Spain: Sedimentary Geology, v. 279, p. 134-155.
Opeloye, S. A., Amigun, J. O., Sanusi, S. O., and Alabi, O., 2021, Palaeoenvironmental reconstruction and oolitic ironstone mapping of the Agbaja Ironstone Formation in the Nupe Basin, North-central Nigeria: insights from sedimentological and aeromagnetic analyses: Results in Geophysical Sciences, p. 100010.
Ossa, F. O., Hofmann, A., Vidal, O., Kramers, J. D., Belyanin, G., and Cavalazzi, B., 2016, Unusual manganese enrichment in the Mesoarchean Mozaan Group, Pongola Supergroup, South Africa: Precambrian Research, v. 281, p. 414-433.
Partin, C., Lalonde, S. V., Planavsky, N., Bekker, A., Rouxel, O., Lyons, T., and Konhauser, K., 2013, Uranium in iron formations and the rise of atmospheric oxygen: Chemical Geology, v. 362, p. 82-90.
Paton, C., Hellstrom, J., Paul, B., Woodhead, J., and Hergt, J., 2011, Iolite: Freeware for the visualisation and processing of mass spectrometric data: Journal of Analytical Atomic Spectrometry, v. 26, no. 12, p. 2508-2518.
Pe-Piper, G., and Dolansky, L. M., 2005, Early diagenetic origin of Al phosphate-sulfate minerals (woodhouseite and crandallite series) in terrestrial sandstones, Nova Scotia, Canada: American Mineralogist, v. 90, no. 8-9, p. 1434-1441.
Peryt, T. M., 1983, Classification of coated grains, Coated grains, Springer, p. 3-6.
Peter, J. M., 2003, Ancient iron formations: their genesis and use in the exploration for stratiform base metal sulphide deposits, with examples from the Bathurst Mining Camp: GeoText, v. 4, p. 145-176.
Petránek, J., 1964, Shallow-water origin of Early Paleozoic oolitic iron ores, Developments in Sedimentology, Volume 1, Elsevier, p. 319-322.
Petránek, J., 1991, Ordovician oolitic ironstones and their source of iron: Věstník Ústředního ústavu geologického, v. 66, no. 6, p. 321-327.
Petránek, J., and Van Houten, F. B., 1997, Phanerozoic Ooidal Ironstones: Contribution to the International Geological Correlation Programme, Project 277-Phanerozoic Ooidal Ironstones, Czech geological survey.
Pettijohn, F. J., 1975, Sedimentary rocks, Harper & Row New York.
Piepgras, D. J., Wasserburg, G., and Dasch, E., 1979, The isotopic composition of Nd in different ocean masses: Earth and Planetary Science Letters, v. 45, no. 2, p. 223-236.
Pirajno, F., and Yu, H.-C., 2021, Cycles of hydrothermal activity, precipitation of chemical sediments, with special reference to Algoma-type BIF: Gondwana Research, v. 100, p. 251-260.
Planavsky, N., Bekker, A., Rouxel, O. J., Kamber, B., Hofmann, A., Knudsen, A., and Lyons, T. W., 2010a, Rare earth element and yttrium compositions of Archean and Paleoproterozoic Fe formations revisited: new perspectives on the significance and mechanisms of deposition: Geochimica et Cosmochimica Acta, v. 74, no. 22, p. 6387-6405.
Planavsky, N. J., Rouxel, O. J., Bekker, A., Lalonde, S. V., Konhauser, K. O., Reinhard, C. T., and Lyons, T. W., 2010b, The evolution of the marine phosphate reservoir: Nature, v. 467, no. 7319, p. 1088.
Planavsky, N. J., Slack, J. F., Cannon, W. F., O'Connell, B., Isson, T. T., Asael, D., Jackson, J. C., Hardisty, D. S., Lyons, T. W., and Bekker, A., 2018, Evidence for episodic oxygenation in a weakly redox-buffered deep mid-Proterozoic ocean: Chemical Geology, v. 483, p. 581-594.
Pope, G. A., 2022, Weathering in the tropics, and related extratropical processes: Treatise on geomorphology, p. 279-298.

Poulton, S., and Raiswell, R., 2002, The low-temperature geochemical cycle of iron: from continental fluxes to marine sediment deposition: American journal of science, v. 302, no. 9, p. 774-805.
Poulton, S. W., 2021, The iron speciation paleoredox proxy, Cambridge University Press.
Poulton, S. W., Bekker, A., Cumming, V. M., Zerkle, A. L., Canfield, D. E., and Johnston, D. T., 2021, A 200-million-year delay in permanent atmospheric oxygenation: Nature, v. 592, no. 7853, p. 232-236.
Poulton, S. W., and Canfield, D. E., 2011, Ferruginous conditions: a dominant feature of the ocean through Earth's history: Elements, v. 7, no. 2, p. 107-112.
Poulton, S. W., Krom, M. D., and Raiswell, R., 2004, A revised scheme for the reactivity of iron (oxyhydr) oxide minerals towards dissolved sulfide: Geochimica et cosmochimica acta, v. 68, no. 18, p. 3703-3715.
Pufahl, P., Anderson, S., and Hiatt, E., 2014, Dynamic sedimentation of Paleoproterozoic continental margin iron formation, Labrador Trough, Canada: Paleoenvironments and sequence stratigraphy: Sedimentary Geology, v. 309, p. 48-65.
Pufahl, P. K., and Grimm, K. A., 2003, Coated phosphate grains: Proxy for physical, chemical, and ecological changes in seawater: Geology, v. 31, no. 9, p. 801-804.
Pufahl, P. K., Pirajno, F., and Hiatt, E. E., 2013, Riverine mixing and fluvial iron formation: A new type of Precambrian biochemical sediment: Geology, v. 41, no. 12, p. 1235-1238.
Pufahl, P. K., Squires, A. D., Murphy, J. B., Quesada, C., Lokier, S. W., Álvaro, J. J., and Hatch, J., 2020, Ordovician ironstone of the Iberian margin: Coastal upwelling, ocean anoxia and Palaeozoic biodiversity: The Depositional Record, v. 6, no. 3, p. 581-604.
Pulfrey, W., 1933, The iron-ore oolites and pisolites of North Wales: Quarterly Journal of the Geological Society, v. 89, no. 1-4, p. 401-430.
Purucker, M. E., 1984, OOLITIC IRONSTONES AND BANDED IRON-FORMATION: CONTROLS ON CHEMICAL SEDIMENTATION (OKLAHOMA, CANADA), Princeton University.
Qiu, Y., Qin, L., Huang, F., Zhao, T., and Li, Y., 2022, Early prosperity of iron bacteria at the end of the Paleoproterozoic era: Geophysical Research Letters, v. 49, no. 9, p. e2022GL097877.
Qiu, Y., Zhao, T., and Li, Y., 2020, The Yunmengshan iron formation at the end of the Paleoproterozoic era: Applied Clay Science, v. 199, p. 105888.
Quirke, T. T., 1961, Geology of the Temiscamie iron-formation, Lake Albanel iron range, Mistassini territory, Quebec, Canada: Economic Geology, v. 56, no. 2, p. 299-320.
Rahiminejad, A. H., and Zand-Moghadam, H., 2018, Synsedimentary formation of ooidal ironstone: an example from the Jurassic deposits of SE central Iran: Ore Geology Reviews, v. 95, p. 238-257.
Rainbird, R., Jefferson, C., and Young, G., 1996, The early Neoproterozoic sedimentary Succession B of northwestern Laurentia: Correlations and paleogeographic significance: Geological Society of America Bulletin, v. 108, no. 4, p. 454-470.
Rainbird, R. H., McNicoll, V., Theriault, R., Heaman, L., Abbott, J., Long, D., and Thorkelson, D., 1997, Pan-continental river system draining Grenville Orogen recorded by U-Pb and Sm-Nd geochronology of Neoproterozoic quartzarenites and mudrocks, northwestern Canada: The Journal of Geology, v. 105, no. 1, p. 1-17.
Raiswell, R., 2011, Iron transport from the continents to the open ocean: The aging–rejuvenation cycle: Elements, v. 7, no. 2, p. 101-106.
Raiswell, R., and Canfield, D. E., 1998, Sources of iron for pyrite formation in marine sediments: American Journal of Science, v. 298, no. 3, p. 219-245.
Raiswell, R., and Canfield, D. E., 2012, The iron biogeochemical cycle past and present: Geochemical perspectives, v. 1, no. 1, p. 1-220.
Rankey, E. C., and Berkeley, A., 2012, Holocene carbonate tidal flats: Principles of tidal sedimentology, p. 507-535.
Rasmussen, B., Fletcher, I. R., Bekker, A., Muhling, J. R., Gregory, C. J., and Thorne, A. M., 2012, Deposition of 1.88-billion-year-old iron formations as a consequence of rapid crustal growth: Nature, v. 484, no. 7395, p. 498-501.
Reineck, H.-E., and Singh, I. B., 2012, Depositional sedimentary environments: with reference to terrigenous clastics, Springer Science & Business Media.
Reinhard, C. T., and Planavsky, N. J., 2022, The history of ocean oxygenation: Annual Review of Marine Science, v. 14, p. 331-353.
Reinhard, C. T., Planavsky, N. J., Gill, B. C., Ozaki, K., Robbins, L. J., Lyons, T. W., Fischer, W. W., Wang, C., Cole, D. B., and Konhauser, K. O., 2017, Evolution of the global phosphorus cycle: Nature, v. 541, no. 7637, p. 386.
Reinhard, C. T., Planavsky, N. J., Robbins, L. J., Partin, C. A., Gill, B. C., Lalonde, S. V., Bekker, A., Konhauser, K. O., and Lyons, T. W., 2013, Proterozoic ocean redox and biogeochemical stasis: Proceedings of the National Academy of Sciences, v. 110, no. 14, p. 5357-5362.
Reinson, G., 1979, Facies models 14. Barrier island systems: Geoscience Canada, v. 6, no. 2, p. 51-68.
Reolid, M., Abad, I., and Martín-García, J. M., 2008, Palaeoenvironmental implications of ferruginous deposits related to a Middle–Upper Jurassic discontinuity (Prebetic Zone, Betic Cordillera, southern Spain): Sedimentary Geology, v. 203, no. 1-2, p. 1-16.
Roden, E., McBeth, J. M., Blothe, M., Percak-Dennett, E. M., Fleming, E. J., Holyoke, R. R., Luther III, G. W., and Emerson, D., 2012, The microbial ferrous wheel in a neutral pH groundwater seep: Frontiers in Microbiology, v. 3, p. 172.

Rohrlich, V., Price, N., and Calvert, S., 1969, Chamosite in the recent sediments of Loch Etive, Scotland: Journal of Sedimentary Research, v. 39, no. 2, p. 624-631.
Rooney, A. D., Cantine, M. D., Bergmann, K. D., Gómez-Pérez, I., Al Baloushi, B., Boag, T. H., Busch, J. F., Sperling, E. A., and Strauss, J. V., 2020, Calibrating the coevolution of Ediacaran life and environment: Proceedings of the National Academy of Sciences, v. 117, no. 29, p. 16824-16830.
Roselli, L., Cañedo-Argüelles, M., Goela, P. C., Cristina, S., Rieradevall, M., D'Adamo, R., and Newton, A., 2013, Do physiography and hydrology determine the physico-chemical properties and trophic status of coastal lagoons? A comparative approach: Estuarine, Coastal and Shelf Science, v. 117, p. 29-36.
Roy, M., Martin, J. B., Cherrier, J., Cable, J. E., and Smith, C. G., 2010, Influence of sea level rise on iron diagenesis in an east Florida subterranean estuary: Geochimica et Cosmochimica Acta, v. 74, no. 19, p. 5560-5573.
Rude, P. D., and Aller, R. C., 1989, Early diagenetic alteration of lateritic particle coatings in Amazon continental shelf sediment: Journal of Sedimentary Research, v. 59, no. 5, p. 704-716.
Rudmin, M., Banerjee, S., and Mazurov, A., 2017, Compositional variation of glauconites in Upper Cretaceous-Paleogene sedimentary iron-ore deposits in South-eastern Western Siberia: Sedimentary Geology, v. 355, p. 20-30.
Rudmin, M., Mazurov, A., and Banerjee, S., 2019, Origin of ooidal ironstones in relation to warming events: Cretaceous-Eocene Bakchar deposit, south-east Western Siberia: Marine and Petroleum Geology, v. 100, p. 309-325.
Rudmin, M., Reva, I., Sokol, E., Abdullayev, E., Ruban, A., Kudryavtsev, A., Tolkachev, O., and Mazurov, A., 2020, Minerals of rare earth elements in high-phosphorus ooidal ironstones of the western Siberia and Turgai depression: Minerals, v. 10, no. 1, p. 11.
Ruttenberg, K., 2003, The global phosphorus cycle: Treatise on geochemistry, v. 8, p. 682.
Ryan, P., and Reynolds, R., 1996, The origin and diagenesis of grain-coating serpentine-chlorite in Tuscaloosa Formation sandstone, US Gulf Coast: American Mineralogist, v. 81, no. 1-2, p. 213-225.
Rye, R., and Holland, H. D., 2000, Life associated with a 2.76 Ga ephemeral pond?: Evidence from Mount Roe# 2 paleosol: Geology, v. 28, no. 6, p. 483-486.
Saha, D., and Tripathy, V., 2012, Palaeoproterozoic sedimentation in the Cuddapah Basin, south India and regional tectonics: a review: Geological Society, London, Special Publications, v. 365, no. 1, p. 161-184.
Salama, W., 2014, Paleoenvironmental significance of aluminum phosphate-sulfate minerals in the upper Cretaceous ooidal ironstones, E-NE Aswan area, southern Egypt: International Journal of Earth Sciences, v. 103, p. 1621-1639.
Salama, W., El Aref, M., and Gaupp, R., 2013, Mineral evolution and processes of ferruginous microbialite accretion–an example from the Middle Eocene stromatolitic and ooidal ironstones of the Bahariya Depression, Western Desert, E gypt: Geobiology, v. 11, no. 1, p. 15-28.
Salama, W., El Aref, M., and Gaupp, R., 2014, Facies analysis and palaeoclimatic significance of ironstones formed during the Eocene greenhouse: Sedimentology, v. 61, no. 6, p. 1594-1624.
Sanders, C. J., Santos, I. R., Maher, D. T., Sadat-Noori, M., Schnetger, B., and Brumsack, H.-J., 2015, Dissolved iron exports from an estuary surrounded by coastal wetlands: can small estuaries be a significant source of Fe to the ocean?: Marine Chemistry, v. 176, p. 75-82.
Sarkar, S., Eriksson, P. G., and Chakraborty, S., 2004, Epeiric sea formation on Neoproterozoic supercontinent break-up: A distinctive signature in coastal storm bed amalgamation: Gondwana Research, v. 7, no. 2, p. 313-322.
Satkoski, A. M., Lowe, D. R., Beard, B. L., Coleman, M. L., and Johnson, C. M., 2016, A high continental weathering flux into Paleoarchean seawater revealed by strontium isotope analysis of 3.26 Ga barite: Earth and Planetary Science Letters, v. 454, p. 28-35.
Schellmann, W., 1969, Die Bildungsbedingungen sedimentärer Chamosit-und Hämatit-Eisenerze am Beispiel der Lagerstätte Echte: N. Jb. Miner. Abh, v. 111, p. 1-31.
Schieber, J., 1986, The possible role of benthic microbial mats during the formation of carbonaceous shales in shallow Mid-Proterozoic basins: Sedimentology, v. 33, no. 4, p. 521-536.
Schoen, R., 1964, Clay minerals of the Silurian Clinton ironstones, New York state: Journal of Sedimentary Research, v. 34, no. 4, p. 855-863.
Schröder, S., Bedorf, D., Beukes, N., and Gutzmer, J., 2011, From BIF to red beds: Sedimentology and sequence stratigraphy of the Paleoproterozoic Koegas Subgroup (South Africa): Sedimentary Geology, v. 236, no. 1-2, p. 25-44.
Schumm, S. A., 1968, Speculations concerning paleohydrologic controls of terrestrial sedimentation: Geological Society of America Bulletin, v. 79, no. 11, p. 1573-1588.
Schunck, S., Rickli, J., Wohlwend, S., Weissert, H., and Vance, D., 2023, Continental weathering as the source of iron in Jurassic iron oolites from Switzerland: Swiss Journal of Geosciences, v. 116, no. 1, p. 4.
Schwarz, T., and Germann, K., 1993, Ferricretes as a source of continental oolitic ironstones in northern Sudan: Chemical geology, v. 107, no. 3-4, p. 259-265.
Schweigart, H., 1965, Genesis of the iron ores of the Pretoria Series, South Africa: Economic Geology, v. 60, no. 2, p. 269-298.
Schwertmann, U., 1988, Occurrence and formation of iron oxides in various pedoenvironments, Iron in soils and clay minerals, Springer, p. 267-308.
Severmann, S., McManus, J., Berelson, W. M., and Hammond, D. E., 2010, The continental shelf benthic iron flux and its isotope composition: Geochimica et Cosmochimica Acta, v. 74, no. 14, p. 3984-4004.

Shaw, H., and Wasserburg, G., 1985, Sm-Nd in marine carbonates and phosphates: Implications for Nd isotopes in seawater and crustal ages: Geochimica et Cosmochimica Acta, v. 49, no. 2, p. 503-518.
Sheldon, N. D., 2006, Precambrian paleosols and atmospheric CO2 levels: Precambrian Research, v. 147, no. 1-2, p. 148-155.
Sheldon, N. D., Mitchell, R. L., and Dzombak, R. M., 2021, Reconstructing Precambrian pCO2 and pO2 using paleosols, Cambridge University Press.
Sheldon, R., 1970, Sedimentation of iron-rich rocks of Llandovery age (Lower Silurian) in the southern Appalachian basin: Correlation of the Northern American Silurian Rocks: Geological Society of America Special Paper, v. 102, p. 107-112.
Sholkovitz, E., 1976, Flocculation of dissolved organic and inorganic matter during the mixing of river water and seawater: Geochimica et Cosmochimica Acta, v. 40, no. 7, p. 831-845.
Siedlecka, A., and Edwards, M., 1980, Lithostratigraphy and sedimentation of the Riphean Basnaering Formation, Varanger Peninsula, North Norway.
Siehl, A., and Thein, J., 1989, Minette-type ironstones: Geological Society, London, Special Publications, v. 46, no. 1, p. 175-193.
Siever, R., 1992, The silica cycle in the Precambrian: Geochimica et Cosmochimica Acta, v. 56, no. 8, p. 3265-3272.
Simonson, B. M., 1987, Early silica cementation and subsequent diagenesis in arenites from four early Proterozoic iron formations of North America: Journal of Sedimentary Research, v. 57, no. 3, p. 494-511.
Simonson, B. M., 2003, Origin and evolution of large Precambrian iron formations: SPECIAL PAPERS-GEOLOGICAL SOCIETY OF AMERICA, p. 231-244.
Simonson, B. M., and Goode, A., 1989, First discovery of ferruginous chert arenites in the early Precambrian Hamersley Group of Western Australia: Geology, v. 17, no. 3, p. 269-272.
Simonson, B. M., and Lanier, W. P., 1987, Early silica cementation and microfossil preservation in cavities in iron formation stromatolites, early Proterozoic of Canada: Precambrian Iron-Formations, p. 187-213.
Sindol, G. P., Babechuk, M. G., Conliffe, J., Slack, J. F., Rosca, C., and Schoenberg, R., 2022, Shallow-ocean and atmospheric redox signatures preserved in the ca. 1.88 Ga Sokoman iron formation, Labrador Trough, Canada: Precambrian Research, v. 379, p. 106750.
Singer, P. C., and Stumm, W., Kinetics of the oxidation of ferrous iron, *in* Proceedings Second Symposium on Coal Mine Drainage Research1968, National Coal Association/Bituminous Coal Research, p. 12-34.
Slack, J., Grenne, T., Bekker, A., Rouxel, O., and Lindberg, P., 2007, Suboxic deep seawater in the late Paleoproterozoic: evidence from hematitic chert and iron formation related to seafloor-hydrothermal sulfide deposits, central Arizona, USA: Earth and Planetary Science Letters, v. 255, no. 1, p. 243-256.
Slack, J. F., Grenne, T., and Bekker, A., 2009, Seafloor-hydrothermal Si-Fe-Mn exhalites in the Pecos greenstone belt, New Mexico, and the redox state of ca. 1720 Ma deep seawater: Geosphere, v. 5, no. 3, p. 302-314.
Slotznick, S., Sperling, E., Tosca, N., Miller, A., Clayton, K., van Helmond, N., Slomp, C., and Swanson-Hysell, N., 2020, Unraveling the mineralogical complexity of sediment iron speciation using sequential extractions: Geochemistry, Geophysics, Geosystems, v. 21, no. 2, p. e2019GC008666.
Smith, A., Beukes, N., Gutzmer, J., Czaja, A., Johnson, C., and Nhleko, N., 2017, Oncoidal granular iron formation in the Mesoarchaean Pongola Supergroup, southern Africa: Textural and geochemical evidence for biological activity during iron deposition: Geobiology, v. 15, no. 6, p. 731-749.
Smith, A. J., and Beukes, N. J., 2023, The paleoenvironmental implications of pre-Great Oxidation Event manganese deposition in the Mesoarchean Ijzermijn Iron Formation Bed, Mozaan Group, Pongola Supergroup, South Africa: Precambrian Research, v. 384, p. 106922.
Smith, A. J., Beukes, N. J., and Gutzmer, J., 2013, The composition and depositional environments of Mesoarchean iron formations of the West Rand Group of the Witwatersrand Supergroup, South Africa: Economic Geology, v. 108, no. 1, p. 111-134.
Smith, A. J., Beukes, N. J., Gutzmer, J., Johnson, C. M., Czaja, A. D., Nhleko, N., de Beer, F., Hoffman, J. W., and Awramik, S. M., 2020, Life on a Mesoarchean marine shelf–insights from the world's oldest known granular iron formation: Scientific Reports, v. 10, no. 1, p. 1-8.
Sokol, E. V., Kokh, S. N., Kozmenko, O. A., Nekipelova, A. V., Rudmin, M., Khvorov, P. V., and Artemyev, D. A., 2020, Geochemistry and mineralogy of rare earth elements in high-phosphorus ooidal ironstones: A case study of the Kamysh-Burun deposit (Azov–Black Sea iron Province): Ore Geology Reviews, p. 103827.
Song, H., Jiang, G., Poulton, S. W., Wignall, P. B., Tong, J., Song, H., An, Z., Chu, D., Tian, L., and She, Z., 2017, The onset of widespread marine red beds and the evolution of ferruginous oceans: Nature communications, v. 8, no. 1, p. 399.
Sperling, E. A., Halverson, G. P., Knoll, A. H., Macdonald, F. A., and Johnston, D. T., 2013, A basin redox transect at the dawn of animal life: Earth and Planetary Science Letters, v. 371, p. 143-155.
Sperling, E. A., and Stockey, R. G., 2018, The temporal and environmental context of early animal evolution: considering all the ingredients of an 'explosion': Integrative and Comparative Biology.
Sperling, E. A., Wolock, C. J., Morgan, A. S., Gill, B. C., Kunzmann, M., Halverson, G. P., Macdonald, F. A., Knoll, A. H., and Johnston, D. T., 2015, Statistical analysis of iron geochemical data suggests limited late Proterozoic oxygenation: Nature, v. 523, no. 7561, p. 451.
Spiegel, T., Vosteen, P., Wallmann, K., Paul, S. A., Gledhill, M., and Scholz, F., 2021, Updated estimates of sedimentary potassium sequestration and phosphorus release on the Amazon shelf: Chemical Geology, v. 560, p. 120017.

Stern, R. J., Mukherjee, S. K., Miller, N. R., Ali, K., and Johnson, P. R., 2013, ~ 750Ma banded iron formation from the Arabian-Nubian Shield—Implications for understanding neoproterozoic tectonics, volcanism, and climate change: Precambrian Research, v. 239, p. 79-94.
Stüeken, E. E., Catling, D. C., and Buick, R., 2012, Contributions to late Archaean sulphur cycling by life on land: Nature Geoscience, v. 5, no. 10, p. 722-725.
Sturesson, U., 1995, Llanvirnian (Ord.) iron ooids in Baltoscandia: element mobility, REE distribution patterns, and origin of the REE: Chemical Geology, v. 125, no. 1-2, p. 45-60.
Sturesson, U., 2003, Lower Palaeozoic iron oolites and volcanism from a Baltoscandian perspective: Sedimentary Geology, v. 159, no. 3-4, p. 241-256.
Sturesson, U., Heikoop, J., and Risk, M., 2000, Modern and Palaeozoic iron ooids—a similar volcanic origin: Sedimentary Geology, v. 136, no. 1-2, p. 137-146.
Subarkah, D., Blades, M. L., Collins, A. S., Farkaš, J., Gilbert, S., Löhr, S. C., Redaa, A., Cassidy, E., and Zack, T., 2022, Unraveling the histories of Proterozoic shales through in situ Rb-Sr dating and trace element laser ablation analysis: Geology, v. 50, no. 1, p. 66-70.
Sumner, D. Y., and Grotzinger, J. P., 1993, Numerical modeling of ooid size and the problem of Neoproterozoic giant ooids: Journal of Sedimentary Research, v. 63, no. 5, p. 974-982.
Sun, J., Qian, Y., Li, Y., Zhang, P., Qiao, J., Shen, Y., and Sun, F., 2023, Age and geochemistry of the Naxiguole banded iron formation (BIF), NW China: recurrence of superior-type BIF in the Neoproterozoic: International Geology Review, v. 65, no. 14, p. 2235-2255.
Sundby, B. r., Gobeil, C., Silverberg, N., and Alfonso, M., 1992, The phosphorus cycle in coastal marine sediments: Limnology and oceanography, v. 37, no. 6, p. 1129-1145.
Survey, Y. G., 2020, Yukon digital bedrock geology, Yukon Geological Survey.
Sverjensky, D. A., 1984, Europium redox equilibria in aqueous solution: Earth and Planetary Science Letters, v. 67, no. 1, p. 70-78.
Swanner, E. D., Planavsky, N. J., Lalonde, S. V., Robbins, L. J., Bekker, A., Rouxel, O. J., Saito, M. A., Kappler, A., Mojzsis, S. J., and Konhauser, K. O., 2014, Cobalt and marine redox evolution: Earth and Planetary Science Letters, v. 390, p. 253-263.
Swanson-Hysell, N. L., Maloof, A. C., Condon, D. J., Jenkin, G. R., Alene, M., Tremblay, M. M., Tesema, T., Rooney, A. D., and Haileab, B., 2015, Stratigraphy and geochronology of the Tambien Group, Ethiopia: Evidence for globally synchronous carbon isotope change in the Neoproterozoic: Geology, v. 43, no. 4, p. 323-326.
Swift, D. J., Figueiredo, A. G., Freeland, G., and Oertel, G., 1983, Hummocky cross-stratification and megaripples; a geological double standard?: Journal of Sedimentary Research, v. 53, no. 4, p. 1295-1317.
Tachikawa, K., Piotrowski, A. M., and Bayon, G., 2014, Neodymium associated with foraminiferal carbonate as a recorder of seawater isotopic signatures: Quaternary Science Reviews, v. 88, p. 1-13.
Tanaka, T., Togashi, S., Kamioka, H., Amakawa, H., Kagami, H., Hamamoto, T., Yuhara, M., Orihashi, Y., Yoneda, S., and Shimizu, H., 2000, JNdi-1: a neodymium isotopic reference in consistency with LaJolla neodymium: Chemical Geology, v. 168, no. 3-4, p. 279-281.
Tang, D., Xie, B., Shi, X., and Zhou, X., 2022, Low level of phosphorous concentration in terminal Paleoproterozoic shallow seawater: Evidence from Chuanlinggou ironstone on North China Platform: Precambrian Research, v. 370, p. 106554.
Taylor, G. F., 1973, The geochemistry of siderite in relation to ironstone in the Paradise Creek Formation, northwest Queensland: Journal of Geochemical Exploration, v. 2, no. 4, p. 367-382.
Taylor, J. H., 1949, Petrology of the Northampton sand ironstone formation, HM Stationery Office.
Taylor, K., 1990, Berthierine from the non-marine Wealden (Early Cretaceous) sediments of south-east England: Clay Minerals, v. 25, no. 3, p. 391-399.
Taylor, K. G., 1998, Spatial and temporal variations in early diagenetic organic matter oxidation pathways in Lower Jurassic mudstones of eastern England: Chemical Geology, v. 145, no. 1-2, p. 47-60.
Taylor, K. G., and Curtis, C. D., 1995, Stability and facies association of early diagenetic mineral assemblages; an example from a Jurassic ironstone-mudstone succession, UK: Journal of Sedimentary Research, v. 65, no. 2a, p. 358-368.
Taylor, K. G., and Macquaker, J. H., 2011, Iron minerals in marine sediments record chemical environments: Elements, v. 7, no. 2, p. 113-118.
Taylor, K. G., Simo, J., Yocum, D., and Leckie, D. A., 2002, Stratigraphic significance of ooidal ironstones from the Cretaceous western interior seaway: The Peace River Formation, Alberta, Canada, and the Castlegate Sandstone, Utah, USA: Journal of Sedimentary Research, v. 72, no. 2, p. 316-327.
Taylor, S. R., and McLennan, S. M., 1985, The continental crust: its composition and evolution.
Tegengren, F. R., 1921, The Iron Ores and Iron Industry of China, Geological Survey of China Ministry of Agriculture and Commerce.
Thamdrup, B., 2000, Bacterial manganese and iron reduction in aquatic sediments, Advances in microbial ecology, Springer, p. 41-84.
Thomson, D., Rainbird, R. H., Planavsky, N., Lyons, T. W., and Bekker, A., 2015, Chemostratigraphy of the Shaler Supergroup, Victoria Island, NW Canada: A record of ocean composition prior to the Cryogenian glaciations: Precambrian Research, v. 263, p. 232-245.
Thorkelson, D. J., 2000, Geology and mineral occurrences of the Slats Creek, Fairchild Lake and" Dolores Creek" areas, Wernecke Mountains (106D/16, 106C/13, 106C/14), Yukon Territory.

Thorkelson, D. J., Abbott, J. G., Mortensen, J. K., Creaser, R. A., Villeneuve, M. E., McNicoll, V. J., and Layer, P. W., 2005, Early and middle Proterozoic evolution of Yukon, Canada: Canadian Journal of Earth Sciences, v. 42, no. 6, p. 1045-1071.
Thorkelson, D. J., Mortensen, J. K., Creaser, R. A., Davidson, G. J., and Abbott, J. G., 2001, Early Proterozoic magmatism in Yukon, Canada: constraints on the evolution of northwestern Laurentia: Canadian Journal of Earth Sciences, v. 38, no. 10, p. 1479-1494.
Thurston, P., Kamber, B., and Whitehouse, M., 2012, Archean cherts in banded iron formation: insight into Neoarchean ocean chemistry and depositional processes: Precambrian Research, v. 214, p. 227-257.
Todd, S., Pufahl, P., Murphy, J., and Taylor, K., 2019, Sedimentology and oceanography of early Ordovician ironstone, Bell Island, Newfoundland: Ferruginous seawater and upwelling in the Rheic Ocean: Sedimentary Geology, v. 379, p. 1-15.
Tornos, F., Peter, J. M., Allen, R., and Conde, C., 2015, Controls on the siting and style of volcanogenic massive sulphide deposits: Ore Geology Reviews, v. 68, p. 142-163.
Tosca, N. J., Jiang, C. Z., Rasmussen, B., and Muhling, J., 2019, Products of the iron cycle on the early Earth: Free Radical Biology and Medicine, v. 140, p. 138-153.
Tostevin, R., and Ahmed, I. A., 2023, Micronutrient availability in Precambrian oceans controlled by greenalite formation: Nature Geoscience, v. 16, no. 12, p. 1188-1193.
Trendall, A., 1968, Three great basins of Precambrian banded iron formation deposition: a systematic comparison: Geological Society of America Bulletin, v. 79, no. 11, p. 1527-1544.
Trendall, A., 2002, The significance of iron-formation in the Precambrian stratigraphic record: Precambrian sedimentary environments: A modern approach to ancient depositional systems, p. 33-66.
Tribovillard, N., Algeo, T. J., Lyons, T., and Riboulleau, A., 2006, Trace metals as paleoredox and paleoproductivity proxies: an update: Chemical geology, v. 232, no. 1, p. 12-32.
Tucker, M., and Wright, V., 1990, Carbonate platforms: facies evolution and sequences: Int Ass Sed, v. 2, p. 328.
Turner, E., 2011a, Little Dal Group, *in* Martel, E., Turner, E. C., and Fischer, B. J., eds., Geology of the Central Mackenzie Mountains of the Northern Canadian Cordillera: Sekwi Mountain (105P), Mount Eduni (106A), Northwestern Wrigley Lake (95M) Map-areas, Northwest-Territories, Northwest Territories Geoscience Office.
Turner, E., and Bekker, A., 2016, Thick sulfate evaporite accumulations marking a mid-Neoproterozoic oxygenation event (Ten Stone Formation, Northwest Territories, Canada): GSA Bulletin, v. 128, no. 1-2, p. 203-222.
Turner, E., and Long, D. G., 2012, Formal definition of the Neoproterozoic Mackenzie Mountains Supergroup (Northwest Territories), and formal stratigraphic nomenclature for its carbonate and evaporite formations: Geological Survey of Canada Open File, v. 7112.
Turner, E. C., 2011b, Stratigraphy of the Mackenzie Mountains supergroup in the Wernecke Mountains, Yukon, *in* MacFarlane, K. E., Weston, L. H., and Relf, C., eds., Yukon Exploration and Geology, Yukon Geological Survey, p. 207-231.
Turner, E. C., 2021, Possible poriferan body fossils in early Neoproterozoic microbial reefs: Nature, p. 1-5.
Turner, E. C., James, N. P., and Narbonne, G. M., 1997, Growth dynamics of Neoproterozoic calcimicrobial reefs, Mackenzie Mountains, northwest Canada: Journal of Sedimentary Research, v. 67, no. 3, p. 437-450.
Turner, E. C., and Long, D. G., 2008, Basin architecture and syndepositional fault activity during deposition of the Neoproterozoic Mackenzie Mountains supergroup, Northwest Territories, Canada: Canadian Journal of Earth Sciences, v. 45, no. 10, p. 1159-1184.
Turner, E. C., Narbonne, G. M., and James, N. P., 1993, Neoproterozoic reef microstructures from the Little Dal Group, northwestern Canada: Geology, v. 21, no. 3, p. 259-262.
van de Flierdt, T., Frank, M., Lee, D.-C., Halliday, A. N., Reynolds, B. C., and Hein, J. R., 2004, New constraints on the sources and behavior of neodymium and hafnium in seawater from Pacific Ocean ferromanganese crusts: Geochimica et Cosmochimica Acta, v. 68, no. 19, p. 3827-3843.
Van Hise, C. R., 1901, The iron-ore deposits of the Lake Superior region, US Government Printing Office.
Van Houten, F., and Arthur, M. A., 1989, Temporal patterns among Phanerozoic oolitic ironstones and oceanic anoxia: Geological Society, London, Special Publications, v. 46, no. 1, p. 33-49.
Van Houten, F., and Karasek, R., 1981, Sedimentologic framework of Late Devonian oolitic iron formation, Shatti Valley, west-central Libya: Journal of Sedimentary Research, v. 51, no. 2, p. 415-427.
Van Houten, F., and Purucker, M., 1984, Glauconitic peloids and chamositic ooids-favorable factors, constraints, and problems: Earth-Science Reviews, v. 20, no. 3, p. 211-243.
van Houten, F. B., 1992, Review of Cenozoic ooidal ironstones: Sedimentary geology, v. 78, no. 1-2, p. 101-110.
Van Houten, F. B., and Bhattacharyya, D. P., 1982, Phanerozoic oolitic ironstones--geologic record and facies model: Annual Review of Earth and Planetary Sciences, v. 10, no. 1, p. 441-457.
Van Staal, C., Wilson, R., Rogers, N., Fyffe, L., Langton, J., McCutcheon, S., McNicoll, V., and Ravenhurst, C., 2003, Geology and tectonic history of the Bathurst Supergroup, Bathurst Mining Camp, and its relationships to coeval rocks in southwestern New Brunswick and adjacent Maine—A synthesis.
Van Straaten, L. M. J. U., 1961, Sedimentation in tidal flat areas: Bulletin of Canadian Petroleum Geology, v. 9, no. 7, p. 203-226.
Vargas, M., Kashefi, K., Blunt-Harris, E. L., and Lovley, D. R., 1998, Microbiological evidence for Fe (III) reduction on early Earth: Nature, v. 395, no. 6697, p. 65-67.

Verbaas, J., Thorkelson, D. J., Milidragovic, D., Crowley, J. L., Foster, D., Gibson, H. D., and Marshall, D. D., 2018, Rifting of western Laurentia at 1.38 Ga: The Hart River sills of Yukon, Canada: Lithos, v. 316, p. 243-260.
Veselovskiy, R., Arzamastsev, A., Tselmovich, V., Fetisova, A., and Kulakova, E., 2017, Paleomagnetism of Precambrian dikes in the Kola part of northeastern Fennoscandia and its relation to the Svecofennian orogeny: Izvestiya, Physics of the Solid Earth, v. 53, p. 898-907.
Vodrážková, S., Kumpan, T., Vodrážka, R., Frýda, J., Čopjaková, R., Koubová, M., Munnecke, A., Kalvoda, J., and Holá, M., 2022, Ferruginous coated grains of microbial origin from the Lower Devonian (Pragian) of the Prague Basin (Czech Republic)–Petrological and geochemical perspective: Sedimentary Geology, v. 438, p. 106194.
Volkert, R. A., Monteverde, D. H., Friehauf, K. C., Gates, A. E., Dalton, R. F., and Smith, R. C., 2010, Geochemistry and origin of Neoproterozoic ironstone deposits in the New Jersey Highlands and implications for the eastern Laurentian rifted margin in the north-central Appalachians, USA: Geological Society of America Memoirs, v. 206, p. 283-306.
Von Damm, K., 1990, Seafloor hydrothermal activity: black smoker chemistry and chimneys: Annual Review of Earth and Planetary Sciences, v. 18, no. 1, p. 173-204.
Vosteen, P., Spiegel, T., Gledhill, M., Frank, M., Zabel, M., and Scholz, F., 2022, The Fate of Sedimentary Reactive Iron at the Land-Ocean Interface: A Case Study from the Amazon Shelf: Geochemistry, Geophysics, Geosystems, p. e2022GC010543.
Wang, C., Lechte, M. A., Reinhard, C. T., Asael, D., Cole, D. B., Halverson, G. P., Porter, S. M., Galili, N., Halevy, I., Rainbird, R. H., Lyons, T. W., and Planavsky, N. J., 2022, Strong evidence for a weakly oxygenated ocean–atmosphere system during the Proterozoic: Proceedings of the National Academy of Sciences.
Wang, C., Robbins, L. J., Planavsky, N. J., Beukes, N. J., Patry, L. A., Lalonde, S. V., Lechte, M. A., Asael, D., Reinhard, C. T., and Zhang, L., 2023, Archean to early Paleoproterozoic iron formations document a transition in iron oxidation mechanisms: Geochimica et Cosmochimica Acta, v. 343, p. 286-303.
Wang, P., Du, Y., Yu, W., Algeo, T. J., Zhou, Q., Xu, Y., Qi, L., Yuan, L., and Pan, W., 2020, The chemical index of alteration (CIA) as a proxy for climate change during glacial-interglacial transitions in Earth history: Earth-Science Reviews, v. 201, p. 103032.
Wang, X.-C., Li, Z.-X., Li, X.-H., Li, Q.-L., and Zhang, Q.-R., 2011, Geochemical and Hf–Nd isotope data of Nanhua rift sedimentary and volcaniclastic rocks indicate a Neoproterozoic continental flood basalt provenance: Lithos, v. 127, no. 3-4, p. 427-440.
Warchola, T., Lalonde, S. V., Pecoits, E., Von Gunten, K., Robbins, L. J., Alessi, D. S., Philippot, P., and Konhauser, K. O., 2018, Petrology and geochemistry of the Boolgeeda Iron Formation, Hamersley Basin, Western Australia: Precambrian Research, v. 316, p. 155-173.
Warke, M. R., Di Rocco, T., Zerkle, A. L., Lepland, A., Prave, A. R., Martin, A. P., Ueno, Y., Condon, D. J., and Claire, M. W., 2020, The great oxidation event preceded a paleoproterozoic “snowball Earth”: Proceedings of the National Academy of Sciences, v. 117, no. 24, p. 13314-13320.
Wei, G.-Y., Chen, T., Poulton, S. W., Lin, Y.-B., He, T., Shi, X., Chen, J., Li, H., Qiao, S., and Liu, J., 2021, A chemical weathering control on the delivery of particulate iron to the continental shelf: Geochimica et Cosmochimica Acta, v. 308, p. 204-216.
Wellman, C. H., and Strother, P. K., 2015, The terrestrial biota prior to the origin of land plants (embryophytes): a review of the evidence: Palaeontology, v. 58, no. 4, p. 601-627.
Wijsman, J. W., Middelburg, J. J., and Heip, C. H., 2001, Reactive iron in Black Sea sediments: implications for iron cycling: Marine Geology, v. 172, no. 3-4, p. 167-180.
Williams, G. E., 1971, Flood deposits of the sand-bed ephemeral streams of central Australia: Sedimentology, v. 17, no. 1-2, p. 1-40.
Williams, G. E., Schmidt, P. W., and Clark, D. A., 2004, Palaeomagnetism of iron-formation from the late Palaeoproterozoic Frere Formation, Earaheedy Basin, Western Australia: palaeogeographic and tectonic implications: Precambrian Research, v. 128, no. 3-4, p. 367-383.
Williams, M., 2003, The development of hiatal surfaces in the Osmington Mills ironstone member of the upper Jurassic Ringstead formation of south Dorset, England: Proceedings of the Geologists' Association, v. 114, no. 3, p. 193-210.
Woltz, C., Porter, S., Agić, H., Dehler, C., Junium, C., Riedman, L., Hodgskiss, M., Wörndle, S., and Halverson, G., 2020, Total organic carbon and the preservation of organic-walled microfossils in Precambrian shale: Geology.
Woodhead, J. D., Hellstrom, J., Hergt, J. M., Greig, A., and Maas, R., 2007, Isotopic and elemental imaging of geological materials by laser ablation inductively coupled plasma-mass spectrometry: Geostandards and Geoanalytical Research, v. 31, no. 4, p. 331-343.
Wright, M. D., 1959, The formation of cross-bedding by a meandering or braided stream: Journal of Sedimentary Research, v. 29, no. 4, p. 610-615.
Wu, X., Zhu, J., He, H., Xian, H., Yang, Y., Ma, L., Liang, X., Lin, X., Li, S., and Konhauser, K. O., 2023, Geodynamic oxidation of Archean terrestrial surfaces: Communications Earth & Environment, v. 4, no. 1, p. 132.
Xie, B., Lechte, M., Shi, X., Wang, X., Zhou, L., Zhou, X., Huang, K. J., Wang, Z., Wang, X., and Tang, D., 2024, Marine aluminum phosphate–sulfate authigenesis as a phosphorus sink during mid-Proterozoic oxygenation: Geophysical Research Letters, v. 51, no. 4, p. e2023GL107512.

Xing, B., Graham, N., and Yu, W., 2020, Transformation of siderite to goethite by humic acid in the natural environment: Communications Chemistry, v. 3, no. 1, p. 38.
Yan, B., Sun, J., and Zhu, X.-K., 2015, Fe isotopes constrain the origin of iron ore in Ningxiang: Acta Geologica Sinica, v. 89(S), p. 217-221.
Yang, X., Mao, J., Li, R., Huang, F., He, C., Zhao, C., Wei, W., Yang, G., Xiong, Y., and Poulton, S. W., 2024, Fluctuating oxygenation and dynamic iron cycling in the late Paleoproterozoic ocean: Earth and Planetary Science Letters, v. 626, p. 118554.
Yang, X., Mao, J., Li, R., Jiang, Z., Yu, M., Xu, L., Reershemius, T., and Planavsky, N. J., 2023a, The deposition and significance of an Ediacaran non-glacial iron formation: Geobiology, v. 21, no. 1, p. 44-65.
Yang, X., Mao, J., Wu, C., Li, Z., Konhauser, K. O., Chen, B., and Yang, G., 2023b, Genesis and depositional environment of the Carboniferous Baishanquan iron deposit in Eastern Tianshan, Northwestern China: Lithos, p. 107304.
Yang, X., Mao, J., Zhang, Z., Robbins, L. J., Planavsky, N. J., Jiang, Z., Duan, S., and Chen, Z., 2021, Episodic ferruginous conditions associated with submarine volcanism led to the deposition of a Late Carboniferous iron formation: Geochimica et Cosmochimica Acta, v. 292, p. 1-23.
Yellappa, T., Chetty, T., and Santosh, M., 2016, Precambrian iron formations from the Cauvery Suture Zone, Southern India: Implications for sub-marine hydrothermal origin in Neoarchean and Neoproterozoic convergent margin settings: Ore Geology Reviews, v. 72, p. 1177-1196.
Yeo, G., 1981, The late Proterozoic Rapitan glaciation in the northern Cordillera: Proterozoic Basins of Canada, v. 81, no. 10.
Yilmaz, İ. Ö., Göncüoğlu, M. C., Demiray, D. G., and Gedik, I., 2015, An approach to paleoclimatic conditions for Devonian (upper Lochkovian and middle Givetian) ironstone formation, NW Anatolian carbonate platform: Turkish Journal of Earth Sciences, v. 24, no. 1, p. 21-38.
Young, G., Jefferson, C., Delaney, G., and Yeo, G., 1979, Middle and late Proterozoic evolution of the northern Canadian Cordillera and Shield: Geology, v. 7, no. 3, p. 125-128.
Young, G. M., 1976, Iron-formation and glaciogenic rocks of the Rapitan Group, Northwest Territories, Canada: Precambrian Research, v. 3, no. 2, p. 137-158.
Young, G. M., 2002, Stratigraphic and tectonic settings of Proterozoic glaciogenic rocks and banded iron-formations: relevance to the snowball Earth debate: Journal of African Earth Sciences, v. 35, no. 4, p. 451-466.
Young, G. M., 2013, Evolution of Earth's climatic system: Evidence from ice ages, isotopes, and impacts: GSA Today, v. 23, no. 10, p. 4-10.
Young, T. P., 1989, Phanerozoic ironstones: an introduction and review: Geological Society, London, Special Publications, v. 46, no. 1, p. ix-xxv.
Zajac, I. S., and Peter, J. M., 2022, Origin of the Sokoman Iron Formation, Labrador Trough, Canada: The Canadian Mineralogist, v. 60, no. 3, p. 417-431.
Zegeye, A., Bonneville, S., Benning, L. G., Sturm, A., Fowle, D. A., Jones, C., Canfield, D. E., Ruby, C., MacLean, L. C., and Nomosatryo, S., 2012, Green rust formation controls nutrient availability in a ferruginous water column: Geology, v. 40, no. 7, p. 599-602.
Zeng, T., Tang, L., Wang, H.-H., Santosh, M., and Sheng, Y.-M., 2023, The Paleoproterozoic Zhaigou banded iron formation in the Fuping Complex, North China Craton: Geochemistry, geochronology and implications for genesis and tectonic setting: Ore Geology Reviews, p. 105314.
Zhang, S. H., Ernst, R. E., Pei, J. L., Zhao, Y., and Hu, G. H., 2021, Large Igneous Provinces (LIPs) and Anoxia Events in "The Boring Billion": Large Igneous Provinces: A Driver of Global Environmental and Biotic Changes, p. 449-486.
Zhang, T., Keller, C. B., Hoggard, M. J., Rooney, A. D., Halverson, G. P., Bergmann, K. D., Crowley, J. L., and Strauss, J. V., 2023, A Bayesian framework for subsidence modeling in sedimentary basins: A case study of the Tonian Akademikerbreen Group of Svalbard, Norway: Earth and Planetary Science Letters, v. 620, p. 118317.
Zhao, Y., and Bi, C., 2000, Time–space distribution and evolution of the Ningxiang type sedimentary iron deposits: Miner. Deposits, v. 19, no. 4, p. 350-362.
Zhu, X., Gao, Z., and Wang, X., 2022, Shallow-water hydrothermal venting and the formation of Precambrian ironstones: Insights from the terminal-Paleoproterozoic Xuanlong ironstones in North China Craton: Precambrian Research, v. 375, p. 106667.
Zhu, X.-K., Sun, J., and Li, Z.-H., 2019, Iron isotopic variations of the Cryogenian banded iron formations: A new model: Precambrian Research, p. 105359.